Advancements in 2D Photonic Crystal Hydrogel and Organogel Sensor Fabrication

by

Andrew Eagle Coukouma

B.A. Chemistry, University of Maryland Baltimore County, 2013

Submitted to the Graduate Faculty of the

Dietrich School of Arts and Sciences in partial fulfillment

of the requirements for the degree of

Master of Science

University of Pittsburgh

2021

UNIVERSITY OF PITTSBURGH

DIETRICH SCHOOL OF ARTS AND SCIENCES

This thesis was presented

by

Andrew Coukouma

It was defended on

May 26th 2021

and approved by

Jill Millstone, Associate Professor, Department of Chemistry

David Waldeck, Professor, Department of Chemistry

Thesis Advisor: Sanford Asher, Distinguished Professor, Department of Chemistry

Advancements in 2D Photonic Crystal Hydrogel and Organogel Sensor Fabrication

Andrew Eagle Coukouma, MS

University of Pittsburgh, 2021

2D photonic crystal hydrogel and organogel sensors are composed of 2D photonic crystals embedded in volume responsive hydrogels and organogels. Hydrogels utilize polymers in water. Organogels utilize polymers in organic solvents. Hydrogels and organogels changes volume due to changing concentrations of analytes such as proteins, enzymes, and small molecules. We measure the hydrogel or organogel volume by using an embedded 2D Photonic Crystal (2DPhC). 2DPhCs utilizes hexagonal monolayers of polystyrene spheres that diffract light at wavelengths that depend upon the 2DPhC particle spacing

In this work, the state of the art of 2D Photonic crystal hydrogel and organogel sensors is advanced. An interpenetrating poly-vinyl alcohol network enabled the use of fragile hydrogels. Macroporous hydrogels increase hydrogel volume responsiveness. I increased the understanding of 2D Photonic Crystal fabrication. Finally, I improved our understanding of the transition of protein hydrogels to protein organogels.

Table of Contents

Preface xix

1.0 Introduction, Motivation 1

1.1 References 2

2.0 Removable Interpenetrating Network Enables Highly-Responsive 2-D Photonic Crystal Hydrogel Sensors 3

2.1 Introduction 4

2.2 Results and Discussion 7

2.3 Experimental 11

2.3.1 Materials 11

2.3.2 Fabrication of pH Sensitive Hydrogels 12

2.3.3 pH Sensing 13

2.4 Conclusions 14

2.5 Acknowledgements 14

2.6 References 14

3.0 Increased Volume Responsiveness of Macroporous Hydrogels 18

3.1 Introduction 19

3.2 Materials and Methods 20

3.2.1 Materials 20

3.2.2 Fabrication of Inverse Opal Hydrogels 21

3.2.3 Fabrication of Vortexed Hydrogels 21

3.2.4 Electron Microscopy of Hydrogels 22

3.2.5 Measurement of pH Volume Response 22

3.3 Results and Discussion 23

3.3.1 Structure and Morphology of Vortexed Hydrogels 23

3.3.2 pH Volume Phase Transitions of Macroporous Hydrogels 24

3.4 Conclusion 27

3.5 Acknowledgements 27

3.6 References 28

4.0 Debye Ring Diffraction Elucidation of 2D Photonic Crystal Self-Assembly and Ordering at the Air-Water Interface 32

4.1 Introduction 33

4.2 Experimental 35

4.2.1 Materials 35

4.2.2 Polymerization and Characterization of Monodisperse Negatively Charged Polystyrene Nanoparticles 35

4.2.3 2DPC Fabrication Using Needle Tip Flow Method 36

4.2.4 2DPC Debye Ring Diffraction Measurements 39

4.2.5 2DPC Ordering Analysis 42

4.3 Results and Discussion 43

4.3.1 Needle Tip Flow Nanoparticle Self-Assembly at the Air-Water Interface ... 43

4.3.2 Estimating 2DPC Order from Debye Ring Measurements 45

4.3.3 2DPC Ordering and Particle Spacing at the Air-Water Interface 50

4.3.4 Electrostatic Interactions of Charged Particles at the Air-Water Interface. 54

4.3.5 Mechanism of Self-Assembly for Close Packed Particle Arrays at the Air-WaterInterface 56

4.4 Conclusions 59

4.5 References 59

5.0 Mechanisms by which Organic Solvent Exchange Transforms Responsive Hydrogels into Responsive Organogels 68

5.1 Introduction 69

5.2 Experimental Section 73

5.2.1 Materials 73

5.2.2 Fabrication of BSA Hydrogel, Organogels, and Organogel Incubated in Water 73

5.2.3 Volume Phase Transition Measurements 75

5.2.4 UV Resonance Raman Spectroscopy of BSA Hydrogels and Organogels 76

5.2.5 NIR Absorption Measurements of BSA Organogel Water Content 76

5.2.6 Cryo-SEM of BSA Hydrogels and Water Incubated BSA Organogels 77

5.2.6.1 Preparation of BSA Solution, BSA Hydrogel, and Water Incubated BSA Organogel Samples for Cryo-SEM 77

5.2.6.2 Cryo-SEM of Frozen Hydrated BSA Hydrogels and Water Incubated Organogels 79

5.2.7 Titration of BSA Hydrogels and Water Incubated Organogels 80

5.3 Results and Discussion 81

5.3.1 Cryo-SEM Imaging of BSA Hydrogel Morphology and Topology 82

5.3.2 EG Solvent Exchange Causes Irreversible VPT 86

5.3.3 BSA Hydrogel, Organogel, and Water Incubated Organogel Secondary Structures 88

5.3.4 Water Content in BSA Organogels 91

5.3.5 Water Incubated BSA Organogel Morphology 94

5.3.6 Mechanism of Irreversible VPT Caused by EG Exchange 96

5.4 Conclusions 102

5.4.1 Funding 104

5.4.2 Notes 105

5.5 Acknowledgements 105

5.6 References 105

6.0 Summary of Important Findings and Future Directions 117

6.1 Future Directions 118

Appendix A Chapter 4 Supporting Information 119

Appendix A.1 Representative SEM Images of 2DPC for 409, 570, and 915 nm Particles for All Salt 119

Appendix A.2 Array Ordering Analysis 122

Appendix A.3 References 126

Appendix B Chapter 5 Supporting Information 128

Appendix B.1 Sample Holder for Cryo-SEM Frozen Hydrated Samples 128

Appendix B.2 UVRR Spectra of BSA Hydrogels and BSA Protein Monomers in Aqueous Solutions 129

Appendix B.3 UVRR Measurements and Protein Secondary Structure Determination 129

Appendix B.3.1 Fitting the BSA UVRR Spectra 129

Appendix B.3.2 Ψ Ramachandran Angle Calculation 130

Appendix B.3.3 Estimation of the Change in BSA Organogel α-Helix Populations 130

Appendix B.4 NIR Absorption of Ethylene Glycol-Water Solutions and BSA Organogels..... 131

Appendix B.4.1 Hydrophilic BSA Polymers Retain Much of Their Hydration Shell Waters in EG 134

Appendix B.5 References 136

List of Figures

Figure 2.1- Fabrication and dissolution of sacrificial PVA physically crosslinked hydrogel-2D PhC sensing hydrogel bilayer system. A solution of polymerizable monomers containing a UV initiator is deposited upon a 2D PhC attached to a coverslip (A). A coverslip is placed onto the solution (B) and the system photopolymerized (C)[1-8]. The 2D PhC sensing hydrogel is peeled off the glass slide (D) and partially immersed in a PVA solution (E). After two freeze-thaw cycles an interpenetrating PVA hydrogel forms within the sensing hydrogel and a pure PVA hydrogel forms below (F). The coverslips are removed (G). Upon heating, the PVA hydrogel dissolves leaving the original sensing hydrogel..... 6

Figure 2.2- Photographs of AA-Am-BIS sensing hydrogels. The top row show hydrogels fabricated without the use of PVA at 1%, 0.1%, and 0.05% (w/w) BIS crosslinker concentrations, (Figure 1 D to H). The second row shows a second set of sensing hydrogels fabricated using the PVA hydrogels, (Figure 1 D to G). The third row shows this second set of sensing hydrogels after the PVA hydrogel is removed (Figure 1 G to H). White scale bar lengths are 1 cm..... 8

Figure 2.3- Comparison of pH dependence of 2D array spacing of 2.5% AA-10% Am hydrogels prepared with 1%, 0.1%, and 0.05% concentrations of BIS crosslinker. Error bars indicate one standard deviation 10

Figure 2.4- Comparison of pH response of pH sensing 0.1% BIS hydrogel fabricated without a PVA hydrogel to that of a pH sensing hydrogel fabricated with an interpenetrating

PVA hydrogel bilayer system that was subsequently dissolved. Error bars indicate one standard deviation 11

Figure 3.1- Fabrication methods utilized to produce macroporous hydrogels. A-D. An inverse opal method utilizes polstrene nanoparticles to incorporate macropores. E-H. Alternatively, a vortexing method utilizes agitation to incorporate air bubble macropores. Macroporous hydrogels fabricated via both methods were dried and rehydrated, filling the air bubbles with water before the swelling ratio measurements. 20

Figure 3.2- SEM micrographs. A. Hydrogel fabricated using the vortexing method shows large pores of 10-100 μm in diameter. B. A non-macroporous hydrogel shows no pores 23

Figure 3.3- Comparison of pH dependence of the swelling ratio of macroporous hydrogels compared to a non-macroporous hydrogel. Error bars indicate one standard deviation. 24

Figure 3.4- Hydrogel responsivity dependence on Effective Relative Crosslinking Concentration (ERC). The data fit the relationship Responsivity $\approx 2*ERC^{-1.5}$ 25

Figure 4.1- Schematic of needle tip flow 2DPC fabrication at the air-water interface. 1) Addition of propanol lowers the surface tension of the particle dispersion. 2) The dispersion is spread on the water surface through a needle tip at a constant rate. The surface tension gradient forces the particles to the outer edge of the water surface. 3) Appendix A contains a link to a video showing 2DPC self-assembly on the water surface. The boundary between the self-assembled 2DPC and the particle-free pure water surface is visually evident. The radius of this boundary decreases as more

particles are spread onto the surface. 4) The 2DPC is lifted from the water surface by a microscope slide. 5) The wet slide with the lifted 2DPC is dried at room temperature. 6) After the water evaporation, the particles on the slide surface adhere to the microscope slide. 38

Figure 4.2- (A) Illustration showing the angles of diffraction for 406 nm light travelling through water, θw, and air, θa. The distance the light travels in each medium, hw and ha determines the final Debye ring diameter. (B) Photograph of the Debye ring. ... 40

Figure 4.3- Cartoon showing the angles of diffraction for 406 nm light travelling through water, θw, and air, θa. The distance the light travels in each medium, hw and ha determines the final Debye ring diameter. 41

Figure 4.4- SEM micrographs (1a - 3a) of 2DPC of 915 nm PS particles prepared on solutions of increasing salt concentrations (pure water, 0.01 M NaCl and 0.1 M NaCl). (1b - 3b) Photographs of polychromatic light diffraction of 2DPC prepared on solutions of increasing salt concentrations. The diffraction polychromatic dispersion becomes more diffuse and less intense at larger salt concentrations. (1c - 3c) Photographs of Debye ring diffraction of normally incident 405 nm monochromatic light at increasing salt concentrations. 44

Figure 4.5- SEM images of 915 nm particle 2DPC (A) self-assembled on pure water and (B) on 0.1 M NaCl. (A)shows a well ordered 2DPC where the particle spacings show little variation. (B) shows a highly disordered 2DPC. The areas outlined in red are where the particle arrays assembled into a square lattice instead of a hexagonal lattice. Areas highlighted in blue show regions that are randomly oriented with little crystalline order. 47

Figure 4.6- Dependence of Debye ring widths of 570 nm and 915 nm 2DPC as a function of the NaClconcentration..... 48

Figure 4.7- Particle spacing change, $\Delta a = a[NaCl] - a_{water}$, for 570 and 915 nm 2DPC as a function of NaCl concentration. Particle Spacing is calculated from the Debye ring diameter measurements. 48

Figure 4.8- Dependence of the 2DPC order parameter, $\kappa/\kappa o$ on salt concentration for 409, 570 and 915 nm particle diameters. The horizontal line indicates $\kappa/\kappa o = 1.5$, above which disorder is present. Error bars indicate 95% confidence intervals. 50

Figure 4.9- Debye ring width, w of 915 nm diameter particle 2DPC at different stages of fabrication. 2DPC were fabricated by self-assembly of 915 nm PS particles on pure water, 0.01 M NaCl and 0.1 M NaCl. Errorbars represent one std. dev. 52

Figure 4.10- Dependence of 2DPC particle spacings for 915 nm diameter particle 2DPC at different stages of fabrication. The Debye ring was measured for a 2DPC at the air-water interface of the crystallization dish (onliquid), at the air-water interface after the 2DPC and a thin water layer are transferred to a slide (wet slide), and after the 2DPC is dried on the slide (dry slide). 2DPC were fabricated by self-assembly of 915 nm PS particles on pure water, and in the presence of 0.01M NaCl and 0.1M NaCl. Error bars represent one standard deviation..... 53

Figure 4.11- Confocal microscope image of 915 nm particles at the air-water interface fabricated using the NTF method. The levels, thresholds, and sharpness in the image were edited using GIMP software so that theparticles are clearly visible..... 54

Figure 4.12- Zeta-potentials (mV) for 409, 570, and 915 nm diameter anionic polystyrene particles in solutions as a function of NaCl concentration. Error bars indicate one standard deviation. 58

Figure 5.1- (A) BSA protein structure showing lysine residues highlighted in red. Structure obtained from RCSB Protein Data Bank, 3V03. Image made using PyMol software. (B) One of the possible glutaraldehyde interprotein cross-linking reactions; the aldehyde and lysine amine group form a Schiff base that covalently links the two proteins..... 80

Figure 5.2- Cryo-SEM of frozen hydrated BSA hydrogels (A−D) and of BSA monomer solutions prior to polymerization (E), and a non-Cryo-SEM of a BSA hydrogel that was freeze-dried (F). Frozen hydrated BSA hydrogels are shown at 20K magnification (A); 70K magnification (B), red arrow points to vitreous ice remaining in the sample; 70K magnification (C), red box indicates the area that is enlarged in Figure 2D. (D) Enlarged area from Figure 2C where the thin BSA polymer strands are clearly visible. The red line highlights one of the measured protein polymer strand lengths. (E) Cryo-SEM of BSA monomer solutions before glutaraldehyde polymerization: 70K magnification. (F) Non-Cryo-SEM of freeze-dried BSA hydrogel: 70K magnification. 83

Figure 5.3- Proposed BSA hydrogel topology based on the Figure 5.2 Cryo-SEM images. Black arrows point to polymer cross-links, where a BSA forms interprotein cross-links that connect two polymer strands. Red arrows point to the different protein polymer strands that are colored red, green, and pink. 84

Figure 5.4- Dependence of the BSA polymer volume fraction, ϕ (left axis, black squares), and the swelling ratio, V/V_i (right axis, red circles), as a function of mobile phase composition during the stepwise water to EG exchange. The breaks in the graph illustrate the stepwise solvent exchange from pure EG back to pure water. 86

Figure 5.5- UVRR spectra of BSA hydrogel (blue), BSA organogel (red), and BSA hydrogel−organogel difference spectrum (green). The broad AmIII[3] band at ∼1240−1270 cm^{-1} results from the distribution of peptide backbone Ψ angles used to calculate the protein secondary structure. Spectral differences at ∼1460 cm^{-1} result from the subtraction of an intense EG Raman peak in the BSA organogel. 88

Figure 5.6- UVRR spectra of (blue) BSA hydrogel, (red) BSA organogel incubated in water, and (green) BSA hydrogel−water organogel incubated in water difference spectrum. 90

Figure 5.7- Cryo-SEM images comparing the morphology of BSA hydrogels (A, B) to that of the water incubated BSA organogels (C, D) after 40 min of sublimation and the application of a 2.5 nm Pt sputter coat. (A) BSA hydrogel; 70K magnification. (B) Enlarged area of BSA hydrogel, indicated by the red box in Figure 5.7A. (C) Water incubated BSA organogel; 50K magnification. (D) Enlarged area of water incubated BSA organogel, indicated by the red box in Figure 5.7C 93

Figure 5.8- Titration curve of the BSA hydrogel before the water to EG exchange (blue), and the water incubated BSA organogel after the water to EG exchange and EG to water exchange (red). The titration is normalized to the number of moles of H^+ added to solution per mole of BSA in the sample. 95

Figure 5.9- Illustration of the proposed kinetic two-stage phase separation of the BSA polymer that occurs during the water to EG exchange. The first stage (1a−1b) involves a fast coil-to-globule transition of the BSA polymer strands. This coil-to-globule transition decreases the distance between BSA polymer strands. Polymerized BSA on different protein polymer strands can form interprotein interactions where the BSA polymer strands are in close proximity, highlighted by the blue circles in stage 1b. These additional interprotein polymer strand interactions formed during phase separation increase the polymer cross-link density through physical polymer cross-linking, thus, preventing organogel reswelling. The second slower stage (2a−2b) of the phase separation involves knotting of the localized globules in the network and entanglement of the BSA polymer strands. This second stage further increases the BSA polymer density, resulting in the very dense BSA polymer phase observed in the water incubated organogel Cryo-SEM. 97

Appendix Figure A.1- 570 nm Diameter 2DPC SEM micrographs of 2DPC fabricated by self-assembly of 915 nm diameter charged polystyrene particles at the air-water interface of electrolyte solutions containing NaCl. A. Pure Water B. 0.001 M NaCl C 119

Appendix Figure A.2- SEM micrographs of 2DPC fabricated by self-assembly of 570 nm diameter charged polystyrene particles at the air-water interface of electrolyte solutions containing NaCl. A. Pure Water B. 0.001 M NaCl C. 0.01 M NaCl D. 0.1 M NaCl E. 1 M NaCl 120

Appendix Figure A.3- SEM micrographs of 2DPC fabricated by self-assembly of 409 nm diameter charged polystyrene particles at the air-water interface of electrolyte

solutions containing NaCl. A. Pure Water B. 0.001 M NaCl C. 0.01 M NaCl D. 0.1 M NaCl E. 1 M NaCl 121

Appendix Figure A.4- 2D Pair Correlation function for a perfect close-packed 2D array of circles with 409 nmdiameters and 2DPC of 409 nm particles fabricated on pure water and on 0.001, 0.01, 0.1, and 1M NaCl solutions..... 123

Appendix Figure A.5- 2D Pair Correlation function for a perfect close-packed 2D array of circles with 570 nmdiameters and 2DPC of 570 nm particles fabricated on pure water and on 0.001, 0.01, 0.1, and 1M NaCl solutions..... 124

Appendix Figure A.6- 2D Pair Correlation function for a perfect close-packed 2D array of circles with 915 nmdiameters and 2DPC of 915 nm particles fabricated on pure water and on 0.001, 0.01, 0.1, and 1M NaCl solutions..... 125

Appendix Figure A.7- The first peak of the FFT of g(r)-1 plotsfor 2DPC arrays of 413nm (top), 570nm (middle),and 915nm (bottom). 126

Appendix Figure B.1- Cryo-SEM sample holder. The sample cavity on the right contains one of the Ted Pella brass planchets that is used to freeze and fracture the hydrogel or organogel samples. The sample cavity on the left is empty..... 128

Appendix Figure B.2- UVRR measurements and protein secondary structure determination fitting the BSA UVRR spectra 129

Appendix Figure B.3- NIR absorbance of EG and its water solutions in a 5 mm path length quartz cuvette between 1400 nm to 2000 nm. (a) Spectra of pure EG with 0, 5, 10, 15, 20, and 25 µL water added (b) Difference Spectra of (EG/water solution) - EG spectra. 132

Appendix Figure B.4- (EG+water)-EG difference spectra absorbance at 1915 nm as a function of waterconcentration. The slope of the best fit line is 0.47 A.U. M^{-1}. 133

Appendix Figure B.5- The 1400-2000 nm NIR absorbance of a single and double layer BSA organogel film. 134

Appendix Figure B.6- BSA protein structure from X-ray crystallography (PDB: 3V03)[13]. Hydrophilic aminoacid residues are colored blue (Lys, Arg, Asp, Glu, His, Ser, Thr, Asn, Gln, Cys); hydrophobic amino acid residues are colored red (Gly, Ala, Leu, Ile, Met, Val, Phe, Tyr, Trp, Pro)..... 135

Preface

I would like to thank the many people. I would like to thank my mother, Sharon Eagle, for her emotional support. I would like to thank my Father for his emotional support and our discussions about electronics. The Asher research group was a great inspiration for me. The scientific discussions we had were of great help. I want to thank Dr. Natasha Smith for mentoring me and being an excellent collaborator. Last but not least, I would like to thank Dr. Sanford Asher for being my research advisor. He has put up with far too many of my flaws. I want to express my appreciation for all of his hard work to help me.

1.0 Introduction, Motivation

2D photonic crystal hydrogel sensors are composed of 2D photonic crystals embedded in volume responsive hydrogels. The responsive hydrogels utilize polymers in water. The hydrogel changes volume due to changing concentrations of analytes such as proteins, enzymes, and small molecules. We measure the hydrogel volume by using an embedded 2D Photonic Crystal (2DPhC). 2DPhCs utilizes hexagonal monolayers of polystyrene spheres that diffract light at wavelengths that depend upon the 2DPhC particle spacing.[1]

Research on 2D photonic crystal hydrogel sensors will enable advances in a wide range of fields including healthcare, industrial/home safety, and chemical/biological weapon detection. 2D Photonic Crystal sensors could function as point of care sensors. Point of care sensors have improved the quality of life of millions. For example, blood glucose and pregnancy point of care sensors enable people to monitor their health at home, allowing for better healthcare decisions.

My work aims to improve 2D photonic crystal hydrogel sensors for use as a point of care sensors. I will enhance the dynamic range of the sensor by investigating low-crosslinking concentrations and macroporous hydrogels. I will explore the 2D photonic crystal fabrication process to improve the understanding of 2D Photonic crystal self-assembly. I will investigate the mechanisms by which we convert hydrogels to organogels to improve the air stability of our sensors

1.1 References

(1) Coukouma, A. E.; Smith, N. L.; Asher, S. A. *Analyst* **2015**, *140*, 6517-6521.

(2) Smith, N. L.; Coukouma, A. E.; Wilson, D. C.; Ho, B.; Gray, V. P.; Asher, S. A. *ACS Applied Materials & Interfaces* **2019**.

(3) Cai, Z.; Kwak, D. H.; Punihaole, D.; Hong, Z.; Velankar, S. S.; Liu, X.; Asher, S. A. *Angewandte Chemie International Edition* **2015**, *54*, 13036-13040.

(4) Cai, Z.; Zhang, J.-T.; Xue, F.; Hong, Z.; Punihaole, D.; Asher, S. A. *Analytical Chemistry* **2014**, *86*, 4840-4847.

(5) Walker, J. P.; Kimble, K. W.; Asher, S. A. *Analytical and bioanalytical chemistry* **2007**, *389*, 2115-2124.

(6) Walker, J. P.; Asher, S. A. *Analytical chemistry* **2005**, *77*, 1596-1600.

(7) Cai, Z.; Luck, L. A.; Punihaole, D.; Madura, J. D.; Asher, S. A. *Chemical Science* **2016**, *7*, 4557-4562.

(8) Lee, M.-C.; Kabilan, S.; Hussain, A.; Yang, X.; Blyth, J.; Lowe, C. R. *Analytical chemistry* **2004**, *76*, 5748-5755.

(9) Zhang, J.-T.; Wang, L.; Luo, J.; Tikhonov, A.; Kornienko, N.; Asher, S. A. *Journal of the American Chemical Society* **2011**, *133*, 9152-9155.

(10) Goponenko, A. V.; Asher, S. A. *Journal of the American Chemical Society* **2005**, *127*, 10753-10759.

(11) Ye, B.-F.; Zhao, Y.-J.; Cheng, Y.; Li, T.-T.; Xie, Z.-Y.; Zhao, X.-W.; Gu, Z.-Z. *Nanoscale* **2012**, *4*, 5998-6003.

(12) Cai, Z.; Sasmal, A.; Liu, X.; Asher, S. A. *ACS Sensors* **2017**, *2*, 1474-1481.

2.0 Removable Interpenetrating Network Enables Highly-Responsive 2-D Photonic Crystal Hydrogel Sensors

This work was previously published in Sensors and Actuators B as Coukouma, A. E.; Smith, N. L.; Asher, S. A. *Analyst* **2015**, *140*, 6517-6521

Author Contributions: A.E.C. performed all experimental design and work. N.L.S. assisted with initial experiential design. The manuscript was prepared by A.E.C. with assistance from N.L.S. and S.A.A.

Responsive hydrogels functionalized with molecular recognition agents can undergo large volume changes upon interactions with specific chemical species. These responsive hydrogels can function as chemical sensing materials if the hydrogel volumes are monitored by using devices such as photonic crystals (PhC). An important criterion of merit is the responsiveness of these sensing hydrogels. Generally, hydrogel responsiveness is inversely proportional to the hydrogel crosslink density because the elastic constants scale with the crosslink density. The responsivities of these hydrogel sensors dramatically increase as their hydrogel crosslinker concentrations decrease. Unfortunately, the resulting highly responsive hydrogels become fragile at low crosslink densities, and are hard to fabricate and utilize. To temporarily increase the mechanical strengths of these highly responsive hydrogels we developed a method to incorporate a removable reinforcing interpenetrating hydrogel network. We demonstrate the utility of this approach by incorporating an interpenetrating PVA hydrogel within a weak, low crosslinked pH sensitive hydrogel through a freeze-thaw process. These interpenetrating PVA hydrogels are indefinitely stable at room temperature, but easily dissolved on transient heating to 70°C. The pH sensing hydrogel response is unaffected by this incorporation and subsequent dissolution of the

interpenetrating PVA hydrogel. These sacrificial hydrogels enable the fabrication and utilization of highly responsive hydrogel sensing materials.

2.1 Introduction

Hydrogels are polymer networks that stabilize a water mobile phase. The unusual properties of hydrogels enable their applications as responsive smart materials. Responsive hydrogels have been used in applications such as sensors[2-7], mechanical actuators[8,9], and for drug delivery.[8,10-12] Chemical sensors have been fabricated that utilize hydrogel volume phase transitions (VPT); the volume of the hydrogel changes in response to chemical or physical stimuli. We, as well as others, fabricated hydrogels to sense pH[6,13-16], heavy metals[2,5-7,16,17], humidity[18], and biological targets such as creatinine[14] and glucose.[1,2,19]

A wide range of methods have been developed to monitor the VPT of hydrogels. Originally measurements were conducted by measuring the size of the hydrogel.[20,21] Later, groups developed the use of photonic crystals (PhC)[7,14,16,18,22-26] and holograms[1,13] to measure hydrogel VPT. Our group pioneered the use of 2D[4,24,27-29] and 3D[2,5,7,16,17,19,22,] PhC embedded within responsive hydrogels to monitor the VPT.[30] PhC can be used to optically monitor the volume of the hydrogel by measuring the wavelength or the angle of light diffracted. The diffraction depends on the spacing of the attached PhC periodicity which depends on the responsive hydrogel volume.[2,31]

Chemically responsive hydrogels can be fabricated where their VPT are selectively induced by specific chemical species. These hydrogels change volume in response to chemically induced osmotic pressures. The three typical sources of hydrogel osmotic pressures are osmotic

pressures due to the free energy of mixing (Π_m), due to the elastic free energy (Π_{el}), and due to the ionic free energy (Π_i).[32] Equilibrium occurs when the total osmotic equals zero ($\Pi_m + \Pi_{el} + \Pi_i = 0$).

The elastic free energy osmotic pressure is *roughly* proportional to the crosslink density times the extent to which the hydrogel volume departs from the synthesized hydrogel volume. The hydrogel VPT volume response due to changes in the free energy of mixing osmotic pressure, and/or due to changes in the immobilized charge-induced osmotic pressure, will increase as the crosslinker concentration decreases. The hydrogel becomes more volume responsive as the elastic restoring force is decreased. Unfortunately, decreasing the crosslinker concentrations also decreases the hydrogel mechanical strength.[33] Mechanically weak hydrogels are difficult to fabricate and handle.

The utilization of mechanically weak hydrogels requires hydrogel reinforcement. Unfortunately, structural reinforcement of mechanically weak hydrogels will reduce the magnitude of their VPT response. In order to utilize highly responsive but weak materials we developed a method to transiently reinforce the system to enable its fabrication and handling. We then remove the reinforcing PVA hydrogel restoring the high responsivity. As shown below we incorporate an interpenetrating hydrogel of physically crosslinked poly(vinyl alcohol) (PVA) within a weak highly responsive hydrogel. Uncrosslinked PVA has been used as a water soluble lift off layer.[34] PVA is easily physically crosslinked into indefinitely stable hydrogels (at room temperature) by

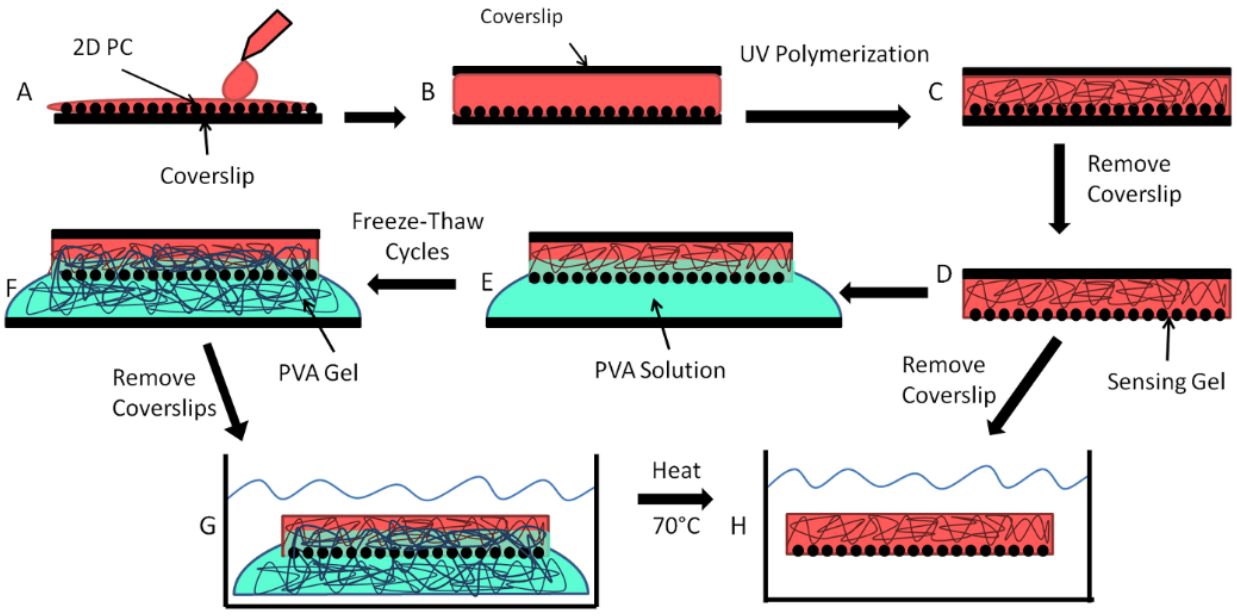

Figure 2.1- Fabrication and dissolution of sacrificial PVA physically crosslinked hydrogel-2D PhC sensing hydrogel bilayer system. A solution of polymerizable monomers containing a UV initiator is deposited upon a 2D PhC attached to a coverslip (A). A coverslip is placed onto the solution (B) and the system photopolymerized (C)[1-8]. The 2D PhC sensing hydrogel is peeled off the glass slide (D) and partially immersed in a PVA solution (E). After two freeze-thaw cycles an interpenetrating PVA hydrogel forms within the sensing hydrogel and a pure PVA hydrogel forms below (F). The coverslips are removed (G). Upon heating, the PVA hydrogel dissolves leaving the original sensing hydrogel.

freezing aqueous PVA solutions into cryogels.[22,35,36] Upon freezing the PVA polymer chains form crystallites through hydrogen bonding. The crystals formed have the same structure as pure PVA crystals.[37] The crystallites are ~7 nm thick and spaced 15-20 nm apart.[37] The crystallites physically crosslink multiple PVA chains, forming a mechanically robust cryogel. PVA crystallites are stable at room temperature[36, 37]. At 70°C, the PVA crystallites rapidly melt, dissolving the PVA cryogel.[22]

2.2 Results and Discussion

Figure 2.1 shows the fabrication of the 2D PhC sensing hydrogels and the incorporation of interpenetrating PVA hydrogels. The 2D-PhC sensor is fabricated by depositing the polymerizable monomer solution on a slide containing a 2D PhC (Figure 2.1A). A coverslip is placed on top of the solution and the solution is polymerized by UV light (Figure 2.1B to C).[18,23,30] After the sensor hydrogel is polymerized, the coverslip on the 2D array side is removed (Figure 2.1C and D).

In this case we form a reinforcing interpenetrating physically crosslinked hydrogel within the sensing hydrogel which is attached to a pure PVA hydrogel substrate. This is accomplished by partially immersing the mechanically weak, highly-responsive hydrogel in a PVA solution (Fig. 2.1E). The PVA polymer is allowed to diffuse into the sensing hydrogel and then the PVA is physically crosslinked by a freeze-thaw process to form a PVA interpenetrating sensing hydrogel-pure PVA hydrogel bilayer system (Figure 2.1F). This physically crosslinked PVA bilayer system is robust and is easily handled (Figure 2.1G). The interpenetrating and pure PVA crosslinked hydrogel bilayers are easily dissolved away by heating the system briefly for 10 min to 70°C (Figure 2.1H).

We prepared highly pH responsive hydrogels by incorporating acrylic acid (AA) within acrylamide (Am) hydrogels crosslinked with low concentrations of bisacrylamide (BIS). The interpenetrating PVA cryogel was incorporated to mechanically strengthen the mechanically weak pH sensing hydrogel. Bulk polyacrylic acid has a pK_a ~4.7[3] and increasingly deprotonates as the pH increases to form carboxylates that immobilize counterions, resulting in an osmotic pressure

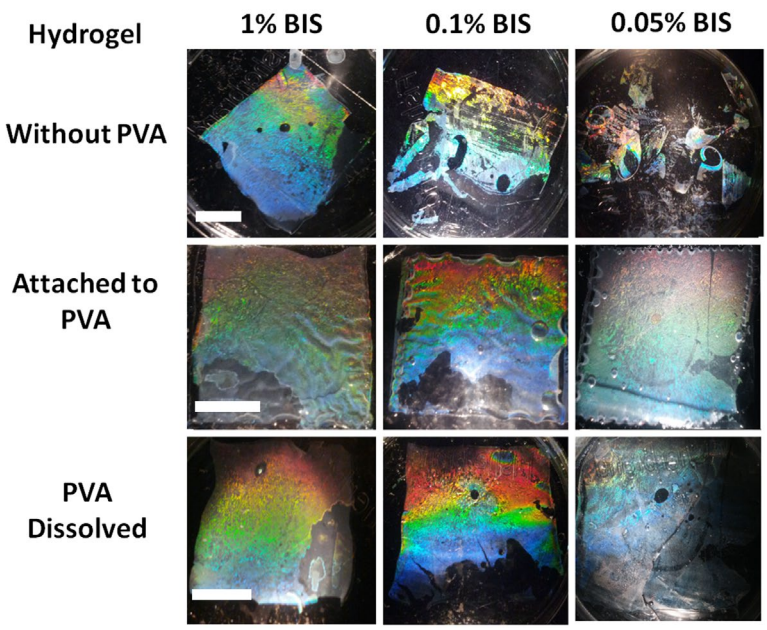

Figure 2.2- Photographs of AA-Am-BIS sensing hydrogels. The top row show hydrogels fabricated without the use of PVA at 1%, 0.1%, and 0.05% (w/w) BIS crosslinker concentrations, (Figure 1 D to H). The second row shows a second set of sensing hydrogels fabricated using the PVA hydrogels, (Figure 1 D to G). The third row shows this second set of sensing hydrogels after the PVA hydrogel is removed (Figure 1 G to H). White scale bar lengths are 1 cm.

that swells the hydrogel.[3,15] We sensitively monitor the hydrogel volume by monitoring the light diffracted from the embedded 2D PhC.

These poly-AA-Am-BIS hydrogels swell as the carboxyl groups deprotonate to form carboxylates at higher pH values.[38] The extent of hydrogel swelling increases as the crosslinker concentration decreases. Unfortunately, the decreasing crosslinker concentration decreases the hydrogel mechanical strength[33]. These hydrogels become difficult to fabricate and handle. To enable the fabrication and utilization of minimally crosslinked, more highly responsive hydrogels, we incorporated the poly(vinyl alcohol) cryogels to temporarily mechanically reinforce the hydrogel.

Figure 2.2 shows photographs of pH sensing hydrogels that were polymerized with decreasing BIS crosslinker concentrations of 1%, 0.1%, and 0.05%. The top row of pictures show hydrogels fabricated without the PVA hydrogels as depicted in Figure 2.1 going from D to H without steps E-G. The low crosslink density 2D PhC pH sensing hydrogels are fragile and easily tear during fabrication. For example, the top left 1% BIS hydrogel is easily removed from the coverslip, while the 0.1% BIS hydrogel tore easily during handling, as shown in the top center of Figure 2.2. The very fragile 0.05% BIS hydrogels tore into multiple small pieces because of its mechanical weakness (Figure 2.2 top right).

Incorporation of the interpenetrating PVA hydrogel results in a more mechanically robust hydrogel bilayer system as shown in the middle row of photographs. The resulting bilayer hydrogel systems show significant wrinkling due to the differential swelling of the sensing interpenetrating PVA hydrogel composite compared to the pure PVA hydrogel. Wrinkling relieves strain caused by the differential swelling in the hydrogel bilayers.[39]

These interpenetrating PVA-sensing hydrogel- PVA hydrogel bilayers are stable for over three months in pH 3.18 buffer at room temperature. The bottom row of Figure 2.2 shows the resulting sensing hydrogels after PVA hydrogel dissolution at 70° C (Figure 2.1G to H) most notable is that the 0.05% BIS hydrogel remains intact.

Figure 2.3 shows the pH dependence of the inter-particle spacing of a series of 2D PhC AA-Am-BIS hydrogel sensors polymerized at decreasing crosslinker concentrations of 1%, 0.1% and 0.05%. As expected, the sensing hydrogel pH responsivities increase as the crosslinker concentration decreases. At pH 3.76 the particles spacing is 646 ±2 nm for the 1% BIS hydrogel, 970±4 nm for the 0.1% BIS hydrogel, and spacing increases to 746 ±4 nm for the 1% BIS

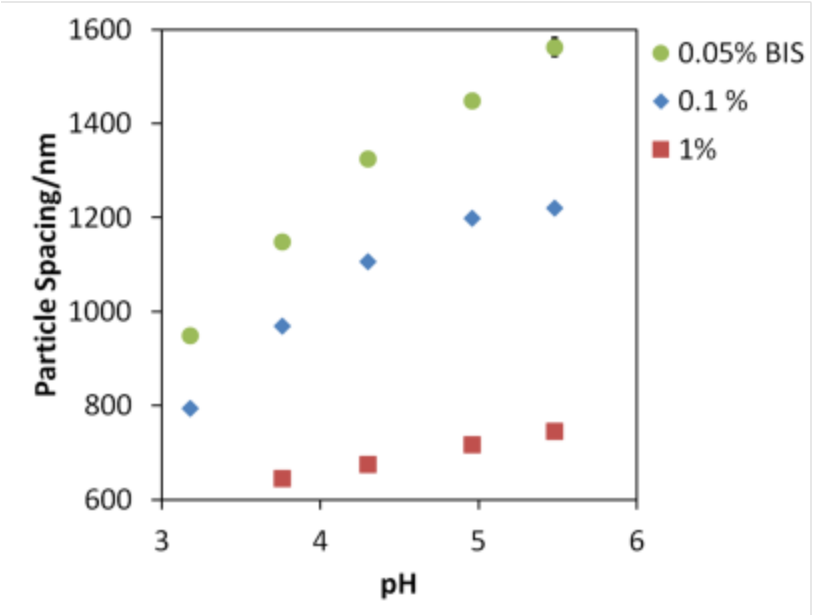

Figure 2.3- Comparison of pH dependence of 2D array spacing of 2.5% AA-10% Am hydrogels prepared with 1%, 0.1%, and 0.05% concentrations of BIS crosslinker. Error bars indicate one standard deviation

hydrogel,1148±8 nm for the 0.05% BIS hydrogel. At pH 5.48 the particle spacing is 1220±7 nm for the 0.1% BIS hydrogel, and 1562±18 nm for the 0.05% BIS hydrogel. Thus, between pH 3.76 to 5.48 the particle spacing increases by 100 nm for a 1% BIS hydrogel, 251 nm for a 0.1% BIS hydrogel, 414 nm for a 0.05% BIS hydrogel. The pH sensing hydrogels increase their responsivity by four-fold as the crosslinker concentration decreases 20-fold from 1% BIS to 0.05%.

The linear response observed over this pH range was previously observed[3,6,15].This volume response is of complex origin. The hydrogel changes volume in response to the sum of changes in the ionic free energy, the free energy of mixing, and the restoring elastic force.[32] The equilibrium between these factors gives rise to a linear response to the titration of the carboxylate groups.

We examined the impact of the incorporation and dissolution of the PVA hydrogel on the response of a pH responsive 0.1% BIS hydrogel. A single 2D PhC AA-Am-BIS hydrogel was polymerized and cut in half. One half was stored in pH 3.18 buffer while the other had a PVA cryogel incorporated. Both hydrogels were similarly heated for 15 min at 70 °C. We independently demonstrated that this 15 min heating does not affect the pH response of the sensing hydrogels. We observe essentially identical pH responses of these two pH responsive hydrogels (Figure 2.4).

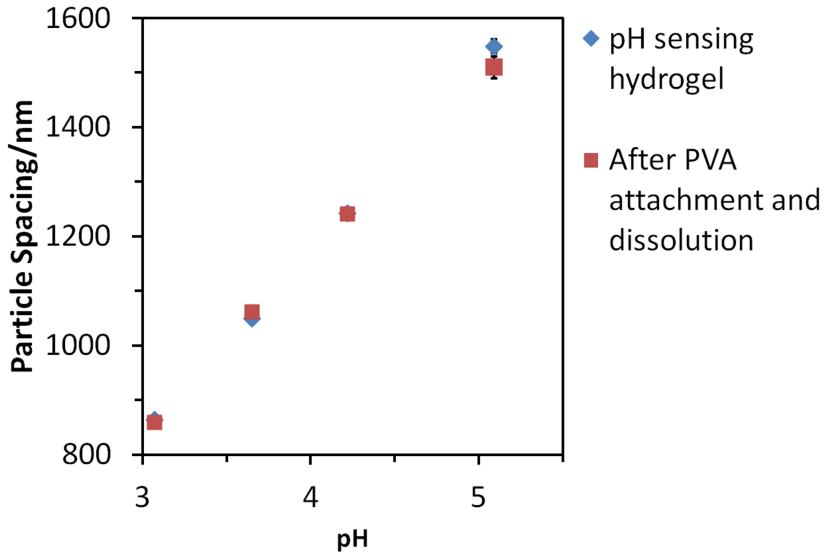

Figure 2.4- Comparison of pH response of pH sensing 0.1% BIS hydrogel fabricated without a PVA hydrogel to that of a pH sensing hydrogel fabricated with an interpenetrating PVA hydrogel bilayer system that was subsequently dissolved. Error bars indicate one standard deviation

The observed bright visible diffraction in Figure 2.2 and a sharp well defined Debye ring after the PVA is dissolved indicates that the attached 2D PhC is well ordered. Neither the hydrogel sensor response nor the attached 2D PhC is irreversibly adversely affected by the incorporation and dissolution of the PVA hydrogel.

2.3 Experimental

2.3.1 **Materials**

Igracure 2959, DMSO, Acrylamide (Am), 1-Propanol and N-N`-Methylenebisacrylamide (BIS) were acquired from Sigma Aldrich (≥99% purity) and used as received. Acrylic acid (AA) was acquired from Sigma Aldrich and purified through distillation. Glacial acetic acid was

supplied by Fisher and used as received. Sodium acetate was acquired from EM Science and used as received. 98% mole hydrolyzed 78,000 MW Poly(vinyl alcohol) (PVA) was acquired from Polysciences Inc. and used as received.

2.3.2 **Fabrication of pH Sensitive Hydrogels**

2D photonic crystal array (2D PhC) pH sensing hydrogels were fabricated as previously described.[4] 490 nm diameter polystyrene particles were synthesized by emulsifier-free polymerization.[40] A 2D PhC was fabricated by carefully layering a 3:1 volume dispersion of these 490 nm polystyrene particles (15 wt%) in 1-propanol onto a water surface.[27] As shown previously[27] these particles self-assemble on the water surface into a 2D PhC. The 2D PhC on the water surface was transferred to a glass slide by inserting the slide under the 2D PhC and carefully lifting it.

The sensing hydrogel monomer solution was prepared by adding 20 μL of a photoinitiator solution of 33% (w/w) Irgacure 2959 in DMSO to a 1 mL aqueous solution containing 10% (w/w) Am, 2.5% AA (w/w), and between 1% to 0.05% (w/w) BIS crosslinker in a pH 3.18, 0.1 M acetate buffer. 130 μL of this monomer solution was deposited onto the glass slide attached to the 2D PhC (Figure 2.1A). A coverslip was placed on top and the solution was UV polymerized for 15 min by illuminating the solution with a UV lamp (UVGL-55, UVP) to form a 100 μm thick 2D PhC BIS-AA-Am hydrogel (Figure 2.1B).

One of the glass coverslips was removed (Figure 2.1C to D). The adhesion of the hydrogel to the opposite cover slip enabled this removal. The adhesion to the opposite coverslip distributes the mechanical strain from the coverslip removal evenly over the hydrogel. An interpenetrating PVA hydrogel-bilayer system was fabricated within and around the 2D PhC sensing hydrogel by partially immersing the 2D PhC sensing hydrogel in a 7% (w/w) aqueous PVA solution (Figure

2.1E). The system was temperature cycled twice by cooling to -20°C for 2 hr and thawing for 2 hr at room temperature. At the lower temperature the PVA forms small crystallites that physically crosslink the PVA into an interpenetrating network within the 2D PhC sensing hydrogel and an adjacent pure PVA hydrogel.

The PVA hydrogel was dissolved by heating the system in a pH 3.18 acetate buffer to 70 °C (Figure 2.3G and H). The dissolved PVA solution was removed and the 2D PhC pH sensor was washed with and stored in a room temperature pH 3.18 acetate buffer.

2.3.3 **pH Sensing**

The 2D PhC pH sensing response was studied in acetate buffers at concentrations between 0.01 M to 0.1 M fabricated using sodium acetate and glacial acetic acid and adjusted to maintain a constant ionic strength of 0.01 M. Changes in hydrogel volume due to pH changes were monitored by measuring the 2D PhC particle spacing as previously described.[4] A 532 nm laser pointer illuminated the 2D PhC sensing hydrogel at normal incidence. The light is diffracted by the 2D PhC at an angle determined by the particle spacing. This would give rise to six diffraction spots for a perfectly ordered 2D array. However, the randomly oriented 2D PhC micro-domains diffract the light to form a Debye ring.

The angle of diffraction, α was determined from the Debye ring diameter from $\alpha = \tan^{-1}(D/2H)$ where D is the diameter of the Debye ring and H is the distance between the measured ring and the illuminated hydrogel. The particle spacing was determined by the Bragg diffraction condition for 2D diffraction: $M\lambda = (\sqrt{3}/2)d(\sin\alpha)$. M is the order of the diffraction, λ is the wavelength of illumination or 532 nm, and d is the nearest neighbour particle distance.

2.4 Conclusions

Incorporation of interpenetrating PVA hydrogels enables the utilization of highly responsive, but mechanically weak sensing hydrogels. These interpenetrating PVA hydrogels can easily be removed by incubation at 70° C. This process neither alters the responsivity of the hydrogels nor significantly affects the attached 2D PhC. This approach of temporarily reinforcing weak hydrogels will enable utilization of highly responsive hydrogel sensors that were previously inaccessible due to their fragility.

2.5 Acknowledgements

We would like to thank the Defense Threat Reduction Agency (DTRA) for funding this research under grants no. HDTRA1-10-1-0044 and HDTRA1-15-1-0038.

2.6 References

(1) Joannopoulos, J. D.; Johnson, S. G.; Winn, J. N.; Meade, R. D. Photonic crystals: molding the flow of light; Princeton university press, 2011.

(2) Coukouma, A. E.; Smith, N. L.; Asher, S. A. Analyst 2015, 140, 6517-6521.

(3) Holtz, J. H.; Asher, S. A. Nature 1997, 389, 829-832.

(4) Richter, A.; Paschew, G.; Klatt, S.; Lienig, J.; Arndt, K.-F.; Adler, H.-J. P. Sensors 2008, 8, 561-581.

(5) Zhang, J.-T.; Chao, X.; Liu, X.; Asher, S. A. Chem. Commun. 2013, 49, 6337-6339.

(6) Goponenko, A. V.; Asher, S. A. J. Am. Chem. Soc. 2005, 127, 10753-10759.

(7) Reese, C. E.; Baltusavich, M. E.; Keim, J. P.; Asher, S. A. Anal. Chem. 2001, 73, 5038-5042.

(8) Asher, S. A.; Peteu, S. F.; Reese, C. E.; Lin, M.; Finegold, D. Analytical and bioanalytical chemistry 2002, 373, 632-638.

(9) DeRossi, D.; Kajiwara, K.; Osada, Y.; Yamauchi, A. Fundamentals and Biomedical Applications, Plenum Press, New York 1991.

(10) Osada, Y.; Okuzaki, H.; Hori, H. Nature 1992, 355, 242-244.

(11) Hoffman, A. S. Advanced drug delivery reviews 2012, 64, 18-23.

(12) Jeong, B.; Kim, S. W.; Bae, Y. H. Advanced drug delivery reviews 2002, 54, 37-51.

(13) Qiu, Y.; Park, K. Advanced drug delivery reviews 2012, 64, 49-60.

(14) Marshall, A. J.; Blyth, J.; Davidson, C. A.; Lowe, C. R. Anal. Chem. 2003, 75, 4423-4431.

(15) Sharma, A. C.; Jana, T.; Kesavamoorthy, R.; Shi, L.; Virji, M. A.; Finegold, D. N.; Asher, S. A. J. Am. Chem. Soc. 2004, 126, 2971-2977.

(16) Lee, Y. J.; Braun, P. V. Adv. Mater. 2003, 15, 563-566.

(17) Muscatello, M. M. W.; Asher, S. A. Adv. Funct. Mater. 2008, 1186, 18-18.

(18) Asher, S. A.; Sharma, A. C.; Goponenko, A. V.; Ward, M. M. Anal. Chem. 2003, 75, 1676-1683.

(19) Smith, N. L.; Hong, Z.; Asher, S. A. Analyst 2014, 139, 6379-6386.

(20) Lee, M.-C.; Kabilan, S.; Hussain, A.; Yang, X.; Blyth, J.; Lowe, C. R. Anal. Chem. 2004, 76, 5748-5755.

(21) Ward Muscatello, M. M.; Stunja, L. E.; Asher, S. A. Anal. Chem. 2009, 81, 4978-4986.

(22) Gehrke, S. H.; Cussler, E. L. Chem. Eng. Sci. 1989, 44, 559-566.

(23) Otake, K.; Inomata, H.; Konno, M.; Saito, S. Macromolecules 1990, 23, 283-289.

(24) Asher, S. A.; Kimble, K. W.; Walker, J. P. Chem. Mater. 2008, 20, 7501-7509.

(25) Cai, Z.; Zhang, J.-T.; Xue, F.; Hong, Z.; Punihaole, D.; Asher, S. A. Anal. Chem. 2014, 86, 4840-4847.

(26) Zhang, J.-T.; Wang, L.; Luo, J.; Tikhonov, A.; Kornienko, N.; Asher, S. A. J. Am. Chem. Soc. 2011, 133, 9152-9155.

(27) Kang, Y.; Walish, J. J.; Gorishnyy, T.; Thomas, E. L. Nat Mater 2007, 6, 957-960.

(28) Choi, S. Y.; Mamak, M.; von Freymann, G.; Chopra, N.; Ozin, G. A. Nano Lett. 2006, 6, 2456-2461.

(29) Zhang, J.-T.; Wang, L.; Lamont, D. N.; Velankar, S. S.; Asher, S. A. Angew. Chem. Int. Ed. 2012, 51, 6117-6120.

(30) Zhang, J.-T.; Cai, Z.; Kwak, D. H.; Liu, X.; Asher, S. A. Anal. Chem. 2014, 86, 9036-9041.

(31) Zhang, J.-T.; Smith, N.; Asher, S. A. Anal. Chem. 2012, 84, 6416-6420.

(32) Cai, Z.; Smith, N. L.; Zhang, J.-T.; Asher, S. A. Anal. Chem. 2015, 87, 5013-5025.

(33) Kanai, T.; Sawada, T.; Kitamura, K. Langmuir 2003, 19, 1984-1986.

(34) Flory, P. J. Principles of polymer chemistry; Cornell University Press, 1953.

(35) Anseth, K. S.; Bowman, C. N.; Brannon-Peppas, L. Biomaterials 1996, 17, 1647-1657.

(36) Ken-ichiro, N.; Katsuhiko, T.; Shinji, M. Japanese Journal of Applied Physics 2005, 44, 8186.

(37) Hassan, C. M.; Peppas, N. A. In Biopolymers· PVA Hydrogels, Anionic Polymerisation Nanocomposites; Springer, 2000, pp 37-65.

(38) Stauffer, S. R.; Peppast, N. A. Polymer 1992, 33, 3932-3936.

(39) Ricciardi, R.; Auriemma, F.; De Rosa, C.; Lauprêtre, F. Macromolecules 2004, 37, 1921-1927.

(40) Elliott, J. E.; Macdonald, M.; Nie, J.; Bowman, C. N. Polymer 2004, 45, 1503-1510.

(41) Chung, J. Y.; Nolte, A. J.; Stafford, C. M. Adv. Mater. 2011, 23, 349-368.

(42) Reese, C. E.; Asher, S. A. J. Colloid Interface Sci. 2002, 248, 41-46.

3.0 Increased Volume Responsiveness of Macroporous Hydrogels

This work was previously published as Coukouma, A. E.; Asher, S. A. *Sensors and Actuators B: Chemical* **2018**

Author Contributions: A.E.C. performed all experimental design and work. The manuscript was prepared by A.E.C. with assistance from SAA

Hydrogels can be fabricated into smart materials whose volumes predictably depend on their chemical environment. These smart hydrogel materials can be utilized in applications such as sensors, actuators, and for drug delivery materials, for example. The volume response of these hydrogels is well-known to be limited by their crosslink density. Thus, the responsiveness of hydrogels can be increased by decreasing the hydrogel's crosslink density. Unfortunately, this also decreases the hydrogel strength.

The hydrogel "effective crosslink density" can be decreased by fabricating macroporous hydrogels where voids are incorporated into the hydrogel. In the work here we demonstrate that this approach increases the volume responsiveness of hydrogels. We fabricated pH responsive macroporous hydrogels by copolymerizing acrylic acid with acrylamide. We compared the pH response of these hydrogels to that of macroporous hydrogels with small water bubbles embedded by vortexing the polymerizing hydrogel in air, or by preparing an inverse opal hydrogel. We then filled these embedded air bubbles with water. The pH responsiveness of these macroporous hydrogels are significantly increased compared to those of non-macroporous hydrogels of similar composition. We find that these macroporous hydrogels appear to be more mechanically robust than are similarly responsive hydrogels without voids.

3.1 Introduction

Hydrogels are crosslinked polymer materials that contain significant amounts of a water mobile phase. Hydrogels can be fabricated into highly responsive "smart" materials that respond to changes in their chemical or physical environments. Hydrogels imbibe or expel water in response to changes in their chemical environment, by undergoing a Volume Phase Transition (VPT)[32]. Hydrogels have been utilized in sensors [2,5,17,24,41-43], actuators [44,45], and other smart material applications [10-12]. There is great interest in developing hydrogel sensors to sensitively and selectively detect changes in their chemical and physical environments such as pH [3,15,20,38] and heavy metal concentrations [7,17,46], temperature [21,47,48], and, most recently, concentrations of microbes [43].

Flory and Huggins[32]. demonstrated that hydrogel VPT result from osmotic pressures derived from the free energy of mixing, from counter ion concentration inhomogeneitiy free energies, and from the crosslinking elastic free energy

The magnitude of the hydrogel VPT is constrained by the hydrogel crosslink density. Obviously, we can increase the magnitude of the VPT by decreasing the hydrogel crosslink density. However, this will decrease the mechanical strength of the resulting hydrogel [42]. In the work here we attempt to decrease the "effective crosslinking density" by introducing voids into the hydrogels.

We formed two types of macroporous hydrogels by either incorporating lots of small air and water bubbles into a polymerizing hydrogel by vortexing the system, or by forming an inverse opal hydrogel [15,46,49,50]. Inverse opal hydrogels are fabricated by polymerizing a hydrogel polymer monomer solution around close packed monodisperse particles. Similar inverse opal hydrogels have been utilized in sensing [15,46,50] and cell growth [49,51] applications.

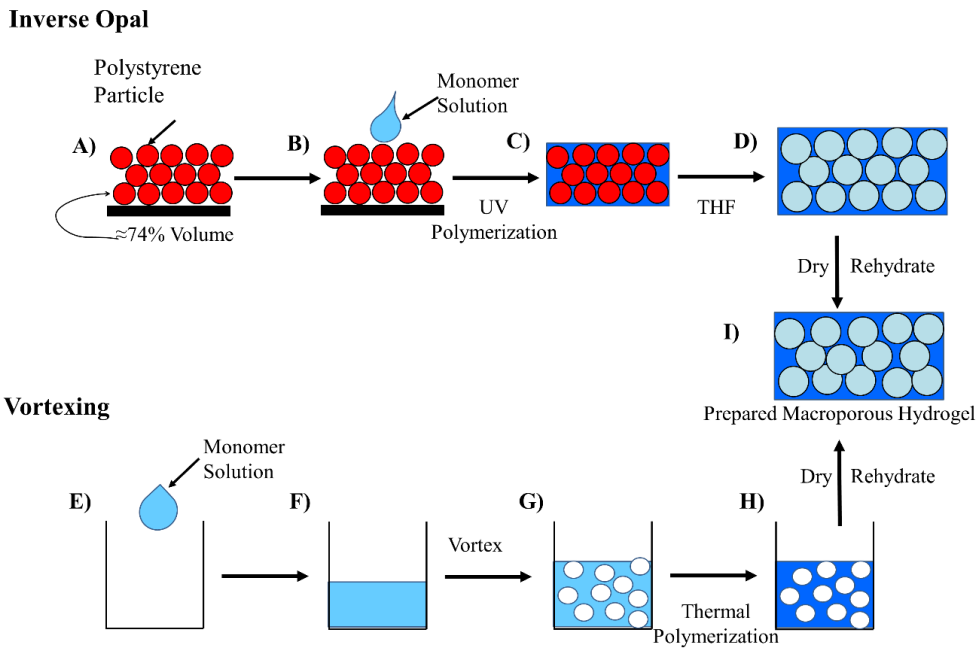

Figure 3.1- Fabrication methods utilized to produce macroporous hydrogels. A-D. An inverse opal method utilizes polstrene nanoparticles to incorporate macropores. E-H. Alternatively, a vortexing method utilizes agitation to incorporate air bubble macropores. Macroporous hydrogels fabricated via both methods were dried and rehydrated, filling the air bubbles with water before the swelling ratio measurements.

3.2 Materials and Methods

3.2.1 **Materials**

Igracure 2959, Acrylamide (Am), Azobisisobutyronitrile (AIBN), Pluronic F-127 (PF-127), Sodium Phosphate Monobasic, Sodium Phosphate Dibasic, Ammonium Persulfate (AMPS), N,N,N',N'-Tetramethylethane-1,2-diamine (TEMED) , Tetrahydrofuran (THF) and N-N`-Methylenebisacrylamide (BIS) were acquired from Sigma Aldrich (≥95% purity) and used as received. Acrylic acid (AA) was acquired from Sigma Aldrich and purified through distillation.

Glacial acetic acid and ethylene glycol was supplied by Fisher and used as received. Sodium acetate was acquired from EM Science and used as received. Water was purified by a Barnstead nanopure system.

3.2.2 **Fabrication of Inverse Opal Hydrogels**

Fig. 3.1 shows the fabrication of inverse opal macroporous hydrogels. A close packed array of monodisperse 940 nm polystyrene particles was formed by evaporating 2 mL of a ~15% (w/w) dispersion of these particles on a glass slide (Figure 3.1A). Igracure 2495 was used to initiate the polymerization of 150 μL of a solution of 10% (w/w) AAm, 1% (w/w) AA, and 1% (w/w) BIS in a 50% ethylene glycol -50%water solution. This polymerization solution was layered onto the previously prepared dried close packed polystyrene particles (Figure 3.1B). A glass slide was placed on top of the solution for 30 min to allow the polymerization solution to fill the polystyrene particles interstitial spaces. The system was then exposed to UV light from two Blak Ray 365 nm mercury lamps for 15 min to polymerize the opal hydrogel (Figure 3.1C). The opal hydrogel was then peeled from the glass slides and soaked in THF for 12 hrs to dissolve the polystyrene particles (Figure 3.1C to D). The resulting inverse opal hydrogel was stored in pH ~3 sodium acetate buffer.

3.2.3 **Fabrication of Vortexed Hydrogels**

Vortexed hydrogels were prepared by deoxygenating 6 mL of a 10% (w/w) AAm, 1%(w/w) AA, 1% (w/w) BIS in a 50% ethylene glycol - 50% water solution by bubbling with N_2 gas for 30 min (Figure 3.1E). 400 μL of a 20% (w/w) solution of PF-127 in water was injected into this deoxygenated solution and gently mixed. To initiate polymerization 100 μL each of 10%

(w/w) TEMED in water, and 10% (w/w) AMPS in water were injected into the vial (Figure 3.1F). The monomer solution was then agitated by vortexing to incorporate gas bubbles during the polymerization (Figure 3.1 G to H). After polymerization (~ 3-5 min), the macroporous hydrogel was removed from the vial and stored in pH ~3 sodium acetate buffer. Non-macroporous samples were similarly fabricated, but without vortexing.

3.2.4 **Electron Microscopy of Hydrogels**

The hydrogels were characterized by Scanning Electron Microscopy (JEOL JSM-6390LV). Samples were dried in air at room temperature and were then sputter coated with a thin layer of Au.

3.2.5 **Measurement of pH Volume Response**

The pH volume responses of the macroporous hydrogels were monitored by swelling ratio measurements. Hydrogel samples were prepared for swelling ratio measurements by washing with water over 24 hrs to remove residual ethylene glycol and THF. The hydrogel samples were then dried in air at 75°C for 24 hrs, after which their dry weight was measured. The samples were then placed in sodium acetate buffers (pH 3.5-6) or sodium phosphate buffers pH (6-7.5) for 24 hrs (Figure 3.1 I). The ionic strength of the buffers was maintained at 0.01 M to avoid volume alterations due to changes in ionic strength. The hydrogels in buffer were subjected to vacuum for 30-60 sec. to assure that all voids were filled with buffer.

The wet, swollen, hydrogel weights were measured by removing the samples from the buffer and gently patting their exterior with an absorbent kimwipe before weighing the samples.

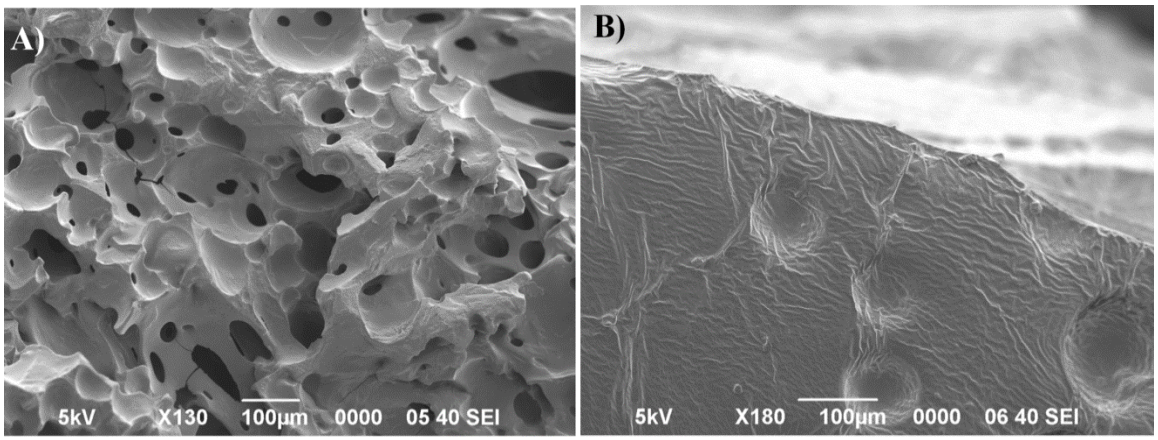

Figure 3.2- SEM micrographs. A. Hydrogel fabricated using the vortexing method shows large pores of 10-100 µm in diameter. B. A non-macroporous hydrogel shows no pores

This process was replicated several times and the results averaged. The swelling ratio, Q is defined as.

Equation 3.1

$$\boldsymbol{Q = (Weight\ Wet - Weight\ Dry)/Weight\ Dry}$$

3.3 Results and Discussion

3.3.1 Structure and Morphology of Vortexed Hydrogels

The morphology of the macroporous hydrogels fabricated by vortexing were compared to those of non-macroporous hydrogels by SEM (Figure 3.2). The SEM image of the vortexed macroporous hydrogel shows the presence of numerous large pores between 10-100 µm in diameter, (Figure 3.2A). This contrasts to the non-macroporous hydrogels that do not show pores (Figure 3.2B). The inverse opal hydrogels did not show clear SEM images, presumably because of their low polymer hydrogel volume fractions which caused them to collapse on drying.

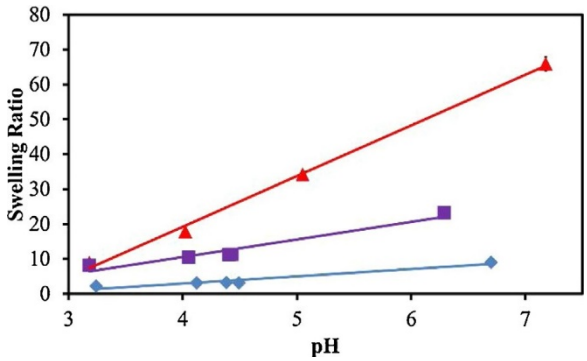

Figure 3.3- Comparison of pH dependence of the swelling ratio of macroporous hydrogels compared to a non-macroporous hydrogel. Error bars indicate one standard deviation.

3.3.2 **pH Volume Phase Transitions of Macroporous Hydrogels**

We fabricated pH responsive hydrogels by copolymerizing acrylic acid which has a pKa of ~4.7[3]. At elevated pH values the hydrogel carboxyl groups deprotonate attaching charges to the hydrogel network. These charges localize counterions around them that generate osmotic pressures that swell the hydrogel.

According to Flory-Huggins theory, the osmotic pressure induced by the deprotonation of the carboxyl group is counterbalanced by the osmotic pressure from the crosslinked hydrogel network [32]. The crosslinked hydrogel network osmotic pressure is dominated by the polymer chain crosslinks. However, the introduction of voids in the hydrogel network affects the hydrogel elasticity and its mechanical properties [52]. The voids decrease the contribution of the elastic free energy to the osmotic pressure due the decrease in the hydrogel polymer network volume fraction. This decrease in the elastic free energy contributions should increase the magnitude of the hydrogel VPT.

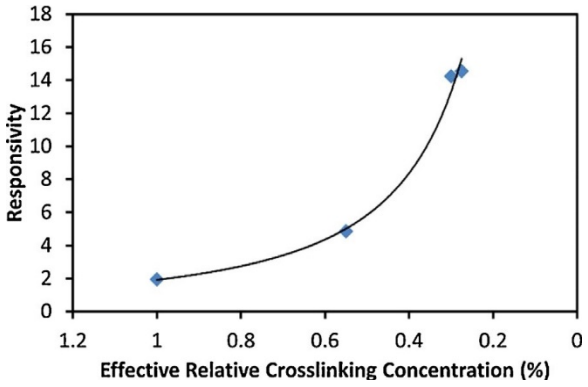

Figure 3.4- Hydrogel responsivity dependence on Effective Relative Crosslinking Con- centration (ERC). The data fit the relationship Responsivity ≈ 2*ERC$^{-1.5}$.

Thus, macroporous hydrogels are expected to have an increased VPT pH response compared to that of non-macroporous hydrogels. To confirm this expectation, we compared the pH dependence of the swelling ratio, Q of macroporous to non-macroporous, hydrogels (Figure 3.3), where Q, was calculated as shown in Eq 3.1.

Between pH 3.2 to 4.1 the non-macroporous hydrogel responsivity, ($\Delta Q/\Delta pH$) is 0.92±0.08. A ~3-fold larger responsivity occurs for the macroporous vortexed hydrogel (2.6±0.2). The responsivity is increased 10-fold compared to the, non-macroporous hydrogel for the inverse opal hydrogel (9.9±0.4). A vortexed hydrogel in the absence of acrylic acid shows no significant volume response over this same pH range.

We examined the dependence of hydrogel pH responsivity on the effective relative crosslinker concentration (Figure 3.4). We expect that effective relative crosslinker concentration will scale as the product of the crosslinker concentration (C_C) added, and polymer volume fraction, as decreased by the incorporated voids: ERC=C_c $(1 - f)$, where f is the void volume fraction; the hydrogel volume fraction = 1 for the non-macroporous hydrogels.

The macroporous hydrogel volume fraction was determined from the measured hydrogel density. The hydrogel densities were determined from the weights and volumes of the hydrogel

samples. The hydrogel density is the volume fraction weighted sum of the water equilibrated hydrogel density and the water filled void density, assumed to be that of water, $\rho_{MH} = \rho_w f + \rho_H (1-f)$, where ρ_{MH} is the macroporous hydrogel density, ρ_w is the density of the hydrogel water bubbles and ρ_H is the density of the non-macroporous pure hydrogel.

We prepared both a vortexed and an inverse opal macroporous hydrogel. From their measured densities we calculated that the vortexed hydrogel volume fraction, to be 0.55, while the inverse opal hydrogel volume fraction was 0.30. A perfect close packed inverse opal hydrogel would have volume fraction of 0.26. Our hydrogel volume fractions were generally larger, due to a lack of close packing. The hydrogel pH responsivity, as shown in Figure 4, is approximately inversely proportional to the ERC. This is expected due to the expected non-linear inverse relationship between the number of crosslinks and the hydrogel swelling ratio [5,32]

We prepared hydrogels with different ERC by varying the BIS crosslinker concentrations between 0.5 and 1 % for vortexed and inverse opal hydrogels. We found that we could prepare an *inverse opal hydrogel* with an estimated ERC ~0.3 % that shows a responsivity of ~14.3 by using a 1% BIS crosslinkier concentration and a hydrogel volume fraction of 0.3. Alternatively, we prepared a vortexed hydrogel with the same responsivity of ~14.3 by using 0.5% BIS and a hydrogel volume fraction of 0.45. Interestingly, the vortexed hydrogel with 0.5% BIS appears to have significantly lower mechanical strengths; the hydrogel broke into multiple pieces after 3 swelling ratio measurements. In contrast, the inverse opal hydrogel with 1 % BIS appears more mechanically robust; it did not fall apart after 3 measurement cycles.

This increased mechanical robustness presumably results from a decreased hydrogel brittleness due to the increase numbers of hydrogel voids which decreases the ability of fractures to successfully propagate [53,54]. For example, voids in foam-like structures interfere with fracture

propagation in metallic foams [55]. Thus, we conclude that increasing the void volumes in hydrogels should decrease fracture propagation, which should increase their mechanical strength.

3.4 Conclusion

We demonstrated an increased magnitude of VPT of macroporous hydrogels compared to those of non-macroporous hydrogels. We conclude that the incorporation of voids into the hydrogel network decreases the impact of the hydrogel crosslinking network elastic free energy constraints, which enables an increased hydrogel response. An increased magnitude of the VPT enables the fabrication of more responsive chemical sensors which enable lower limits of detection. We also demonstrated novel and simple vortexing and inverse opal fabrication methods that enable easy fabrication of macroporous hydrogels. These macroporous hydrogels appear more mechanically robust than their non-macroporous counterparts.

3.5 Acknowledgements

We thank Dr. Sachin Velankar for discussions about the mechanical properties of hydrogel materials. We would like to acknowledge the Defense Threat Reduction Agency (DTRA) for supporting this work (Grant No. HDTRA 1-15-1-0038)

3.6 References

(1) Lee, M.-C.; Kabilan, S.; Hussain, A.; Yang, X.; Blyth, J.; Lowe, C. R. *Analytical chemistry* **2004**, *76*, 5748-5755.

(2) Holtz, J. H.; Asher, S. A. *Nature* **1997**, *389*, 829-832.

(3) Richter, A.; Paschew, G.; Klatt, S.; Lienig, J.; Arndt, K.-F.; Adler, H.-J. P. *Sensors* **2008**, *8*, 561-581.

(4) Zhang, J.-T.; Chao, X.; Liu, X.; Asher, S. A. *Chemical Communications* **2013**, *49*, 6337-6339.

(5) Goponenko, A. V.; Asher, S. A. *Journal of the American Chemical Society* **2005**, *127*, 10753-10759.

(6) Reese, C. E.; Baltusavich, M. E.; Keim, J. P.; Asher, S. A. *Analytical chemistry* **2001**, *73*, 5038-5042.

(7) Asher, S. A.; Peteu, S. F.; Reese, C. E.; Lin, M.; Finegold, D. *Analytical and bioanalytical chemistry* **2002**, *373*, 632-638.

(8) DeRossi, D.; Kajiwara, K.; Osada, Y.; Yamauchi, A. *Fundamentals and Biomedical Applications, Plenum Press, New York* **1991**.

(9) Osada, Y.; Okuzaki, H.; Hori, H. *Nature* **1992**, *355*, 242-244.

(10) Hoffman, A. S. *Advanced drug delivery reviews* **2012**, *64*, 18-23.

(11) Jeong, B.; Kim, S. W.; Bae, Y. H. *Advanced drug delivery reviews* **2002**, *54*, 37-51.

(12) Qiu, Y.; Park, K. *Advanced drug delivery reviews* **2012**, *64*, 49-60.

(13) Marshall, A. J.; Blyth, J.; Davidson, C. A.; Lowe, C. R. *Analytical chemistry* **2003**, *75*, 4423-4431.

(14) Sharma, A. C.; Jana, T.; Kesavamoorthy, R.; Shi, L.; Virji, M. A.; Finegold, D. N.; Asher, S. A. *Journal of the American Chemical Society* **2004**, *126*, 2971-2977.

(15) Lee, Y. J.; Braun, P. V. *Advanced Materials* **2003**, *15*, 563-566.

(16) Muscatello, M. M. W.; Asher, S. A. *Advanced functional materials* **2008**, *1186*, 18-18.

(17) Asher, S. A.; Sharma, A. C.; Goponenko, A. V.; Ward, M. M. *Analytical chemistry* **2003**, *75*, 1676-1683.

(18) Smith, N. L.; Hong, Z.; Asher, S. A. *Analyst* **2014**, *139*, 6379-6386.

(19) Ward Muscatello, M. M.; Stunja, L. E.; Asher, S. A. *Analytical chemistry* **2009**, *81*, 4978-4986.

(20) Gehrke, S. H.; Cussler, E. L. *Chemical Engineering Science* **1989**, *44*, 559-566.

(21) Otake, K.; Inomata, H.; Konno, M.; Saito, S. *Macromolecules* **1990**, *23*, 283-289.

(22) Asher, S. A.; Kimble, K. W.; Walker, J. P. *Chem. Mater.* **2008**, *20*, 7501-7509.

(23) Cai, Z.; Zhang, J.-T.; Xue, F.; Hong, Z.; Punihaole, D.; Asher, S. A. *Analytical Chemistry* **2014**, *86*, 4840-4847.

(24) Zhang, J.-T.; Wang, L.; Luo, J.; Tikhonov, A.; Kornienko, N.; Asher, S. A. *Journal of the American Chemical Society* **2011**, *133*, 9152-9155.

(25) Kang, Y.; Walish, J. J.; Gorishnyy, T.; Thomas, E. L. *Nat Mater* **2007**, *6*, 957-960.

(26) Choi, S. Y.; Mamak, M.; von Freymann, G.; Chopra, N.; Ozin, G. A. *Nano Letters* **2006**, *6*, 2456-2461.

(27) Zhang, J.-T.; Wang, L.; Lamont, D. N.; Velankar, S. S.; Asher, S. A. *Angewandte Chemie International Edition* **2012**, *51*, 6117-6120.

(28) Zhang, J.-T.; Cai, Z.; Kwak, D. H.; Liu, X.; Asher, S. A. *Analytical chemistry* **2014**, *86*, 9036-9041.

(29) Zhang, J.-T.; Smith, N.; Asher, S. A. *Analytical chemistry* **2012**, *84*, 6416-6420.

(30) Cai, Z.; Smith, N. L.; Zhang, J.-T.; Asher, S. A. *Analytical Chemistry* **2015**, *87*, 5013-5025.

(31) Kanai, T.; Sawada, T.; Kitamura, K. *Langmuir* **2003**, *19*, 1984-1986.

(32) Flory, P. J. *Principles of polymer chemistry*; Cornell University Press, 1953.

(33) Anseth, K. S.; Bowman, C. N.; Brannon-Peppas, L. *Biomaterials* **1996**, *17*, 1647-1657.

(34) Ken-ichiro, N.; Katsuhiko, T.; Shinji, M. *Japanese Journal of Applied Physics* **2005**, *44*, 8186.

(35) Hassan, C. M.; Peppas, N. A. In *Biopolymers· PVA Hydrogels, Anionic Polymerisation Nanocomposites*; Springer, 2000, pp 37-65.

(36) Stauffer, S. R.; Peppast, N. A. *Polymer* **1992**, *33*, 3932-3936.

(37) Ricciardi, R.; Auriemma, F.; De Rosa, C.; Lauprêtre, F. *Macromolecules* **2004**, *37*, 1921-1927.

(38) Elliott, J. E.; Macdonald, M.; Nie, J.; Bowman, C. N. *Polymer* **2004**, *45*, 1503-1510.

(39) Chung, J. Y.; Nolte, A. J.; Stafford, C. M. *Advanced materials* **2011**, *23*, 349-368.

(40) Reese, C. E.; Asher, S. A. *Journal of Colloid and Interface Science* **2002**, *248*, 41-46.

(41) Cai, Z.; Luck, L. A.; Punihaole, D.; Madura, J. D.; Asher, S. A. *Chemical Science* **2016**, *7*, 4557-4562.

(42) Coukouma, A. E.; Smith, N. L.; Asher, S. A. *Analyst* **2015**, *140*, 6517-6521.

(43) Cai, Z.; Kwak, D. H.; Punihaole, D.; Hong, Z.; Velankar, S. S.; Liu, X.; Asher, S. A. *Angewandte Chemie International Edition* **2015**, *54*, 13036-13040.

(44) Gerlach, G.; Arndt, K.-F. *Hydrogel sensors and actuators: engineering and technology*; Springer Science & Business Media, 2009; Vol. 6.

(45) Liu, Z.; Calvert, P. *Advanced Materials* **2000**, *12*, 288-291.

(46) Zhang, M.-L.; Jin, F.; Zheng, M.-L.; Duan, X.-M. *RSC Advances* **2014**, *4*, 20567-20572.

(47) Snowden, M. J.; Chowdhry, B. Z.; Vincent, B.; Morris, G. E. *J. Chem. Soc., Faraday Trans.* **1996**, *92*, 5013-5016.

(48) Kanazawa, H.; Yamamoto, K.; Matsushima, Y.; Takai, N.; Kikuchi, A.; Sakurai, Y.; Okano, T. *Analytical chemistry* **1996**, *68*, 100-105.

(49) Stachowiak, A. N.; Irvine, D. J. *Journal of Biomedical Materials Research Part A* **2008**, *85*, 815-828.

(50) Lee, Y.-J.; Pruzinsky, S. A.; Braun, P. V. *Langmuir* **2004**, *20*, 3096-3106.

(51) Ford, M. C.; Bertram, J. P.; Hynes, S. R.; Michaud, M.; Li, Q.; Young, M.; Segal, S. S.; Madri, J. A.; Lavik, E. B. *Proceedings of the National Academy of Sciences of the United States of America* **2006**, *103*, 2512-2517.

(52) Nakajima, T.; Furukawa, H.; Tanaka, Y.; Kurokawa, T.; Gong, J. P. *Journal of Polymer Science Part B: Polymer Physics* **2011**, *49*, 1246-1254.

(53) Weng, L.; Gouldstone, A.; Wu, Y.; Chen, W. *Biomaterials* **2008**, *29*, 2153-2163.

(54) Sun, J.-Y.; Zhao, X.; Illeperuma, W. R.; Chaudhuri, O.; Oh, K. H.; Mooney, D. J.; Vlassak, J. J.; Suo, Z. *Nature* **2012**, *489*, 133.

(55) Sugimura, Y.; Meyer, J.; He, M.; Bart-Smith, H.; Grenstedt, J.; Evans, A. *Acta materialia* **1997**, *45*, 5245-5259.

4.0 Debye Ring Diffraction Elucidation of 2D Photonic Crystal Self-Assembly and Ordering at the Air-Water Interface

This chapter was previously published as Smith, N. L.; Coukouma, A.; Dubnik, S.; Asher, S. A., *Physical Chemistry ChemicalPhysics* 2017, *19* (47), 31813-31822

Author Contributions: A.E.C. and N.L.S. fabricated samples,collected data, and analyzed data. N.L.S. collected 2DPC SEM images. The MATLAB program that calculated the 2D pair correlation function from SEM images of the 2DPC was written and run by A.E.C. The manuscript was prepared by N.L.S with assistance from S.A.A.

We fabricate 2D Photonic Crystals (2DPC) by spreading a dispersion of charged colloidal particles (diameters= 409, 570, and 915 nm) onto the surface of electrolyte solutions using a needle tip flow method. When the interparticle electrostatic interaction potential is large, particles self-assemble into highly ordered hexagonal close packed (hcp) monolayers. Ordered 2DPC efficiently forward diffract monochromatic light to produce a Debye ring on a screen parallel to the 2DPC. The diameter of the Debye ring is inversely proportional to the 2DPC particle spacing, while the Debye ring brightness and thickness depends on the 2DPC ordering.

The Debye ring thickness increases as the 2DPC order decreases. The Debye ring ordering measurements of 2DPC attached to glass slides track measurements of the 2D pair correlation function order parameter calculated from SEM micrographs. The Debye ring method was used to investigate the 2DPC particle spacing, and ordering at the air-solution interface of NaCl solutions, and for 2DPC arrays attached to glass slides. Surprisingly, the 2DPC ordering does not monotonically decrease as the salt concentration increases. This is because of chloride ion adsorption onto the anionic particle surfaces. This adsorption increases the particle surface charge

and compensates for the decreased Debye length of the electric double layer when the NaCl concentration is below a critical value.

4.1 Introduction

2-Dimensional photonic crystals (2DPC) are two dimensional dielectric periodic materials that control the propagation of light.[1] 2DPC are commonly fabricated using colloidal nano- or mesoparticles with a significant dielectric constant difference from that of the surrounding media. When the particle diameter is on the same order as the wavelengths of light,the individual particles will Mie scatter the incident light. For a colloidal crystal like the a 2DPC,visible light is scattered from a periodic array of particles, causing interference of the scattered waves.[2-3] Constructive interference of the scattered waves from the periodic lattice results in Bragg diffraction, which is analogous to x-ray diffraction from ordered atomic and molecular crystal structures.[4-5] For 2D Bragg diffraction, white light is scattered by particles in a periodic monolayer such that each wavelength is diffracted at a particular angle.[6] The forward diffracted light through a 2DPC film diffracts as a rainbow. The Mie scattering cross sections are large. Thus, these 2DPC diffract nearly all incident light into the Debye ring.

These periodic, optical materials have numerous applications such as sensing,[7-9] waveguiding[10-12], superhydrophobic and antifogging coatings.[13-15] Further, these periodic materials are useful for fabricating SERS substrates[16], for Localized Surface Plasmon Resonance Spectroscopy substrates[17], and for particle lithography[18-20]. There is intense interest in the development of methods to fabricate large area, highly ordered 2DPC.[18, 21]

Nanoparticle 2D array self-assembly is the most commonly used technique to fabricate 2DPC. Alternatively, AFM nano-lithographic techniques offer a high level of precision for fabricating 2DPC structures with few defects.[22] Unfortunately, lithography is slow and limited to fabricating small areas. Self-assembly has the advantage of being less expensive than lithography; it can fabricate much larger areas in less time. Many methods have been developed to self-assemble nanoparticles into hexagonal close packed (hcp) ordered arrays, including the needle tip flow (NTF) method (which has recently been called micro-propulsive injection)[10, 23] , spin coating[24], the Langmuir-Blodgett technique[18,25,26], wet coating[27], floating[28,29], and evaporation induced self assembly.[30,31]

Each of the self-assembly methods constrain interparticle interactions such that a hexagonal close packed structure is the minimum free energy.[32] The interactions that determine particle ordering differ between the different self-assembly techniques. For example, solvent-substrate and particle-substrate interactions that impact ordering in evaporation induced self-assembly methods[16,33] do not significantly impact ordering for particles self-assembled at the air-water interface. The interparticle interactions are optimized for each different method to improve particle ordering to obtain large hcp crystal domains. Alternatively, post self-assembly methods to improve 2DPC order have also been investigated. Shinotsuka *et al*[18] utilized ultrasonic annealing, or repeated compression cycles after self-assembly at the air-water interface to increase the 2DPC order through Oswald ripening of the colloidal crystal domains.

In this work, we investigated the self-assembly of charged colloidal particles at the air-water interface using the needle tip flow method.[23,24] Our objective was to control the 2DPC ordering by decreasing the electrostatic repulsions between particles by the addition of NaCl to the

water subphase. We monitored the 2DPC particle spacing and ordering by using Debye ring diffraction of visible light.

4.2 Experimental

4.2.1 **Materials**

Sodium 4-Vinylbenzenesulfonate, Ammonium Persulfate, 2,2`-Azobis(2-Methylpropionitrile), 1-Propanol, and 2-Hydroxyethyl Methacrylate were acquired from Sigma Aldrich (≥90% purity) and used as received. Styrene was acquired from Sigma Aldrich and purified by column chromatography. Methanol (>99.8%) and Sodium Chloride (>99.5%) were acquired from Fischer Scientific and used as received.

4.2.2 **Polymerization and Characterization of Monodisperse Negatively Charged Polystyrene Nanoparticles**

Negatively charged PS nanoparticles with diameters of 915 nm were synthesized by dispersion polymerization using a procedure described by Zhang et al.[35] Negatively charged polystyrene nanoparticles with diameters of 570 nm and 409 nm were synthesized by emulsifier free emulsion polymerization using a procedure described by Reese et al.[36]

The weight percent of each PS particle dispersion was calculated by dividing the weightof dried particles by the original weight of the dispersion. The average particle diameter was determined by measuring the diameter of >150 particles in SEM micrographs using the National

Institute of Health program, ImageJ. SEM micrographs of 2DPC were obtained using a JEOL 6390LV Scanning Electron Microscope.

PS water dispersions were cleaned by centrifuging the particles into a pellet (10,000 RPM for 10 min) then redispersing them in nanopure water at least three times before use. The final volume of water added to the PS particle pellet was adjusted so that the final concentration is 15 wt% PS particles in water. The zeta-potentials of the PS particles in nanopure water, or in 0.001, 0.01, 0.1 or 1 M NaCl solutions were measured on a Brookhaven Zeta-PALS instrument.

4.2.3 **2DPC Fabrication Using Needle Tip Flow Method**

We fabricated the 2DPC by self-assembling charged colloidal nanoparticles on a water surface using our Needle Tip Flow (NTF) method[23] as shown in Figure 4.1. The 15 wt% PS nanoparticle aqueous dispersion is mixed with propanol to lower the particle dispersion surface tension. The NTF flow method utilizes the Marangoni effect, which drives the PS particles to spread on the water surface due to surface tension gradients. The Marangoni flow guides the particles towards areas with higher surface tension, this directs particles towards the dish outer edge. Therefore, particles radially spread outwards from the needle tip to the edge of the water surface as shown in Figure 4.1, part 3. The video provided in Appendix A demonstrates that the particles initially spread to cover the outer water surface at the edge of the dish.

A 21-gauge needle is attached to a 1 mL plastic syringe containing ~0.6 mL of a 3:1 PS particle dispersion: propanol mixture. A 9 cm diameter, 6 cm deep glass crystallization dish is filled with nanopure water, or aqueous salt solutions containing 0.001, 0.01, 0.1 or 1 M NaCl. The vertically oriented needle pierces the water surface such that half of the needle tip beveled orifice bisects the water meniscus. The particle dispersion flow rate is controlled by the pressure applied

to the 1 mL syringe plunger. The particle dispersion that is layered on the water surface spreads onto the water surface until the surface becomes completely covered with particles. Once the water surface is filled with the particle monolayer, the particle dispersion will begin to disperse into the bulk water instead of spreading on the surface. The circular boundary of the self-assembled 2DPC along the outer edge of the water surface is easily observed as shown in Figure 2.1, part 3. The visually evident 2DPC boundary is monitored during particle depositionto determine the point when the water surface is filled with particles. The particle dispersion flowing onto the water surface is then stopped.

Optical microscopy was used to obtain images of a 2DPC made from 915 nm particles at the air-water interface. A Leica TCS SP5 confocal laser scanning microscope with a Leica HCX-PL APO 40x/0.85 objective was used to collect images in transmission mode, and the scanrate was 100 Hz.

The 2DPC is lifted from the water surface with a glass microscope slide (Figure 2.1, part 4). The slide is vertically inserted into the water. The plane of the slide is then rotated to be parallel with the water surface while the slide lifts the self-assembled 2DPC from the water surface. The slide is placed on a flat surface and allowed to dry at room temperature. After drying, the 2DPC adheres to the microscope slide surface. 2DPC were fabricated using 409, 570,and 915nm diameter PS particles. The particles were self-assembled on nanopure water surfaces, and on aqueous salt solutions containing 0.001, 0.01, 0.1, and 1M NaCl. Ten replicate samples were fabricated for each set of particles and salt solutions.

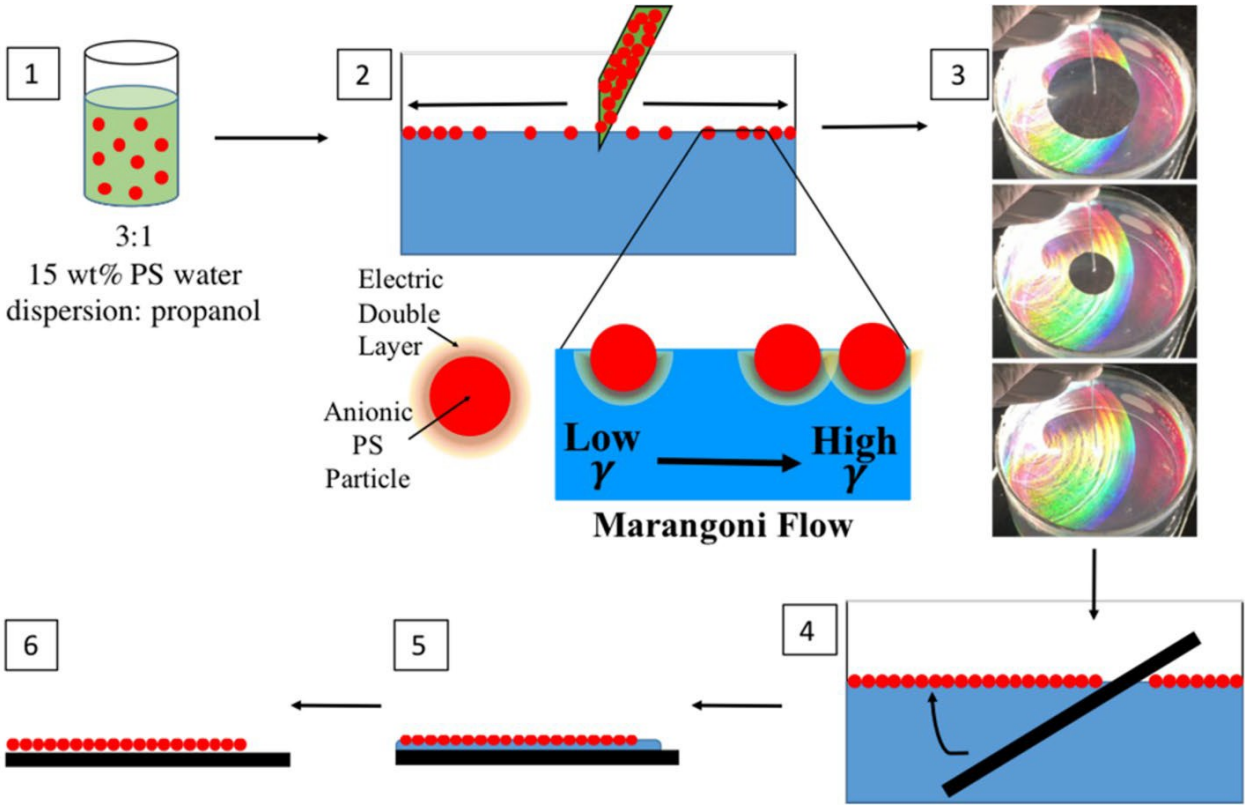

Figure 4.1- Schematic of needle tip flow 2DPC fabrication at the air-water interface. 1) Addition of propanol lowers the surface tension of the particle dispersion. 2) The dispersion is spread on the water surface througha needle tip at a constant rate. The surface tension gradient forces the particles to the outer edge of the water surface. 3) Appendix A contains a link to a video showing 2DPC self-assembly on the water surface. The boundary between the self-assembled 2DPC and the particle-free pure water surface is visually evident. The radius of this boundary decreases as more particles are spread onto the surface. 4) The 2DPC is lifted from the water surface by a microscope slide. 5) The wet slide with the lifted 2DPC is dried at room temperature. 6) After the water evaporation, the particles on the slide surface adhere to the microscope slide.

4.2.4 **2DPC Debye Ring Diffraction Measurements**

The ordered 2DPC efficiently forward diffract light. In the case of a perfectly ordered 2DPC monochromatic light will be diffracted onto a screen parallel to the 2DPC monolayer as a hexagonal array of spots. These six spots correspond to the six reciprocal lattice vectors of the 2D close packed hexagonal particle array.

If the self-assembled 2DPC consists of small crystallites that are rotationally disordered, the diffraction of normal incident monochromatic light will form a continuous ring, called the Debye ring, shown in Figure 4.2B. We measured the Debye ring diameter to calculate the 2DPC particle spacing. We can utilize the Debye ring thickness to monitor the 2DPC order, provided that the width of the Debye ring is limited by disorder and not by the laser beam spot size.

For example, Figure 4.2 A shows the diffraction geometry used for measuring the Debye ring with a 406 nm violet laser diode (Thor Labs, 2.2 mm diameter spot size). The normally incident monochromatic light is forward diffracted at an angle, θ onto a screen parallel to the 2DPC plane. The diameter of the Debye ring projected onto the screen depends on both the 2DPC particle spacing, a and the distance, h between the 2DPC and the screen.

The Debye rings were measured at five different locations on each 2DPC attached to the glass slide. The difference between the outer and inner Debye ring diameters are the widths of the

Equation 4.1

$$\boldsymbol{\theta = tan^{-1}\frac{d}{2h}}$$

Equation 4.2

$$\boldsymbol{sin\theta = \frac{2\lambda}{\sqrt{3}a}}$$

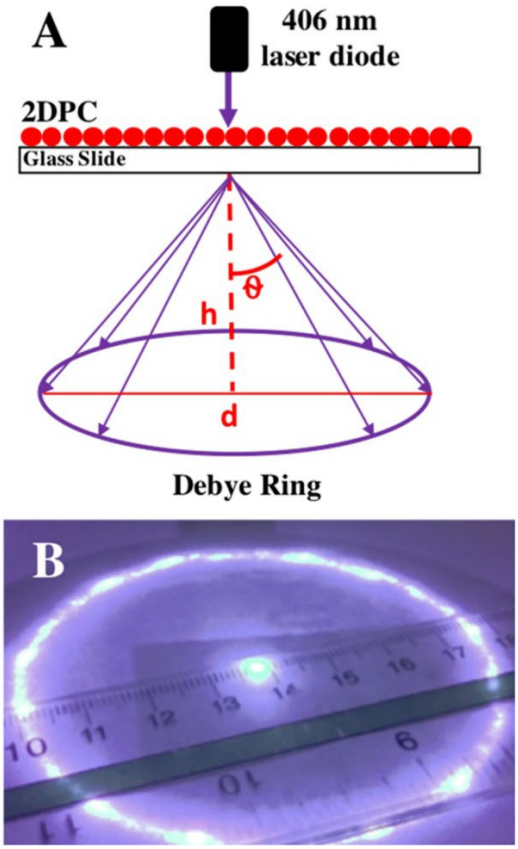

Figure 4.2- (A) Illustration showing the angles of diffraction for 406 nm light travelling through water, θ_w, and air, θ_a. The distance the light travels in each medium, h_w and h_a determines the final Debye ring diameter. (B) Photograph of the Debye ring.

Debye rings. The average of the inner and outer diameters, d, gives us the Debye ring diffraction angle, θ (Equation 4.1), and the particle spacing, a (Equation 4.2).[7, 37]

The Debye ring diffraction was also measured for a 915 nm 2DPC on the water surface. The measurements were repeated at least three times for the 2DPC on a nanopure water surface, and on 0.01 M, and 0.1 M NaCl solutions. The Debye rings were also measured for the 2DPC on the surface of the microscope slide directly after the 2DPC was lifted off the water surface.

As shown in Figure 4.3 the diffraction of the 2DPC lying on the water surface is shifted due to refraction of the light by the air-water interfaces. The Debye ring diameter of a 2DPC on the water surface will be smaller than that from an identical 2DPC on a glass slide.

The diffraction angle in air, θ_a can be calculated from Debye ring diffraction measurements of a 2DPC on a water surface using Equation 4.3, which details the impact of Snell's Law, $\theta_w=\sin^{-1}((n_a \sin\theta_a)/n_w)$. The thickness and refractive index of water and air layers are h_w, n_w, and h_a, n_a respectively.

Equation 4.3

$$\frac{d}{2} = h_w \tan\left(\sin^{-1}\left((n_a \sin\theta_a)/n_w\right)\right) + h_a \tan\theta_a$$

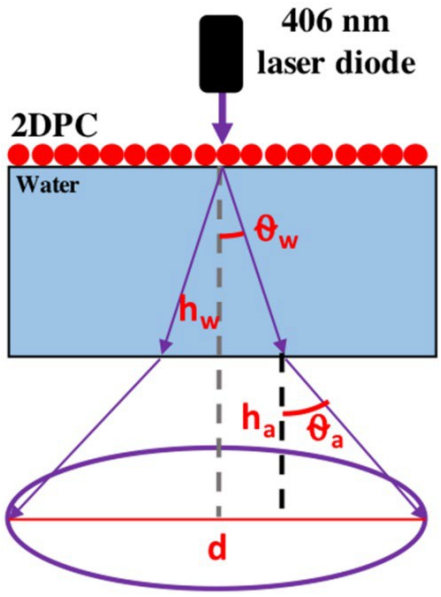

Figure 4.3- Cartoon showing the angles of diffraction for 406 nm light travelling through water, θw, and air, θa. The distance the light travels in each medium, hw and ha determines the final Debye ring diameter.

4.2.5 **2DPC Ordering Analysis**

We examined the ordering of three 2DPC samples for each set of experimental conditions. We sputter coated the 2DPC on glass slides with gold for 90 sec (30 mA current)using a PELCO SC-7 sputter coater. The gold coated 2DPC were imaged using a scanning electron microscope (JEOL 6390LV SEM). Five SEM micrographs were collected from different areas of each 2DPC sample. Representative SEM images for each particle diameter andsalt concentration are provided in Appendix A. These 2DPC images were used to calculate the 2D pair correlation function, g(r)

Equation 4.4

$$g(r) = \frac{1}{\langle p \rangle} \frac{dn(r,r+dr)}{da(r,r+dr)}$$

(Equation 4.4).[23,38,39] The pair correlation function calculatesthe number of particles (dn) within the area (da) of a ring having an inner diameter (r) and outer diameter (r+dr). g(r) was calculated for shell radii ranging from 0 to 14, where dr was $0.016R_0$. R_o is the particle radius.

A detailed description of our 2DPC ordering analysis and the MATLAB code written to calculate the 2D pair correlation function can be found in Appendix A. Briefly, the MATLAB circle finding algorithm, imfindcircles, was used to find the centers of the particles in each SEM micrograph. This function creates a matrix of the particle positions from which the pair correlation function can be calculated. A discrete Fast Fourier Transform (FFT) was then calculated for the function g(r)-1. The dimensionless order parameter (κ/κ_o) is calculated as the ratio of the FWHM of the FFT peak for a fabricated 2DPC, κ and the FWHM of the FFT peak for a perfect array, κ_o.[23] The average order parameter was calculated using data from at least 15 SEM micrographs for each experimental condition.

4.3 Results and Discussion

4.3.1 Needle Tip Flow Nanoparticle Self-Assembly at the Air-Water Interface

The Needle Tip Flow (NTF) method for self-assembling charged nanoparticles at the air-water interface produces highly ordered 2DPC, with large crystalline domains (~100 μm^2).[23, 34] The 2DPC can be fabricated on large area water surfaces (730 cm^2 for a single needle tip) in ~2 min using the NTF method (Figure 2.1). Gao et al[10] fabricated very large area (~1m^2) 2DPC using a micro-propulsive injection method, which is analogous to our NTF method. They were able to quickly fabricate very large areas of 2DPC at the air-water interface because the particle dispersion was spread on the water surface at multiple injection points using syringe pumps.

The NTF flow method, described in previous papers[10, 23, 34, 40, 41] utilizes Marangoni flow that spreads the PS particle dispersion on the water surface. The Marangoni flow results from surface tension gradients that generate surface fluid motion such that lower surface tension liquid regions are pulled towards regions of high surface tension. The 15 wt% PS nanoparticle aqueous dispersion contains propanol to lower its surface tension. The resulting Marangoni flow spreads the particle dispersion radially outwards from the needle tip to the edge of the water surface (Figure 4.1, part 3). As shown by the video in Appendix A the particles spread as a monolayer onto the surface until the entire water surface is covered.

The ordering of the self-assembled 2DPC depends on the rate of spreading and upon the detailed balance between attractive and repulsive particle interactions in the 2DPC film. Adding NaCl to the water subphase should decrease the electrostatic repulsions between these negatively charged particles.

This can be clearly shown by qualitatively viewing the 2DPC ordering in SEM micrographs as shown in Figure 4.4 1a-1c. 2DPC fabricated on higher concentration saltsolutions are clearly less ordered. We can quantitatively determine the 2DPC order by calculating the 2D pair correlation function, g(r), from these SEM micrographs.

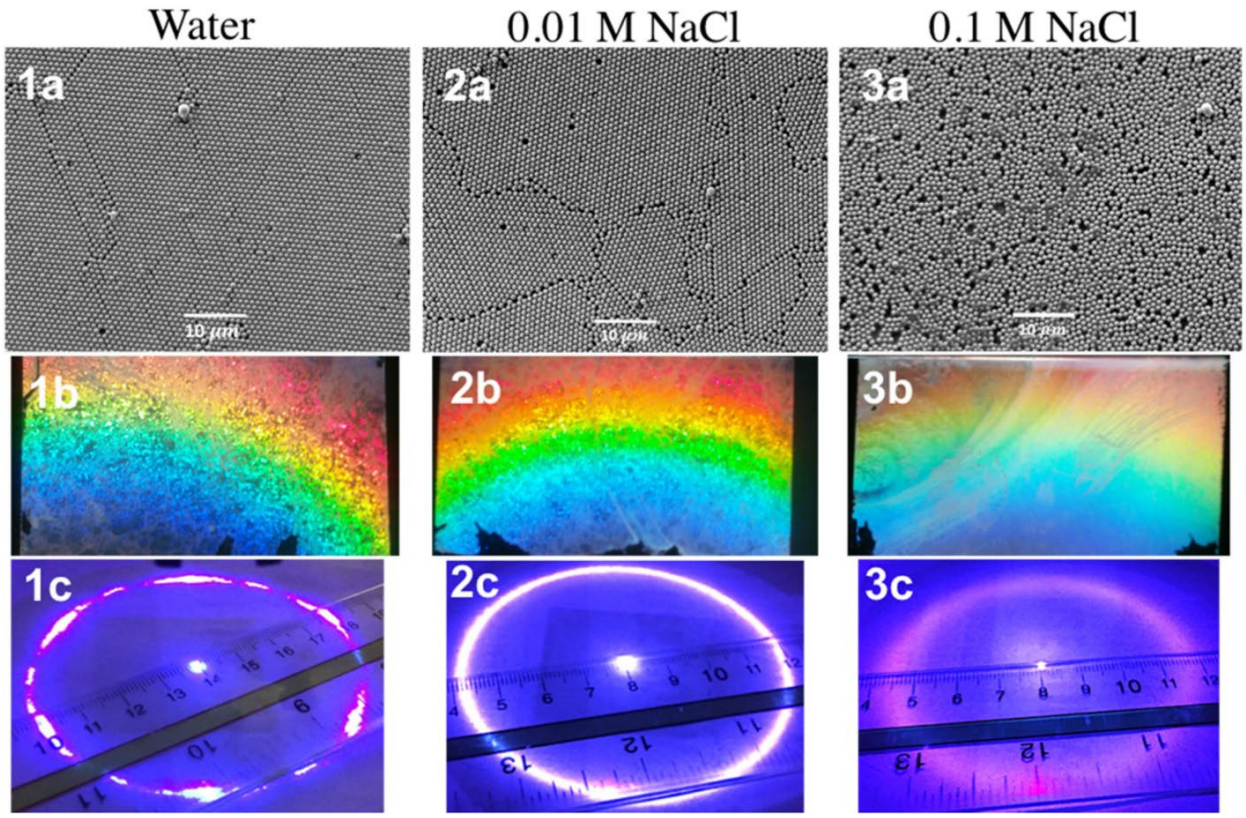

Figure 4.4- SEM micrographs (1a - 3a) of 2DPC of 915 nm PS particles prepared on solutions of increasing salt concentrations (pure water, 0.01 M NaCl and 0.1 M NaCl). (1b - 3b) Photographs of polychromatic light diffraction of 2DPC prepared on solutions of increasing salt concentrations. The diffraction polychromatic dispersion becomes more diffuse and less intense at larger salt concentrations. (1c - 3c) Photographs of Debye ring diffraction of normally incident 405 nm monochromatic light at increasing salt concentrations. Debye ring diffraction photograph of the 2DPC at 0.1 M NaCl was edited with regards to brightness/contrast and color balance so that the Debye ring could be easily be observed. This diffuse Debye ring is very hard to photograph due to the weak diffraction intensity.

Alternatively, we can quantitatively determine the 2DPC ordering without perturbing the sample by monitoring the Debye ring diffraction. Samples probed using the Debye ring diffraction method can be used in future experiments, unlike samples that are sputtered with goldprior to SEM.

4.3.2 **Estimating 2DPC Order from Debye Ring Measurements**

Most of the light incident on the 2DPC is diffracted into the Debye ring.[42] Unlike for the case of 3D Bragg diffraction, 2DPC planes forward diffract polychromatic light such that each wavelength diffracts at a discrete angle, θ as shown in Figure 2.4 1b-3b according to the 2D Bragg diffraction condition (Equation 4.5) for a 2DPC particle array with spacing, a.

Equation 4.5

$$\boldsymbol{\lambda = \frac{\sqrt{3}a}{2}(sin\,\alpha + sin\,\theta)}$$

For normally incident monochromatic light to the 2DPC plane, as shown in Figure 4.2, sinα = 0, and Equation 4.5 becomes Equation 4.2. Thus, the light is forward diffracted at an angle, θ that depends on the particle spacing, a, of the 2DPC array and the detailed 2DPC particle ordering. If a single 2DPC domain is irradiated, six spots are diffracted onto the screen (Figure 4.4 1c). These six spots correspond to the six reciprocal lattice vectors of the 2D hcp particle array. The fabricated 2DPC studied here often show a distribution of randomly oriented2D crystallites. Simultaneous irradiation of numerous crystalline 2DPC domains give rise to diffraction of a continuous Debye ring (Figure 4.4 2c-3c). The diameter of the Debye ring, determined by the diffraction angle θ, is inversely proportional to the 2DPC particle spacing, a.

Figure 4.4 illustrates the impact of 2DPC disorder on the diffraction. The decreasing 2DPC ordering of the particle array self-assembled on water, 0.01 M NaCl, and 0.1 M NaCl is evident in the SEM micrographs in Figure 4.4 a1-a3. As the 2DPC order decreases, the forwarddiffracted

white light intensity decreases (Figure 4.4 1b-3b), while the Debye ring thickness increases (Figure 4.4 1c-3c). The Debye ring width (w), can be used to monitor the 2DPC orderand particle spacing on the glass slides, as well as, at the air-water interface, without perturbingthe 2DPC.

The disordered 2DPC Debye rings will be broader than Debye rings from highly ordered 2DPC. The disordered 2DPC Debye ring broadening results from variations of particle spacing within the probed areas as shown in Figure 4.5. We are assuming the broadening contribution from the finite crystallite size is negligible compared to the laser beam spot size.

The hexagonal close packed (hcp) crystal shows the smallest plane spacing possible. This plane spacing will diffract light into the maximum diffraction angle for this particle diameter.

The Debye ring width of a perfectly ordered close packed 2DPC is only limited by the incident laser spot size. Less ordered crystals will diffract light into smaller diffraction angles. The sum of these contributions broadens the Debye ring. The outer Debye ring diameter does not change because it is fixed at the minimum particle spacing of the 2DPC lattice. In contrast the Debye ring inner diameter will shrink with increasing disorder as the average particle spacing increases. In general, the standard deviations of the Debye ring measurements increase as the 2DPC disorder increases, because the particle spacing is more heterogeneous.

The Debye ring width and calculated particle spacing change of the 2DPC adhered to glass slides are shown in Figure 4.6 and Figure 4.7, respectively for 570 nm and 915 nm diameter particle arrays fabricated on water and on NaCl solutions. The particle spacings were calculated using Equation 4.1 and Equation 4.2. The average of the inner and outer Debye ringdiameter was used to calculate the average particle spacing.

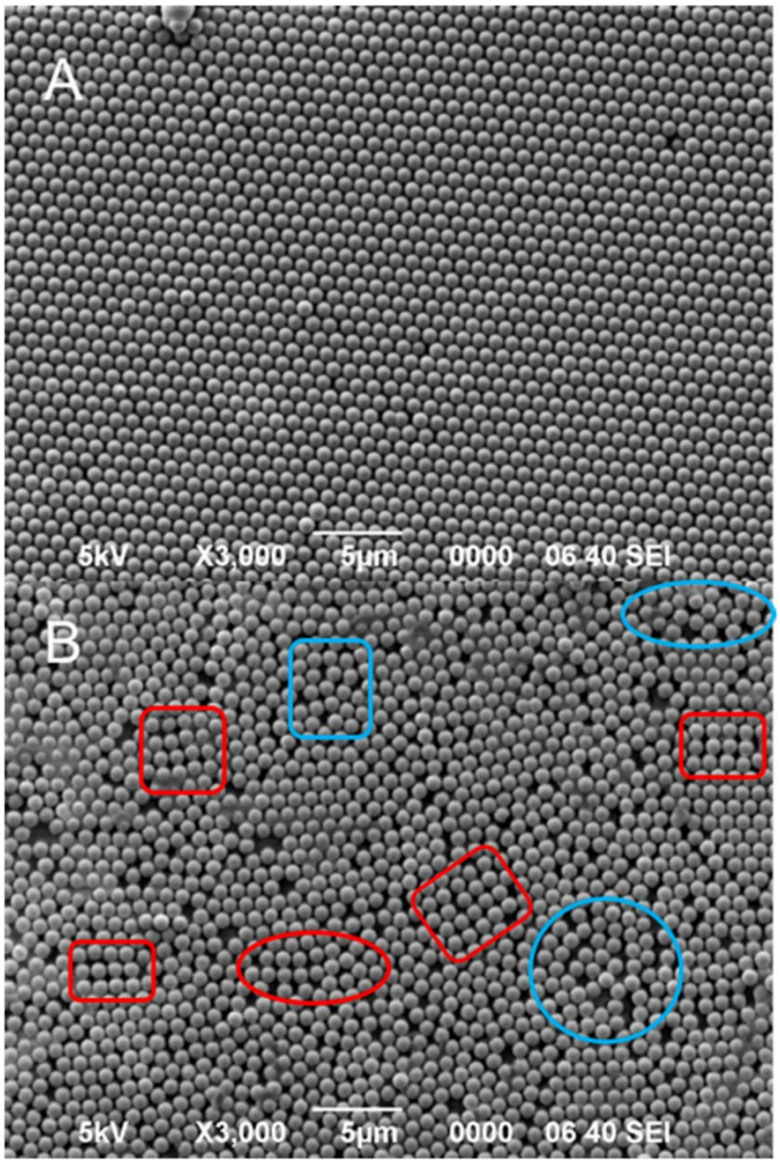

Figure 4.5- SEM images of 915 nm particle 2DPC (A) self-assembled on pure water and (B) on 0.1 M NaCl. (A)shows a well ordered 2DPC where the particle spacings show little variation. (B) shows a highly disordered 2DPC. The areas outlined in red are where the particle arrays assembled into a square lattice instead of a hexagonal lattice. Areas highlighted in blue show regions that are randomly oriented with little crystalline order.

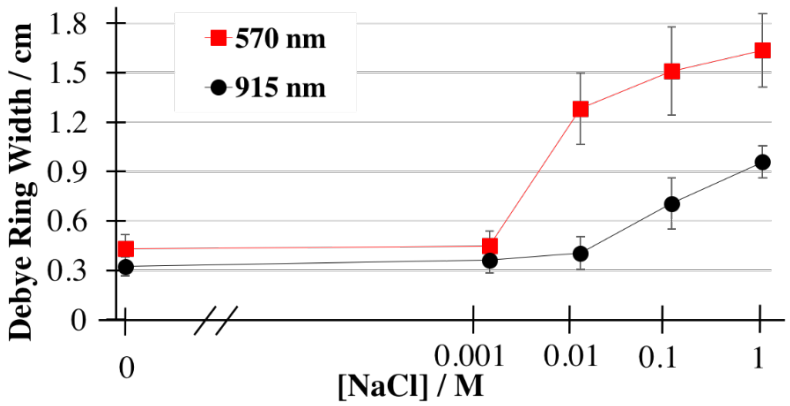

Figure 4.6- Dependence of Debye ring widths of 570 nm and 915 nm 2DPC as a function of the NaCl concentration.

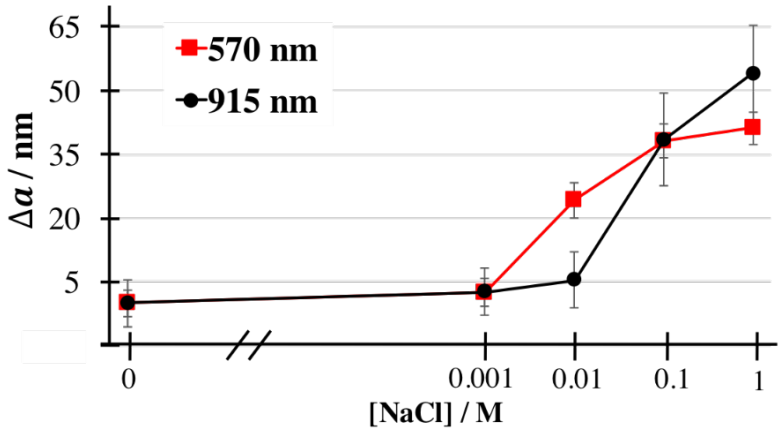

Figure 4.7- Particle spacing change, $\Delta a = a_{[NaCl]} - a_{water}$, for 570 and 915 nm 2DPC as a function of NaCl concentration. Particle Spacing is calculated from the Debye ring diameter measurements.

The average salt induced particle spacing change is the difference between the particle spacing of the 2DPC fabricated on a salt solution and the particle spacing of the 2DPC fabricated on pure water, $\Delta a = a_{[NaCl]} - a_{water}$. The increasing particle spacing change results from the decreased inner diameter of the Debye ring.

We expect the Debye ring width to monotonically increase with NaCl concentration. The 2DPC ordering is determined by the balance of attractive and repulsive interactions between particles at the air-water interface.[21] The addition of salt to the water subphase should monotonically decease the electrostatic repulsions between particles. This leads to "faster" assembly of particle arrays because the probability of particle adhesion between colliding particles increases, leading to disordered particle aggregates that can serve as nucleation sites forcrystal growth. The formation of randomly ordered particle clusters prevent 2D array annealing, where particles repel each other and arrange into a structure that minimizes the total energy of the system.

In contrast, our results indicate the 2DPC order is relatively unaffected by low concentrations of salt in the water subphase. The Debye ring width that is indicative of the 2DPC order, at low NaCl concentrations does not significantly differ from that of 2DPC fabricated in pure water. We find that there is a critical salt concentration, C* of NaCl required toinduce significant disorder. This critical salt concentration depends on the particle diameter, C*≈ 0.01 M NaCl for the 570 nm diameter particle 2DPC, while C*≈ 0.1 M NaCl for the 915 nmparticle 2DPC.

We examined the salt concentration dependence of the order parameter, κ/κ_o from our measured 2D pair correlation function, g(r) (Equation 4.4) from SEM micrographs of the same samples used for our salt concentration Debye ring width measurements. We also studied 409 nm diameter particles to examine the dependence of the 2DPC ordering on the particle diameter.The salt concentration dependence on the order parameter, κ/κ_o of the fabricated 2DPC, determined from the FFT of (g(r)-1), is shown in Figure 4.8. The threshold for disorder occurs when κ/κ_o >1.5.

The 2DPC order estimated from measurements of Debye ring width appears consistent with the detection of disorder from κ/κ_o calculated from SEM micrographs. The order parameter

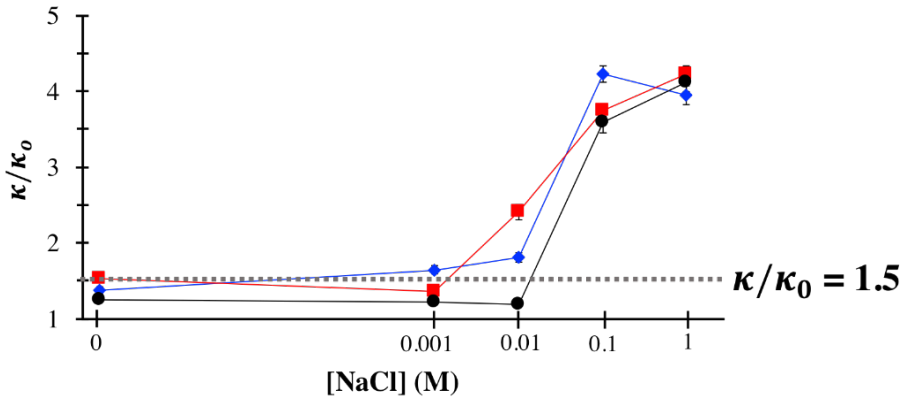

Figure 4.8- Dependence of the 2DPC order parameter, $\kappa/\kappa o$ on salt concentration for 409, 570 and 915 nm particle diameters. The horizontal line indicates $\kappa/\kappa o = 1.5$, above which disorder is present. Error bars indicate 95% confidence intervals.

results confirm that 2DPC order does not significantly decrease until the salt concentration exceeds the critical salt concentration. Analogous to the Debye ring width results,C* increases with an increasing particle diameter. The salt concentration at which κ/κ_o>1.5 is 0.001 M NaCl for 409 nm diameter particles, 0.01 M for 570 nm particles, and 0.1 M NaCl for915 nm particles. This dependence of the 2DPC ordering on the particle diameter and salt concentration is discussed below.

These results clearly indicate that the Debye ring width can be used to monitor the 2DPC order. This Debye ring width dependence is important because it enables non-destructive 2DPC order determinations of fragile systems such as the 2DPC at the air-water (or oil-water) interface.

4.3.3 **2DPC Ordering and Particle Spacing at the Air-Water Interface**

Three decades ago, Pieranski[43] showed that charged colloidal particles trapped at the air-water interface would self-assemble into ordered particle monolayers. Since then numerous additional methods were developed to fabricate close packed and non-close packed ordered particle monolayers, and to transfer them onto solid substrates.[3,21,44,45] Each new method developed

tuned the interparticle interactions to optimize the array ordering. Often, the ordering was monitored by determining the pair correlation function of images collected using Electron Microscopy[23,45,46] or AFM[3]. Any conclusions drawn from these SEM images must account for 2DPC disorder and particle spacing changes induced by transfer of the 2DPC from the air-water interface to the substrate and the impact of drying.

Optical microscopy has been used to investigate the particle array ordering at the air-water interface.[31, 43, 47] Confocal laser scanning microscopy is a powerful tool to investigate interfacial particle ordering, but the experiments require expensive optics and objectives.

Confocal microscopy measurements are also complicated by motion of the air-water interface. Incontrast, the Debye ring diffraction measurements allow us to easily probe the 2DPC ordering and particle spacing at the air-water interface using a laser pointer and a ruler or calliper.

The 2DPC particle spacing at the air-water interface is calculated from the Debye ring diameter using Equation 4.2 and Equation 4.3. We also compared the spacings of the 2DPC transferred from these interfaces to wet and dry microscope slides. The post-transfer measurements were taken prior to evaporation of the thin water film on the microscope slide surface, where the particles are still trapped at this air-water interface. The Debye ring was also measured after slide water evaporation, where the 2DPC adheres to the slide. Figure 4.9 shows the salt concentration dependence for the Debye ring width of the 915 nm diameter 2DPC at the air-water interface of pure water, 0.01 M NaCl, and 0.1 M NaCl. The calculated particle spacingsof these 2DPC samples are shown in Figure 4.10.

With the exception of the 0.1 M NaCl samples, the Debye ring widths are the same for the 2DPC at the air-water interface, on the wet slide, and when dried on the slide, indicating that the 2DPC transfer to the slide, and drying has little impact on the array ordering. The Debye ring width

of the 2DPC at the air-water interface of the 0.1 M NaCl samples may be slightly larger than the Debye ring width after transfer to the slide.

At 0.1 M NaCl concentrations, the particles spread from the needle tip increasingly disperse into the bulk water, increasing the turbidity of the water subphase. This turbidity partially obscures the diffuse Debye ring and makes it more difficult to measure its width. However, it is clear that the Debye ring widths of the 0.1 M NaCl samples are at least 2X greaterthan the widths of the 2DPC samples fabricated at lower salt concentrations.

The 2DPC particle spacing, a does not significantly change upon 2DPC transfer to the slide and the subsequent 2DPC drying. The 2DPC particle spacing at the air-water interface is very close to that found for the 2DPC on the wet and dried glass slides; these calculated particle spacings are roughly equal to the particle diameter when the 2DPC is well ordered. Thus, the NTF method produces self-assembled, highly ordered, hexagonal close packed (hcp) particle array monolayers at the air-water interface. These results are confirmed by confocal microscope imaging of the 915 nm 2DPC at the air-water interface, shown in Figure 4.11. These results aresignificant because it

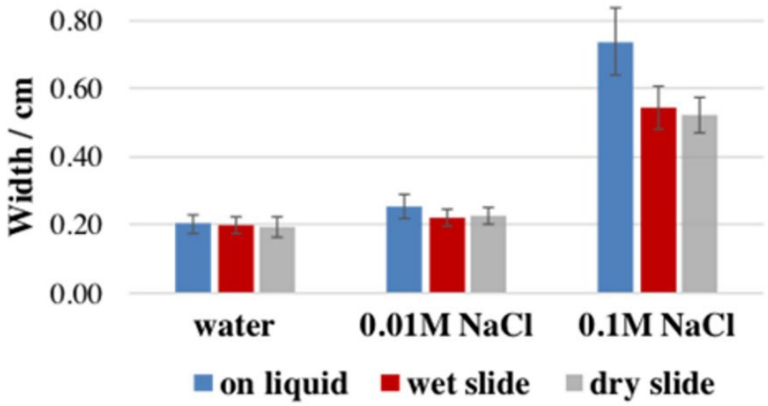

Figure 4.9- Debye ring width, w of 915 nm diameter particle 2DPC at different stages of fabrication. 2DPC were fabricated by self-assembly of 915 nm PS particles on pure water, 0.01 M NaCl and 0.1 M NaCl. Error bars represent one std. dev.

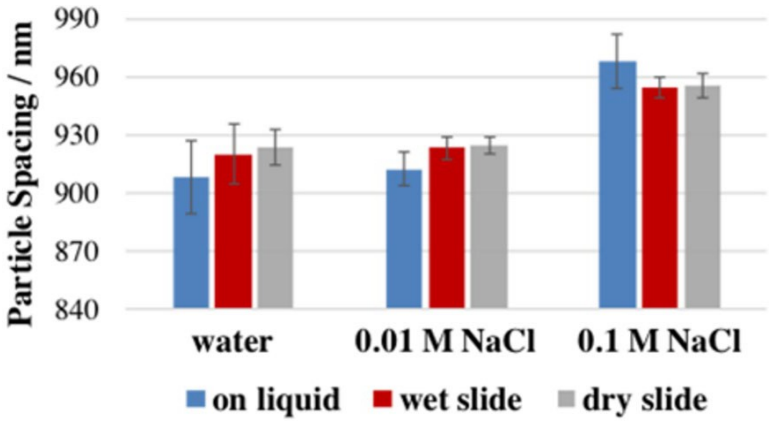

Figure 4.10- Dependence of 2DPC particle spacings for 915 nm diameter particle 2DPC at different stages of fabrication. The Debye ring was measured for a 2DPC at the air-water interface of the crystallization dish (on liquid), at the air-water interface after the 2DPC and a thin water layer are transferred to a slide (wet slide), and after the 2DPC is dried on the slide (dry slide). 2DPC were fabricated by self-assembly of 915 nm PS particles on pure water, and in the presence of 0.01M NaCl and 0.1M NaCl. Error bars represent one standard deviation.

shows that highly ordered close-packed 2DPC can be straight-forwardly fabricated at the air-water interface and transferred to substrates without disrupting 2DPC ordering or particle spacing.

It was recently proposed for the analogous micro-propulsive injection method[10] and other methods[21,48] that capillary attractive interactions between particles during water evaporation playa significant role in formation of the close packed structure. We believe we have shown that for the NTF method immersion capillary forces described by Kralchevsky and Nagayama[48] do not play a significant role in the formation of the close packed structure. The close packed particle array structure is present at the interface.

In a Langmuir-Blodgett trough, close packed hexagonal arrays are formed by compressing the monolayer to the close packed particle spacing after the particles are spread on the water surface.[49] This requires large amounts of sample and instrumentation that controls barrier movement and monitors the surface pressure. The NTF method is an improvement on the

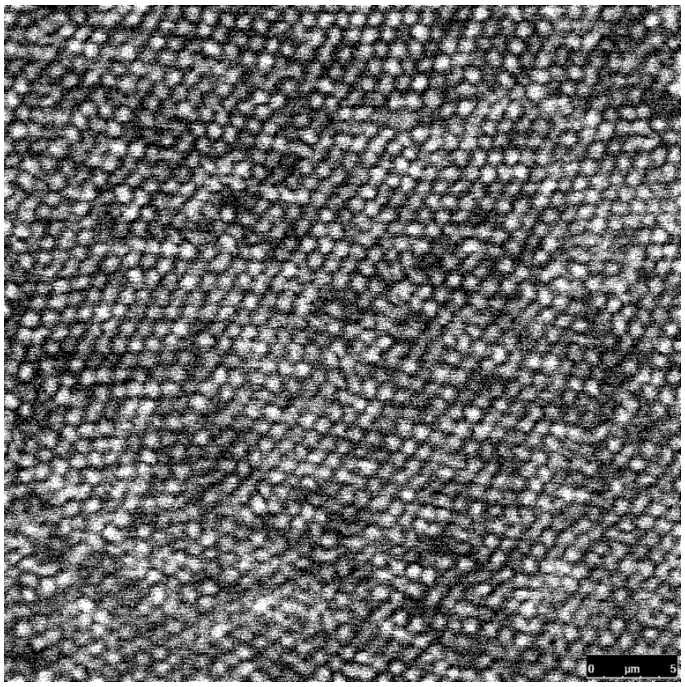

Figure 4.11- Confocal microscope image of 915 nm particles at the air-water interface fabricated using the NTF method. The levels, thresholds, and sharpness in the image were edited using GIMP software so that the particles are clearly visible.

commonly used Langmuir-Blodgett method because it is faster, eliminates expensive instrumentation, avoids compression of the monolayer, and uses less sample.

4.3.4 **Electrostatic Interactions of Charged Particles at the Air-Water Interface**

The electrostatic interactions of charged colloidal particles at the air-water interface are different than the interactions of charged colloidal particles dispersed in solution. Interfacial particles are partially exposed to water so that only the charged groups on the water exposed particle surface can dissociate.[50, 51] The asymmetric ion cloud of the particle creates a dipole moment normal to the air-water interface.[19, 52] Thus, the electrostatic repulsive interaction

Equation 4.6

$$\psi_{ES} = \frac{2q^2e^2}{s\varepsilon(\varepsilon^2-1)} exp^{-s/\mathcal{L}_D} + 2\left(\frac{q\mathcal{L}_D}{\varepsilon}\right)^2 s^{-3}$$

potential, ψ_{ES} (Equation 4.6) of charged interfacial particles has contributions from the screened-Coulomb repulsions (first term of Equation 4.6) and dipole-dipole repulsions (second term of Equation 4.6).[53, 54] The term s is the distance between particle surfaces, q is the particle charge, $\mathcal{L}_D$ is the Debye screening length, and ε is the average of the air and water dielectric constants.

The screened-Coulomb repulsions decay rapidly with distance away from the particle. This short-range interaction dominates ψ_{ES} when the separation between particles is small. Thedipole-dipole repulsions are long range interactions that dominate the potential when distances between particles are large.[53] These long-range repulsive forces have been experimentally observed,[43, 55] theoretically derived,[53] and modeled[56] for charged particles at the air-water or air-oil interface. If the particles are not constrained to a small finite surface area, the dipole-dipole repulsions will create hexagonal particle arrays with spacings larger than the particle diameter.[55]

The electrostatic interaction potential between particles decreases exponentially with distance between particles. The decay rate of the electrostatic interactions increases at higher salt concentrations. The particle surface charges electrostatically interact with ions in solution creating the electric double layer in the electrolyte solution surrounding the particle. Increasing the ion concentration in solution more effectively screens the electrostatic repulsive forces between the ionic interfacial particles and their electric double layers. The electric double layer thickness is roughly given by the Debye length, Equation 4.7, for a 1:1 electrolyte.[57-59] The double layer

Equation 4.7

$$\mathcal{L}_D(nm) = \left((2000e^2 N_A[NaCl])/(\varepsilon_o \varepsilon_w kT)\right)^{1/2}$$

thickness decreases with increasing salt concentration.

The Debye length of charged particles in electrolyte solutions decreases monotonically with increasing salt concentration. $\mathcal{L}_D$ is 966 nm for particles in pure water (assuming an ion concentration of 10^{-7} M), 9.7 nm in 0.001 M NaCl, 3.1 nm in 0.01 M NaCl, 0.97 nm in 0.1 M

NaCl, and 0.31 nm in 1 M NaCl. Accordingly, it is expected that the electrostatic repulsive interaction potential will monotonically decrease as salt concentration increases, which should have negative consequences on 2DPC ordering. Despite the seemingly straight forward relationship between salt concentration and the Debye screening length, both the Debye ring measurements and order parameter calculations show that 2DPC close packed self-assembly and ordering is not impeded by low salt concentrations using the NTF method. In contrast, at NaCl concentrations exceeding 0.01 M NaCl there is a dramatically increased disorder, indicating there is a mechanism counter-balancing the decrease in ψ_{ES} caused by decreasing $\mathcal{L}_D$.

4.3.5 **Mechanism of Self-Assembly for Close Packed Particle Arrays at the Air-Water Interface**

The charged particles dispersed in a water/propanol mixture flow onto the air-water interface from the needle tip due to the large surface tension gradient between the particle dispersion and the water surface.[23, 34, 60] The interfacial particles are transported via Marangoni flow across the water surface towards interfacial areas with the highest surface tension.

Marangoni flow induces the in-plane packing of the particles against the walls of the circular crystallization dish. The particles fill the water surface moving inward from the walls of the dish.This packing force thrusts the particles together so that particles order into a close packed hexagonal array.

The packing force is counter-balanced by the strong electrostatic repulsions that prevent interparticle adhesion and aggregation of random clusters. The electrostatic repulsive interactions between highly charged particles on a pure water surface are larger than the combined attractive Van der Waals interactions and the packing force. The interparticle surface spacings of 2DPC

fabricated by the NTF method are small, therefore the screened-Coulomb repulsions are the dominant electrostatic force driving self-assembly of ordered 2DPC.

The particle mobility gained from the strong electrostatic repulsions give the individual particles time to anneal. Here the term anneal is used to describe the process where individual particles are capable of jiggling around each other on the crowded air-water interface to form the ordered hexagonal 2D particle array with a minimum energy structure.

At low and modest salt concentrations, the particles do not contact one another. The separated particles have a thin water layer between them which lubricates the particle annealing process, to form 2D colloidal crystals. At higher salt concentrations, the electrostatic repulsive interactions are weak and particles approach one another more closely. This increases the probability of interparticle adhesion caused by Van der Waals forces where they collapse into their primary minimum, or they suffer polymer entanglements that could also lead to particle sticking. This stabilizes disorder by slowing or preventing annealing. Disordered 2D arrays formwith increased average interparticle spacing and larger Debye ring widths (Figure 4.6 and Figure4.7). This disorder stems from the aggregation of randomly ordered particle clusters.

The unexpected behaviour of the 2DPC ordering as the ionic strength increases appears to result from adsorption of Cl^- onto the polystyrene particles as is independently shown by the salt concentration dependence of the Zeta potential, ξ shown in Figure 4.12. Chloride anions have been previously shown to adsorb to anionic polystyrene surfaces, increasing the electrophoretic mobility of the particles up to a critical salt concentration.[61, 62] Increasing the saltconcentration further, decreases the electrophoretic mobility due to the collapse of the electric double layer in the high ionic strength solution.

The increase in ξ (more negative) for anionic polystyrene colloids at low concentrationsof NaCl salt results from chloride adsorption.[61, 62] ξ reaches a minimum at a NaCl concentration that is consistent with the critical salt concentration, C* determined from the ordering results. At larger salt concentrations, ξ decreases sharply (less negative) due to compression of the diffuse electric double layer and counter-ion screening. The critical salt concentration, C* at which this transition occurs is dependent on particle diameter. Again, we find the same C* for a certain particle diameter in the Zeta-potential data as in the Debye ring diffraction and order parameter results.

The similarity between the zeta potential, Debye ring measurement, and calculated order parameter results suggests adsorption of Chloride ions onto the polystyrene surface increases the particle anionic surface charge significantly and counteracts the decreasing $\mathcal{L}_D$. Chloride ions adsorbed to the polystyrene surface act as potential determining ions to increase interparticle electrostatic repulsions; this results in better annealing and therefore better ordering of the self-assembled 2DPC.

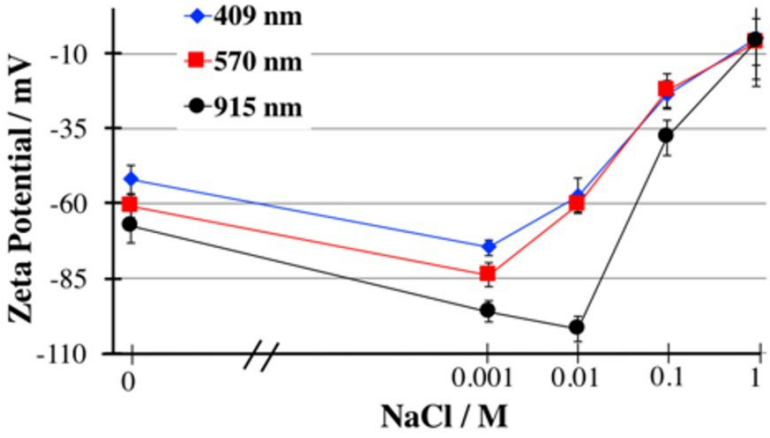

Figure 4.12- Zeta-potentials (mV) for 409, 570, and 915 nm diameter anionic polystyrene particles insolutions as a function of NaCl concentration. Error bars indicate one standard deviation.

4.4 Conclusions

We have shown that utilization of Debye ring measurements is a viable method for monitoring 2DPC ordering for colloidal particle arrays having diameters roughly the size of the wavelengths of visible light. This method could be extended to larger or smaller particles by utilizing Infrared or UV light and a detector. The Debye ring thickness is a reliable indicator of 2DPC order because 2DPC disorder creates larger average particle spacings that decrease the Debye ring inner diameter. Conclusions on 2DPC ordering drawn from Debye ring measurements are consistent with the order parameter found by analysing SEM micrographs ofthe 2DPC.

Using the Debye ring method, we show the NTF method for self-assembly of 2DPC produces highly ordered hexagonal close packed (hcp) monolayers of colloidal particles (diameters= 409, 570, and 915 nm). While investigating the relationship between 2DPC ordering and Debye ring diffraction, we discovered that disorder in the 2DPC does not monotonically increase as salt concentration increases. This behaviour is attributed to chloride anion adsorption to the particle surface. The behaviour of the Zeta potential of particles in salt solutions is analogous to the 2DPC ordering results for 2DPC fabricated on salt solutions. This leads to the conclusion that chloride adsorption increases the particle surface charge which compensates for the decreasing Debye length at low or moderate salt concentrations.

4.5 References

(1) Prather, D. W.; Sharkawy, A.; Shi, S.; Murakowski, J.; Schneider, G., *Photonic Crystals, Theory, Applications and Fabrication*. Wiley Publishing: 2009; p 405.

(2) Rybin, M. V.; Khanikaev, A. B.; Inoue, M.; Samusev, K. B.; Steel, M. J.; Yushin, G.;Limonov, M. F., Fano Resonance between Mie and Bragg Scattering in Photonic Crystals. *Physical Review Letters.* **2009,** *103*, 023901.

(3) van Duffel, B.; Ras, R. H. A.; De Schryver, F. C.; Schoonheydt, R. A., Langmuir- Blodgett deposition and optical diffraction of two-dimensional opal. *Journal of MaterialsChemistry.* **2001,** *11*, 3333-3336.

(4) Chapman, H. N.; Fromme, P.; Barty, A.; White, T. A.; Kirian, R. A.; Aquila, A.; Hunter, M. S.; Schulz, J.; DePonte, D. P.; Weierstall, U.; Doak, R. B.; Maia, F. R. N. C.; Martin, A. V.; Schlichting, I.; Lomb, L.; Coppola, N.; Shoeman, R. L.; Epp, S. W.; Hartmann, R.; Rolles, D.; Rudenko, A.; Foucar, L.; Kimmel, N.; Weidenspointner, G.; Holl, P.; Liang, M.; Barthelmess, M.; Caleman, C.; Boutet, S.; Bogan, M. J.; Krzywinski, J.; Bostedt, C.;Bajt, S.; Gumprecht, L.; Rudek, B.; Erk, B.; Schmidt, C.; Hömke, A.; Reich, C.; Pietschner, D.; Strüder, L.; Hauser, G.; Gorke, H.; Ullrich, J.; Herrmann, S.; Schaller, G.;Schopper, F.; Soltau, H.; Kühnel, K.-U.; Messerschmidt, M.; Bozek, J. D.; Hau-Riege, S.P.; Frank, M.; Hampton, C. Y.; Sierra, R. G.; Starodub, D.; Williams, G. J.; Hajdu, J.; Timneanu, N.; Seibert, M. M.; Andreasson, J.; Rocker, A.; Jönsson, O.; Svenda, M.; Stern, S.; Nass, K.; Andritschke, R.; Schröter, C.-D.; Krasniqi, F.; Bott, M.; Schmidt, K. E.; Wang, X.; Grotjohann, I.; Holton, J. M.; Barends, T. R. M.; Neutze, R.; Marchesini, S.; Fromme, R.; Schorb, S.; Rupp, D.; Adolph, M.; Gorkhover, T.; Andersson, I.; Hirsemann, H.; Potdevin, G.; Graafsma, H.; Nilsson, B.; Spence, J. C. H., Femtosecond X-ray protein nanocrystallography. *Nature.* **2011,** *470*, 73-77.

(5) Elser, V.; Henley, C. L., Crystal and quasicrystal structures in Al-Mn-Si alloys. *Physical Review Letters.* **1985,** *55*, 2883-2886.

(6) Alexander Tikhonov, N. K., Jian-Tao Zhang, Luling Wang, Sanford A. Asher,Relectivity

Enhanced Two-Dimensional Dielectric Particle Array Monoloayer Diffraction. *Journal of Nanophotonics.* **2012,** *6*, 063509-1-063509-9.

(7) Smith, N. L.; Hong, Z.; Asher, S. A., Responsive ionic liquid-polymer 2D photoniccrystal gas sensors. *Analyst.* **2014,** *139*, 6379-6386.

(8) Zhang, J.-T.; Wang, L.; Luo, J.; Tikhonov, A.; Kornienko, N.; Asher, S. A., 2-D Array Photonic Crystal Sensing Motif. *Journal of the American Chemical Society.* **2011,** *133*,9152-9155.

(9) Cai, Z.; Smith, N. L.; Zhang, J.-T.; Asher, S. A., Two-Dimensional Photonic CrystalChemical and Biomolecular Sensors. *Analytical Chemistry.* **2015,** *87*, 5013-5025.

(10) Gao, P.; He, J.; Zhou, S.; Yang, X.; Li, S.; Sheng, J.; Wang, D.; Yu, T.; Ye, J.; Cui, Y., Large-Area Nanosphere Self-Assembly by a Micro-Propulsive Injection Method for High Throughput Periodic Surface Nanotexturing. *Nano Letters.* **2015,** *15*, 4591-4598.

(11) Branham, M. S.; Hsu, W.-C.; Yerci, S.; Loomis, J.; Boriskina, S. V.; Hoard, B. R.; Han, S. E.; Chen, G., 15.7% Efficient 10-μm-Thick Crystalline Silicon Solar Cells UsingPeriodic Nanostructures. *Advanced Materials.* **2015,** *27*, 2182-2188.

(12) Karg, M.; König, T. A. F.; Retsch, M.; Stelling, C.; Reichstein, P. M.; Honold, T.;Thelakkat, M.; Fery, A., Colloidal self-assembly concepts for light management inphotovoltaics. *Materials Today.* **2015,** *18*, 185-205.

(13) Utech, S.; Bley, K.; Aizenberg, J.; Vogel, N., Tailoring re-entrant geometry in inverse colloidal monolayers to control surface wettability. *Journal of Materials Chemistry A.***2016,** *4* (18), 6853-6859.

(14) Bravo, J.; Zhai, L.; Wu, Z.; Cohen, R. E.; Rubner, M. F., Transparent Superhydrophobic Films Based on Silica Nanoparticles. *Langmuir.* **2007,** *23*, 7293-7298.

(15) Li, Y.; Zhang, J.; Zhu, S.; Dong, H.; Jia, F.; Wang, Z.; Sun, Z.; Zhang, L.; Li, Y.; Li, H.;Xu,

W.; Yang, B., Biomimetic Surfaces for High-Performance Optics. *Advanced Materials.* **2009,** *21*, 4731-4734.

(16) Malinsky, M. D.; Kelly, K. L.; Schatz, G. C.; Van Duyne, R. P., Chain Length Dependence and Sensing Capabilities of the Localized Surface Plasmon Resonance of Silver Nanoparticles Chemically Modified with Alkanethiol Self-Assembled Monolayers.*Journal of the American Chemical Society.* **2001,** *123*, 1471-1482.

(17) Das, A.; Zhao, J.; Schatz, G. C.; Sligar, S. G.; Van Duyne, R. P., Screening of Type I andII Drug Binding to Human Cytochrome P450-3A4 in Nanodiscs by Localized Surface Plasmon Resonance Spectroscopy. *Analytical Chemistry.* **2009,** *81*, 3754-3759.

(18) Shinotsuka, K.; Kajita, Y.; Hongo, K.; Hatta, Y., Crystal Perfection of ParticleMonolayer at the Air–Water Interface. *Langmuir.* **2015,** *31*, 11452-11457.

(19) Vogel, N.; Weiss, C. K.; Landfester, K., From soft to hard: the generation of functional and complex colloidal monolayers for nanolithography. *Soft Matter.* **2012,** *8*, 4044-4061.

(20) Zhang, J.; Li, Y.; Zhang, X.; Yang, B., Colloidal Self-Assembly Meets Nanofabrication: From Two-Dimensional Colloidal Crystals to Nanostructure Arrays. *Advanced Materials.***2010,** *22*, 4249-4269.

(21) Lotito, V.; Zambelli, T., Approaches to self-assembly of colloidal monolayers: A guidefor nanotechnologists. *Advances in Colloid and Interface Science*. **2017**, 246, 217-274.

(22) Xie, X. N.; Chung, H. J.; Sow, C. H.; Wee, A. T. S., Nanoscale materials patterning and engineering by atomic force microscopy nanolithography. *Materials Science and Engineering: R: Reports.* **2006,** *54*, 1-48.

(23) Zhang, J.-T.; Wang, L.; Lamont, D. N.; Velankar, S. S.; Asher, S. A., Fabrication of Large-Area Two-Dimensional Colloidal Crystals. *Angewandte Chemie InternationalEdition.* **2012,** *51*,

6117-6120.

(24) Ogi, T.; Modesto-Lopez, L. B.; Iskandar, F.; Okuyama, K., Fabrication of a large area monolayer of silica particles on a sapphire substrate by a spin coating method. *Colloids and Surfaces A: Physicochemical and Engineering Aspects.* **2007,** *297*, 71-78.

(25) Truzzolillo, D.; Sharaf, H.; Jonas, U.; Loppinet, B.; Vlassopoulos, D., Tuning the Structure and Rheology of Polystyrene Particles at the Air–Water Interface by Varyingthe pH. *Langmuir.* **2016,** *32*, 6956-6966.

(26) Kim, J. Y.; Kwon, S. J.; Chang, J.-B.; Ross, C. A.; Hatton, T. A.; Stellacci, F., Two-Dimensional Nanoparticle Supracrystals: A Model System for Two-Dimensional Melting. *Nano Letters.* **2016,** *16*, 1352-1358.

(27) Hu, M.; Chujo, S.; Nishikawa, H.; Yamaguchi, Y.; Okubo, T., Spontaneous formation of large-area monolayers of well-ordered nanoparticles via a wet-coating process. *Journal of Nanoparticle Research.* **2004,** *6*, 479-487.

(28) Ho, C.-C.; Chen, P.-Y.; Lin, K.-H.; Juan, W.-T.; Lee, W.-L., Fabrication of Monolayer of Polymer/Nanospheres Hybrid at a Water-Air Interface. *ACS Applied Materials & Interfaces.* **2011,** *3*, 204-208.

(29) Retsch, M.; Zhou, Z.; Rivera, S.; Kappl, M.; Zhao, X. S.; Jonas, U.; Li, Q., Fabrication of Large-Area, Transferable Colloidal Monolayers Utilizing Self-Assembly at the Air/Water Interface. *Macromolecular Chemistry and Physics.* **2009,** *210*, 230-241.

(30) Okubo, T.; Chujo, S.; Maenosono, S.; Yamaguchi, Y., Microstructure of Silica Particle Monolayer Films Formed by Capillary immersion Force. *Journal of Nanoparticle Research.* **2003,** *5*, 111-117.

(31) Rödner, S. C.; Wedin, P.; Bergström, L., Effect of Electrolyte and Evaporation Rate on the

Structural Features of Dried Silica Monolayer Films. *Langmuir.* **2002,** *18*, 9327-9333.

(32) Grzelczak, M.; Vermant, J.; Furst, E. M.; Liz-Marzán, L. M., Directed Self-Assembly of Nanoparticles. *ACS Nano.* **2010,** *4*, 3591-3605.

(33) Minh, N. V.; Hue, N. T.; Lien, N. T. H.; Hoang, C. M., Close-packed monolayer self-assembly of silica nanospheres assisted by infrared irradiation. *Electronic Materials Letters.* **2017**, 14, 64-69.

(34) Zhang, J.-T.; Wang, L.; Chao, X.; Velankar, S. S.; Asher, S. A., Vertical spreading of two-dimensional crystalline colloidal arrays. *Journal of Materials Chemistry C.* **2013,** 38,6099-6102.

(35) Zhang, F.; Cao, L.; Yang, W., Preparation of Monodisperse and Anion-Charged Polystyrene Microspheres Stabilized with Polymerizable Sodium Styrene Sulfonate by Dispersion Polymerization. *Macromol. Chem. Phys.* **2010,** *211*, 744-751.

(36) Reese, C. E.; Asher, S. A., Emulsifier-Free Emulsion Polymerization Produces Highly Charged, Monodisperse Particles for Near Infrared Photonic Crystals. *Journal of Colloidand Interface Science.* **2002,** *248*, 41-46.

(37) Zhang, J.-T.; Chao, X.; Liu, X.; Asher, S. A., Two-dimensional array Debye ring diffraction protein recognition sensing. *Chemical Communications.* **2013,** *49*, 6337-6339.

(38) Bohn, J. J.; Ben-Moshe, M.; Tikhonov, A.; Qu, D.; Lamont, D. N.; Asher, S. A., Charge stabilized crystalline colloidal arrays as templates for fabrication of non-close-packed inverted photonic crystals. *J. Colloid Interface Sci.* **2010,** *344*, 298-307.

(39) Rengarajan, R.; Mittleman, D.; Rich, C.; Colvin, V., Effect of disorder on the optical properties of colloidal crystals. *Physical Review E.* **2005,** *71*, 016615.

(40) Zhang, J.-T.; Chao, X.; Asher, S. A., Asymmetric Free-Standing 2-D Photonic CrystalFilms and Their Janus Particles. *Journal of the American Chemical Society.* **2013,** *135*,11397-11401.

(41) Xue, F.; Asher, S. A.; Meng, Z.; Wang, F.; Lu, W.; Xue, M.; Qi, F., Two-dimensional colloidal crystal heterostructures. *RSC Advances.* **2015,** *5*, 18939-18944.

(42) Weitenberg, C.; Schauß, P.; Fukuhara, T.; Cheneau, M.; Endres, M.; Bloch, I.; Kuhr, S., Coherent Light Scattering from a Two-Dimensional Mott Insulator. *Physical Review Letters.* **2011,** *106*, 215301.

(43) Pieranski, P., Two-Dimensional Interfacial Colloidal Crystals. *Physical Review Letters.* **1980,** *45*, 569-572.

(44) Schmudde, M.; Grunewald, C.; Goroncy, C.; Noufele, C. N.; Stein, B.; Risse, T.; Graf, C., Controlling the Interaction and Non-Close-Packed Arrangement of Nanoparticles onLarge Areas. *ACS Nano.* **2016,** *10*, 3525-3535.

(45) Lotito, V.; Zambelli, T., Self-Assembly of Single-Sized and Binary Colloidal Particles at Air/Water Interface by Surface Confinement and Water Discharge. *Langmuir.* **2016,** *32*, 9582-9590.

(46) Reincke, F.; Kegel, W. K.; Zhang, H.; Nolte, M.; Wang, D.; Vanmaekelbergh, D.; Mohwald, H., Understanding the self-assembly of charged nanoparticles at the water/oilinterface. *Physical Chemistry Chemical Physics.* **2006,** *8*, 3828-3835.

(47) Yoshida, H.; Ito, K.; Ise, N., Colloidal crystal growth. *Journal of the Chemical Society, Faraday Transactions.* **1991,** *87*, 371-378.

(48) Kralchevsky, P. A.; Nagayama, K., Capillary forces between colloidal particles. *Langmuir.* **1994,** *10*, 23-36.

(49) Bardosova, M.; Pemble, M. E.; Povey, I. M.; Tredgold, R. H., The Langmuir-Blodgett Approach to Making Colloidal Photonic Crystals from Silica Spheres. *Advanced Materials.* **2010,** *22*, 3104-3124.

(50) Paunov, V. N., Novel Method for Determining the Three-Phase Contact Angle of Colloid Particles Adsorbed at Air−Water and Oil−Water Interfaces. *Langmuir.* **2003,** *19*, 7970- 7976.

(51) Aveyard, R.; Clint, J. H.; Nees, D.; Paunov, V. N., Compression and Structure of Monolayers of Charged Latex Particles at Air/Water and Octane/Water Interfaces.*Langmuir.* **2000,** *16*, 1969-1979.

(52) Bossa, G. V.; Bohinc, K.; Brown, M. A.; May, S., Dipole Moment of a Charged Particle Trapped at the Air–Water Interface. *The Journal of Physical Chemistry B.* **2016,** *120*, 6278-6285.

(53) Hurd, A. J., The electrostatic interaction between interfacial colloidal particles. *Journal of Physics A: Mathematical and General.* **1985,** *18*, L1055.

(54) Wu, S.; Nikolov, A.; Wasan, D., Role of Collective Interactions in Self-Assembly of Charged Particles at Liquid Interfaces. *The Canadian Journal of Chemical Engineering.***2007,** *85*, 562-569.

(55) Nikolaides, M. G.; Bausch, A. R.; Hsu, M. F.; Dinsmore, A. D.; Brenner, M. P.; Gay, C.; Weitz, D. A., Electric-field-induced capillary attraction between like-charged particles atliquid interfaces. *Nature.* **2002,** *420*, 299-301.

(56) Girotto, M.; dos Santos, A. P.; Levin, Y., Interaction of Charged Colloidal Particles at the Air–Water Interface. *The Journal of Physical Chemistry B.* **2016,** *120*, 5817-5822.

(57) Okubo, T., Extraordinary behavior in the structural properties of colloidal macroions in deionized suspension and the importance of the Debye screening length. *Accounts of Chemical Research.* **1988,** *21*, 281-286.

(58) Hunter, R. J., *Zeta Potential in Colloid Science*. Academic Press Inc: New York, NewYork, 1981; p 386.

(59) Hiemenz, P. C., *Principles of Colloid and Surface Chemistry*. 2nd ed.; Marcel Dekker,Inc:

New York, New York, 1986.

(60) Dong, L.; Johnson, D., Surface Tension of Charge-Stabilized Colloidal Suspensions at the Water−Air Interface. *Langmuir.* **2003,** *19*, 10205-10209.

(61) Elimelech, M.; O'Melia, C. R., Effect of electrolyte type on the electrophoretic mobilityof polystyrene latex colloids. *Colloids and Surfaces.* **1990,** *44*, 165-178.

(62) Ma, C. M.; Micale, F. J.; El-Aasser, M. S.; Vanderhoff, J. W., The Relationship Betweenthe Electrophoretic Mobility and the A dsorption of Ions on Polystyrene Latex. In Emulsion Polymers and Emulsion Polymerization, *Journal of the American Chemical Society.* **1981**, *165*, 251-262.

5.0 Mechanisms by which Organic Solvent Exchange Transforms Responsive Hydrogels into Responsive Organogels

This chapter was published as Smith, N. L.; Coukouma, A.E.; Jakubek, R.S.; Asher, S. A. **Biomacromolecules** 2019

Author Contributions: A.E.C and N.L.S. fabricated samples and measured swelling ratios. A.E.C. performed titration experiments. N.L.S performed Cryo-SEM imaging at the University of Minnesota Characterization Facility with assistance from Chris Frethem and Hanseung Lee. N.L.S. measured the organogel NIR absorbance and calculated the solvation shell waters. R.S.J. performed the UVRR experiments and calculations of protein secondary structure. N.L.S determined VPT mechanisms with assistance from S.A.A and A.E.C. The manuscript was prepared by N.L.S with assistance from S.A.A.

Responsive pure protein organogel sensors and catalysts are fabricated by replacing the aqueous mobile phase of protein hydrogels with pure ethylene glycol (EG). Exchanging water for EG causes irreversible volume phase transitions (VPT) in bovine serum albumin (BSA) polymers; however, BSA hydrogel and organogel sensors show similar volume responses to protein−ligand binding. This work elucidates the mechanisms involved in this enabling irreversible VPT by examining the protein secondary structure, hydration, and protein polymer morphology. Organogel proteins retain their native activity because their secondary structure and hydration shell are relatively unperturbed by the EG exchange. Conversely, the decreasing solvent quality initiates polymer phase separation to minimize the BSA polymer surface area exposed to EG, thus decreasing distances between BSA polymer strands. These protein polymer morphology changes promote interprotein interactions between BSA polymer strands, which increase the effective

polymer cross-link density and prevent organogel swelling as the mobile phase is exchanged back to water.

5.1 Introduction

Hydrogels and organogels are versatile materials with numerous applications as sensors,[1−5] catalysts,[6,7] drug delivery materials,[8,9] tissue engineering scaffolds,[10] wound dressings,[11] membranes,[12] and mechanical actuators.[13] These responsive materials consist of two primary components: a stationary phase made up of a 3-dimensional chemically or physically cross-linked polymer network and a liquid mobile phase that facilitates diffusion and mass transport within the polymer network. Hydrogels contain an aqueous mobile phase, whereas organogels contain an organic solvent mobile phase.

Our group pioneered the development of photonic crystal- based colorimetric chemical sensors[14,15] that utilize the hydrogel volume phase transition (VPT) responses to external stimuli such as pH, light, and chemical analytes.[4,16−19] Hydrogels or organogels that have molecular recognition groups attached to the polymer network selectively undergo VPT in response to a specific analyte.[17,18,20,21] This analyte-induced VPT shifts the embedded photonic crystal particle spacing, thus shifting the photonic crystal light diffraction.[14−16] These VPT involve distinct changes in the hydrogel/organogel volume in response to small changes in the hydrogel/organogel chemical environment.[22] These volume changes are caused by osmotic pressures, Π, which derive from changes in the Gibbs free energy, ΔG_{total}.[23,24] Osmotic pressures in the system induce mass transfer of the mobile phase: either partitioning the mobile phase into the polymer network to cause swelling, or expelling the mobile phase to cause shrinking. When the polymer and

mobile phase are at equilibrium, $\Pi_{total} = \partial\Delta G_{total}/\partial V = 0$. In general, for hydrogel/organogel chemical sensors, analyte recognition must induce a change in the Gibbs free energy to actuate a VPT.

Recently, we developed several stimuli responsive pure protein hydrogels that sense pH, glucose, yeast cells, drugs, surfactants, and fatty acids.[3,5,25] These protein hydrogels have selective chemical responses because the constituent proteins show specific molecular recognition. There exists a large body of research developing functional pure protein hydrogels using a variety of fabrication methods, such as glutaraldehyde cross-linking, or enzyme catalyzed cross-linking of proteins, and self-assembly of engineered proteins.[6,7,9,26–28]

There are very few studies of pure protein organogels,[29,30] despite the intense interests in utilizing protein chemistries in organic solvents for industrial applications such as enzymatic synthesis of pharmaceuticals and biofuels,[31,32] as well as for sensing and degrading toxic compounds important to the defense industry.[33,34] Organic solvents typically denature proteins and significantly decrease protein reactivity.[35] This has led to the development of several techniques to stabilize proteins against denaturation or deactivation by organic solvents.[36–38]

We very recently developed methods to fabricate stimuli responsive pure protein organogels for sensing and catalysis applications.[39] The pure protein organogels are fabricated from pure protein hydrogels by using a stepwise solvent exchange that replaces the aqueous mobile phase of pure protein hydrogels with ethylene glycol (EG). Chemically cross-linked pure protein polymer hydrogels are fabricated by polymerizing protein monomers in solution using glutaraldehyde. The proteins are immobilized by this protein polymerization such that the proteins retain their native reactivity after the aqueous mobile phase is replaced with pure EG. Protein

immobilization is a widely used strategy to stabilize proteins against denaturation, which typically enhances protein activity in organic solvents.[36,37,40−44]

We believe that our photonic crystal BSA organogel sensor[39] is the first reported responsive pure protein organogel to exhibit a VPT in response to ligand binding. The polymerized BSA in the organogels bind the same ligands as do the BSA hydrogels[3] and the native protein monomers.[45,46] The BSA hydrogels and organogels also exhibit similar VPT responses to ligand binding, swelling when BSA binds charged ligands like ibuprofen and fatty acids.

Recent publications have investigated conformational changes[98] and phase transitions[99] in dipeptide organogels. For example, Yuan et al.[99] demonstrated that self-assembled diphenylalanine organogels are responsive to changes in the solvent composition. The addition of chloroform to the hexafluoropropanol/toluene mobile phase caused organogel swelling, whereas the addition of water caused a gel to crystal transition. The development of more selective responsive hydrogel and organogel materials is enabled by utilizing proteins instead of simple dipeptide molecules because proteins have evolved to have specific ligand binding pockets. However, the responsive protein polymers reported on here and in our previous publication[39] have substantially more complex polymer−mobile phase interactions compared to the homogeneous dipeptide organogels, due to their heterogeneous composition of 20 possible amino acids, leading to interesting VPT phenomenon in response to environmental changes.

The water to EG solvent exchange that transforms responsive BSA hydrogels into responsive BSA organogels induces a large VPT that decreases the organogel volume as the concentration of EG in the mobile phase increases. As shown herein, this solvent exchange induced VPT is irreversible; rehydrating the BSA organogel by exchanging the EG mobile phase back to water does not result in reswelling.

This VPT irreversibility is enabling for developing our selective protein organogel sensors because it creates chemical sensors that are insensitive to fluctuations in humidity and water concentration, thus increasing their potential applications. EG was utilized as the mobile phase due to its low vapor pressure. Protein organogels that utilize an EG mobile phase are more resistant to evaporation compared to protein hydrogels, increasing the time scales these responsive materials can function when exposed to ambient conditions. Thus, these responsive protein organogels with low vapor pressure mobile phases could be utilized for sensing gas phase analytes. EG is hydroscopic, therefore, the organogel's insensitivity to the EG water content is highly advantageous for developing gas sensing materials as it eliminates false negatives and positives that may result from changes in humidity.

In this work, we characterize the protein secondary structure, protein hydration, and the protein polymer morphology in the BSA hydrogels, organogels, and water incubated organogels in order to elucidate the mechanisms involved in this irreversible VPT. The BSA secondary structure in the hydrogel, organogel, and water incubated organogel is determined using the UVRR $AmIII_3$ band frequencies that are sensitive to changes in the peptide secondary structure.[47] The protein solvation shell water layer in the BSA organogel is estimated using the strong NIR absorbance of water. Cryo-SEM is used to image the morphology of the BSA hydrogels and water incubated organogels, elucidating the super- molecular structure of the protein polymer networks. The change in the protein polymer surface area exposed to the mobile phase is determined by titrating the BSA amino acid carboxyl groups.

We discuss the chemistry and mechanisms involved in the BSA hydrogel to organogel transformation that result in this large irreversible VPT shrinking. VPT that dramatically decrease the volume of cross-linked polymer networks are often driven by polymer phase separations; for

example, the extraordinarily large VPT of p(isopropylacrylamide) hydrogels is caused by lower critical solution temperature phase separation, which is initiated by a hydrophobic collapse of the isopropyl groups from water.[48,49] We posit that the origin of the irreversible VPT stems from interprotein interactions formed during the BSA polymer phase separation. These interprotein interactions act as additional polymer network cross-links that prevent BSA polymer swelling of the water incubated organogel.

5.2 Experimental Section

5.2.1 **Materials**

BSA (>98%; lyophilized powder, essentially fatty acid free) and Sigmacote were purchased from Sigma-Aldrich and used as received. Glutaraldehyde (50 wt %) in water was purchased from Sigma-Aldrich and diluted to 12.5 wt % glutaraldehyde with nanopure water. Ethylene glycol (certified, <0.2% water) was purchased from Fisher Chemical and used as received. Nanopure water was produced using a Barnstead NANOpure infinity system. Type A brass planchets were purchased from Ted Pella.

5.2.2 **Fabrication of BSA Hydrogel, Organogels, and Organogel Incubated in Water**

BSA hydrogels were fabricated by polymerizing BSA monomers in solution using glutaraldehyde to form covalent linkages between BSA lysine residues, as described in our previous publications.[3] Glass microscope slides were treated with Sigmacote to make their surfaces

hydrophobic. A ~410 μm thick spacer was created by adhering layers of 3 M Scotch Magic Greener tape along the four edges of the slide. The spacer ensures that the polymerized hydrogel film has a uniform thickness.

A 200 mg/mL BSA stock solution was prepared by dissolving lyophilized BSA powder in nanopure water. BSA hydrogel polymerization was initiated by adding 64 μL of a 12.5 wt % glutaraldehyde solution to 1.0 mL of the BSA stock solution. The solution was shaken to mix the components, and then poured onto the glass slide within the spacer. A second glass slide was placed on top and pressed firmly into the spacer to expel excess solution. The BSA/glutaraldehyde solution was polymerized for 3 h at room temperature. After polymerization, the slides were separated, releasing the BSA hydrogel films. BSA hydrogels were washed with large amounts of nanopure water for 2 days to remove unreacted BSA and glutaraldehyde.

BSA organogels were fabricated by using a stepwise solvent exchange process that replaces the aqueous mobile phase with EG.[39] BSA hydrogels were incubated in aqueous solutions containing increasing concentrations of EG for 24 h each during which the solvent was replaced 3 times with ~250 mL of fresh solution. The samples were placed on a shaker to mix the BSA gels and solution during the exchange. The BSA hydrogels were transferred from nanopure water to 30% (v/v) EG in water, then to 50% (v/v) EG in water, and then to 70% (v/v) EG in water. Finally, the BSA gels were equilibrated with pure EG for 2 days to complete the solvent exchange. The ~250 mL volume of pure EG was replaced 6 times over those 2 days to ensure that excess water was removed from the mobile phase.

Water incubated BSA organogels were fabricated by exchanging the pure EG mobile phase of BSA organogels back to pure water. The stepwise solvent exchange described above was reversed; BSA organogels were incubated for 24 h on the shaker in 70% (v/v) EG, followed by

50% (v/v) EG, and then 30% (v/v) EG. The ~250 mL volume of solvent was replaced 3 times each day. Finally, the organogels were incubated in nanopure water for 3 days where ~250 mL of fresh water was replaced 4 times daily to ensure that all the EG was removed from the mobile phase.

5.2.3 **Volume Phase Transition Measurements**

Directly after polymerization of the BSA hydrogels, before washing the hydrogels in water, the hydrogel films were cut into smaller square pieces using a razor blade. The dimensions of each piece were measured using a digital micrometer. The precisely measured hydrogel samples were washed in nanopure water followed by the stepwise solvent exchange steps described above. The dimensions of the hydrogel/organogel samples were measured after incubation in each solvent composition. The BSA hydrogel pieces exist as free-floating films that appear to swell isotropically. Therefore, the hydrogel and organogel volumes can be calculated from the measured gel areas using the swelling ratio $(\frac{A}{A_i})^{3/2} = \frac{V}{V_i}$, where A_i and V_i are the initial area and volume of the BSA hydrogel piece directly after polymerization, while A and V are the area and volume of the BSA hydrogel or organogel after incubating in a particular EG/water solution.

The initial BSA concentration in the hydrogel directly after polymerization is 200 mg/mL. This concentration corresponds to an initial BSA polymer volume fraction of ϕ_i = 15%, given the specific volume of BSA in water is 0.734 cm^3/g.[50] The BSA polymer volume fraction in the hydrogel or organogel after swelling or shrinking in solvent is calculated using the volume swelling ratio (eq 5.1).

Equation 5.1

$$\phi = \phi_i \times \frac{V}{V_i}$$

5.2.4 **UV Resonance Raman Spectroscopy of BSA Hydrogels and Organogels**

UV Resonance Raman (UVRR) spectroscopy was used to investigate the secondary structure of BSA monomers free in solution and polymerized BSA in the hydrogel, organogel, and water incubated organogel.

The instrumentation used was previously described in detail by Bykov et al.[51] We generated ~204 nm excitation light by first frequency tripling the fundamental of a Nd:YAG laser to ~355 nm. The ~355 nm light was then Raman shifted to ~204 nm using the fifth anti-Stokes harmonic of hydrogen gas (30 psi). The 204 nm light was focused onto a spinning Suprasil quartz NMR tube containing the sample, and a ~165° backscattering geometry was used to collect the scattered light. The scattered light was dispersed using a home-built double spectrometer in a subtractive configuration. The dispersed light was imaged using a liquid nitrogen cooled back-thinned CCD camera (Princeton Instruments) with a Lumogen E coating.

5.2.5 **NIR Absorption Measurements of BSA Organogel Water Content**

The strong water absorption band at 1915 nm was used to calculate the water content in BSA organogels using a protocol similar to that of our previous publication.[16] The NIR absorption between 1400 and 2000 nm was measured for solutions containing 1.6 mL of EG and 0, 5, 10, 15, 20, and 25 μL water in a 5 mm path length quartz cuvette.

The absorption of 1 and 2 layers of the BSA organogel film was also measured. The 420 μm thick organogel film was cut to the size of the cuvette inner wall (~1 cm × 4 cm). Excess EG on the surface of the organogel films was removed by blotting the films with filter paper until the

surface appeared dry. The film was then placed on the wall of the quartz cuvette. Experimental details of these measurements are provided in the Supporting Information. The Supporting Information also includes the NIR absorbance of the EG/water solutions and the BSA organogels, the calibration curve for water absorption in EG at 1915 nm, and discusses the calculation of the water concentration in the organogel.

5.2.6 **Cryo-SEM of BSA Hydrogels and Water Incubated BSA Organogels**

5.2.6.1 Preparation of BSA Solution, BSA Hydrogel, and Water Incubated BSA Organogel Samples for Cryo-SEM

Cryo-SEM imaging was performed at the University of Minnesota College of Science and Engineering Characterization Facility in collaboration with Chris Fretham and Hanseung Lee.

BSA was dissolved in nanopure water to make 200 mg/mL BSA solutions. The BSA solution samples were prepared for Cryo-SEM by sandwiching a 3 μL aliquot of this BSA solution between two brass planchets. The Ted Pella Type A planchets were 3 mm in diameter. They contained a 2 mm diameter, 100 μm deep well in the center. The cylindrical cavity between the planchets that contained the samples was 200 μm thick.

The BSA hydrogel samples were prepared by polymerizing the BSA/glutaraldehyde solution between two Type A brass planchets, in the 2 mm diameter, 200 μm thick cavity. The surface of the brass planchets was abraded prior to hydrogel polymerization to promote adhesion between the hydrogel and planchet so that the hydrogels fractured after freezing.

Cryo-SEM imaging requires sublimation of the water mobile phase to reveal the polymer stationary phase. Protocols to flash freeze pure EG and subsequently sublimate the EG mobile phase do not currently exist. Therefore, the EG mobile phase was exchanged back to water to form

the water incubated organogel as described above. The thickness of the water incubated organogel film was between 0.18 and 0.2 μm after the solvent exchange process was completed. A specialized die was fabricated by the University of Pittsburgh machine shop and used to cut 1.8 mm diameter discs from the BSA organogel films. These organogel discs fit snuggly into the 2 mm diameter/0.2 mm thick cavity between the two Type A brass planchets.

High pressure flash freezing of the samples between brass planchets was done using a BAL-TEC HPM 010 high pressure freezing machine at 2100 bar with liquid nitrogen (LN2). High pressure freezing promotes formation of vitreous ice and prevents the formation of ice crystals that can destroy the delicate network structure.52 Samples were stored under constant cryogenic temperatures.

The planchets containing frozen samples were affixed to the sample holder while still immersed in a LN2 bath. A photograph of the sample holder is shown in Figure S1 of the Supporting Information. The sample holder was then transferred to the Leica EM ACE600 high vacuum sputter coater using the Leica VCT100 shuttle. The Leica VCT100 shuttle and the Leica EM ACE600 instrument were cooled with LN2 prior to transferring the samples. It is important that the sample remains at cryogenic temperatures to avoid ice crystal formation. The pressure and temperature inside the chambers were maintained at 1.5×10^{-5} mbar and at −166 °C. A cold knife was used to remove the top planchet, fracturing the sample to reveal the inner hydrogel and organogel polymer networks.

Vitrified ice in the interstitial spaces of the protein polymer network was removed by sublimation, a process sometimes referred to as Cryo-etching.[52] The temperature inside the chamber was increased from −166 to −100 °C at a rate of 3 °C/min. The pressure was kept at 1.5×10^{-5} mbar. The sample was held at −100 °C for 40 min to allow significant sublimation of vitreous

ice at the surface. This reveals the protein polymer network. A cold trap kept at −160 °C was placed over the sample to prevent sublimated water vapor from condensing back onto the sample. After 40 min, the temperature was decreased to −115 °C, halting the sublimation of water. After sublimation, samples were sputter coated, depositing a 2.5 ± 0.03 nm layer of platinum on the sample. The thickness of the Pt coating was determined by the frequency shift of a quartz crystal oscillator, calibrated for the density of the Pt deposited.

5.2.6.2 Cryo-SEM of Frozen Hydrated BSA Hydrogels and Water Incubated Organogels

The samples were transferred to the Hitachi SU8230 *fi*eld emission gun scanning electron microscope under vacuum at cryogenic temperatures in the Leica VCT100 shuttle. The Leica VCT100 Cryo-stage temperature was maintained at −115 °C throughout imaging. Samples were examined using low accelerating voltages (0.8−2 kV) to avoid charging and subsequent damage to the sample. Samples were left in the SEM chamber overnight under vacuum after Cryo-SEM imaging was complete. As the temperature inside the vacuum chamber slowly increased throughout the night, the samples became freeze-dried. The freeze-dried samples were imaged the next day before the SEM was cooled with LN_2. The stage temperature was ∼10 °C during SEM imaging of the freeze-dried samples.

We used the NIH software ImageJ[53] to analyze the BSA polymer networks in the Cryo-SEM micrographs. The BSA polymer strand diameters, pore diameters, and the length of the protein polymer strands were measured in several Cryo-SEM images and averaged.

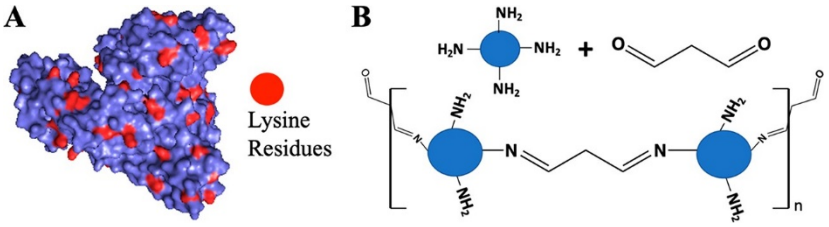

Figure 5.1- (A) BSA protein structure showing lysine residues highlighted in red. Structure obtained from RCSB Protein Data Bank, 3V03. Image made using PyMol software. (B) One of the possible glutaraldehyde interprotein cross-linking reactions; the aldehyde and lysine amine group form a Schiff base that covalently

5.2.7 **Titration of BSA Hydrogels and Water Incubated Organogels**

BSA hydrogels were prepared as described above and cut to various sizes directly after polymerization before incubating in water. The concentrations of BSA in these BSA hydrogels are 200 mg/mL. The area of each freshly prepared 420 μm thick BSA hydrogel piece was measured and the moles of protein contained in each BSA hydrogel piece was calculated from its volume. The hydrogel samples were then equilibrated in nanopure water.

Half of the BSA hydrogel samples were transformed to BSA organogels using the stepwise EG exchange process. These organogel samples were then rehydrated with nanopure water by reversing the stepwise solvent exchange process. These samples were then incubated in water for 3 days, during which the water was replaced twice daily with fresh nanopure water.

The BSA hydrogels and water incubated organogels were placed in 2 mL of pH 7.5 nanopure water. The pH was monitored using a Hanna Instruments HI5522 pH meter with a Hanna Instruments HI1083 microelectrode as 5−20 μL aliquots of 0.1 M HCl titrant were added to the solutions containing the gels. After each addition of HCL, the solution was mixed for 15 min before the pH was recorded. The pH was then plotted against $\frac{mol\ HCl\ added}{mol\ BSA}$. Six replicate measurements were performed for both the BSA hydrogels and water incubated organogels.

5.3 Results and Discussion

Responsive pure protein hydrogels are fabricated by polymerizing BSA protein monomers using glutaraldehyde to form covalent linkages between BSA lysine residues (Figure 5.1). Glutaraldehyde is a commonly used protein cross-linker and fixative that has little impact on the native protein structure and the native protein reactivity.[41,54] We use the term "interprotein cross-links" to specifically describe the short glutaraldehyde linkages between BSA proteins in the pure protein polymer chains. This is distinct from the polymer cross- links that define points where the protein polymer chains interconnect to form the 3-dimensional hydrogel polymer network.

Glutaraldehyde is most reactive toward lysine residues on the protein surface.54 BSA contains 60 lysine residues, 34 of which are located on the BSA surface (Figure 5.1A) and are available for glutaraldehyde interprotein cross-linking.[55] The BSA surface lysine residues are up to 20−24 Å apart.[55] Glutaraldehyde reacts in aqueous solutions to form a mixture of glutaraldehyde monomers and glutaraldehyde polymers of various lengths.[54] Thus, both interprotein and intraprotein cross-linking can occur.

Intraprotein cross-linking is favored at low protein and glutaraldehyde concentrations.[54] At high protein concentrations and at higher glutaraldehyde/protein ratios (typically>25), interprotein cross-linking is favored.[54] The 27 glutaraldehyde/BSA ratio that was used to polymerize the 200 mg/mL BSA solution should favor interprotein cross- linking over intraprotein cross-linking, forming a polymer of covalently linked protein monomers. One possible interprotein cross-linking reaction is shown in Figure 5.1B, where monomeric glutaraldehyde reacts with two lysine residues to form a Schiff base. The formation of interprotein cross-links is evident from the formation of the insoluble protein polymer network that makes up the hydrogel. These elastic BSA hydrogels are sufficiently robust to be easily handled.

5.3.1 **Cryo-SEM Imaging of BSA Hydrogel Morphology and Topology**

We utilized Cryo-SEM to image the BSA hydrogel morphology in the hydrated state.[52,56,57] The hydrogel morphology is defined as the supermolecular structure of the 3D polymer network that gives rise to the polymer strand diameters, polymer strand lengths, and the network pore sizes.[58,59] Polymer morphology can significantly impact the hydrogel properties, such as their swelling behavior, which affects hydrogel sensing and drug release behaviors, and their mechanical properties.[12,60] For example, hydrogel networks with increased cross-link density form increasingly more robust materials that exhibit smaller VPT in response to analyte recognition.

Macroscopically, our BSA hydrogels are transparent and appear to be homogeneous films. These BSA hydrogel films also exhibit homogeneous and isotropic VPT swelling in response to hydrogel protein−ligand binding.[3,39] At the nano- and/or microscale, the BSA hydrogel supermolecular structure appears relatively heterogeneous, as shown in Figure 5.2. The BSA hydrogel network pore sizes have a large distribution of diameters, ranging from ∼50 to ∼200 nm.

The Cryo-SEM micrographs reveal a discernible BSA polymer network once the vitreous ice is sublimed from the sample (Figure 5.2A−D). The 40 min sublimation time removes most of the bulk water near the sample surface, revealing the protein polymer network morphology of our frozen hydrated BSA hydrogel. Figure 5.2B shows an area with many patches of vitreous ice remaining on the sample. The red arrow in Figure 5.2B points to one of these remaining vitreous ice patches. BSA is a hydrophilic water-soluble protein. Thus, solvation shell waters will be difficult to sublimate under these conditions in 40 min and will tend to remain bound to the polymerized BSA. Shown in Figure 5.2A−D, the hydrogel consists of a 3D network of

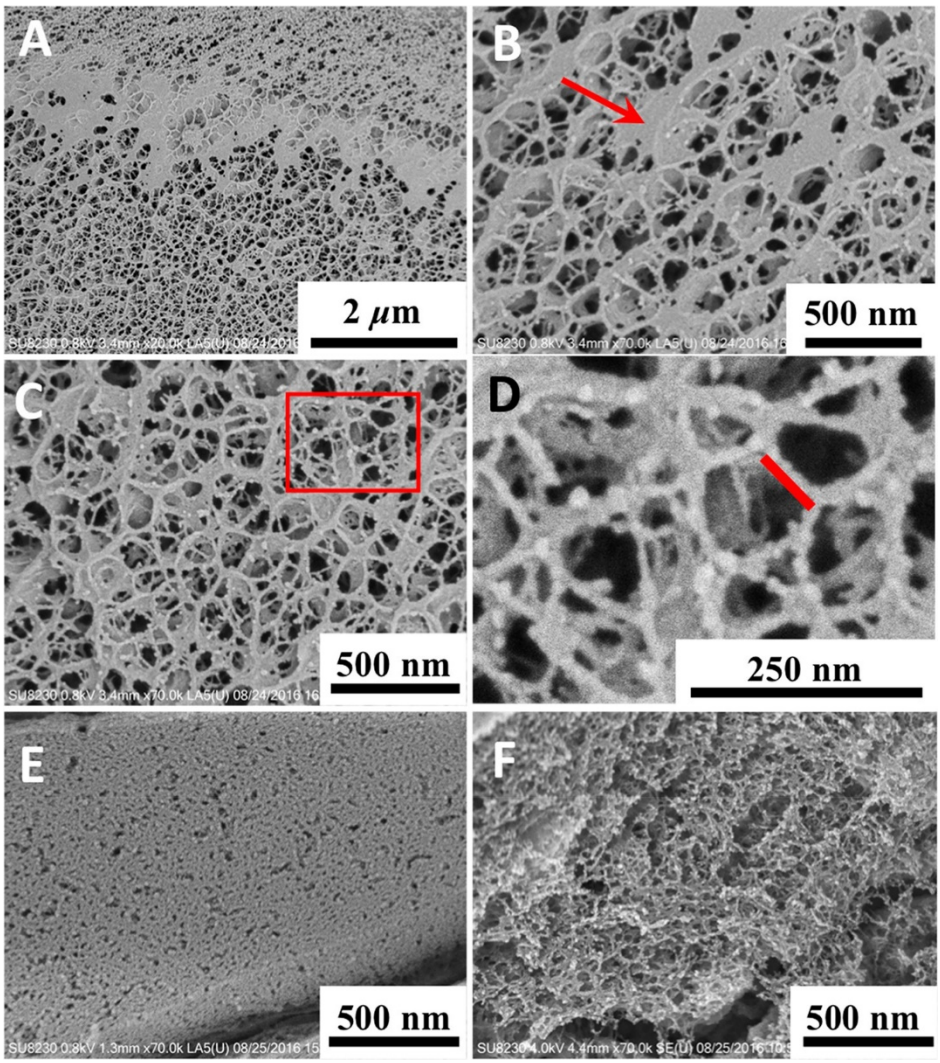

Figure 5.2- Cryo-SEM of frozen hydrated BSA hydrogels (A−D) and of BSA monomer solutions prior to polymerization (E), and a non-Cryo-SEM of a BSA hydrogel that was freeze-dried (F). Frozen hydrated BSA hydrogels are shown at 20K magnification (A); 70K magnification (B), red arrow points to vitreous ice remaining in the sample; 70K magnification (C), red box indicates the area that is enlarged in Figure 2D. (D) Enlarged area from Figure 2C where the thin BSA polymer strands are clearly visible. The red line highlights one of the measured protein polymer strand lengths. (E) Cryo-SEM of BSA monomer solutions before glutaraldehyde polymerization: 70K magnification. (F) Non-Cryo-SEM of freeze-dried BSA hydrogel: 70K magnification.

interconnected thin BSA polymer strands. The BSA polymer strand diameters were measured in areas where vitreous ice had mostly sublimated, as shown in Figure 5.2D.

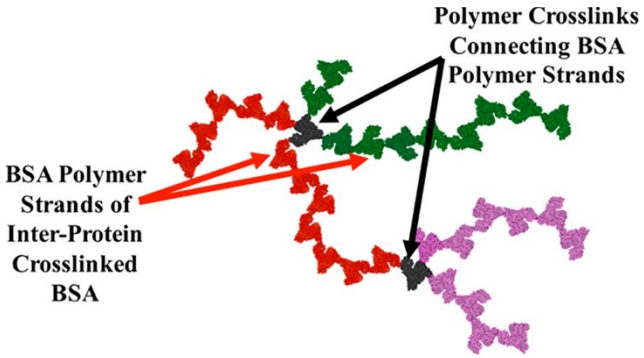

Figure 5.3- Proposed BSA hydrogel topology based on the Figure 5.2 Cryo-SEM images. Black arrows point to polymer cross-links, where aBSA forms interprotein cross-links that connect two polymer strands. Red arrows point to the different protein polymer strands that are colored red, green, and pink.

The BSA hydrogel is primarily composed of BSA polymer strands having diameters of ~15 ± 5 nm. These ~15 nm BSA polymer strand diameters are roughly the width of a single hydrated BSA protein monomer. X-ray diffraction measurements of BSA crystals determined that the BSA monomer has dimensions of ~4 × 6.5 × 7.5 nm^3.[61] We expect that the measured dimensions of a single BSA in our samples will be larger than the crystal structure dimensions due to its bound water layers and its Pt coating. Terahertz spectroscopy has shown that the water solvation shell can extend up to ~0.8−1.5 nm from the protein surface.[62,63] The 2.5 nm Pt sputter coating will also increase the dimensions of the hydrated BSA polymer strands. These measured BSA polymer strand diameters (Figure 5.2) are roughly similar to the expected dimension of a single, Pt coated, hydrated BSA protein.

From these high resolution Cryo-SEM images of hydrated BSA hydrogels, we can detect the polymerized BSA hydrogel topology,[64] i.e., how the BSA protein monomers are interconnected by the glutaraldehyde interprotein cross-linking to form the polymer network. The ~single BSA diameter of the protein polymer strands indicates that most of the globular proteins are bound together into roughly linear BSA chains, reminiscent of a pearl-necklace-like structure. Polymer

cross-links in the BSA hydrogel network are created by a protein that forms ≥3 interprotein cross-links that connect two or more of these BSA polymer strands, as illustrated in Figure 5.3.

We can approximate the molecular weight between cross- links in the BSA hydrogel network by estimating the number of proteins (MW: 66 463 g/mol BSA) in the polymer strands between polymer cross-links. The red line in Figure 2D highlights a measured polymer strand length. The BSA polymer strand lengths correspond to ∼5−30 BSA proteins; i.e., the molecular weight between cross-links in the BSA polymer network is between ∼3 × 105 and 2 × 106 g/mol.

The polymer cross-link density is the dominant factor determining the elastic free energy storage of the responsive BSA hydrogel.[23,65] Increasing the polymer cross-link density limits VPT swelling and shrinking. The cross-link density is inversely proportional to the average molecular weight between cross-links.

There are clear differences between the BSA hydrogel morphology (Figure 5.2A−D) and the morphology of the BSA monomer solution before glutaraldehyde polymerization (Figure 5.2E). Cryo-SEM images of the BSA monomer solution lack the characteristic interconnected polymer network observed for the BSA hydrogels. This difference between the glutaraldehyde polymerized BSA hydrogel and the BSA monomer solution confirms that predominantly interprotein cross-links are formed by the polymerization of 200 mg/mL BSA solutions at a glutaraldehyde/BSA protein ratio of 27.

Cryo-SEM is uniquely able to probe hydrated samples like hydrogels without significantly altering the protein polymer morphology.[56,57,66] In contrast, non-Cryo/traditional SEM techniques require sample drying prior to SEM imaging. Drying the hydrogel results in the collapse of the polymer network. It is much more difficult to observe and measure the individual polymer strands in non-Cryo-SEM images where BSA hydrogel samples are freeze-dried (Figure 5.2F). Freeze-

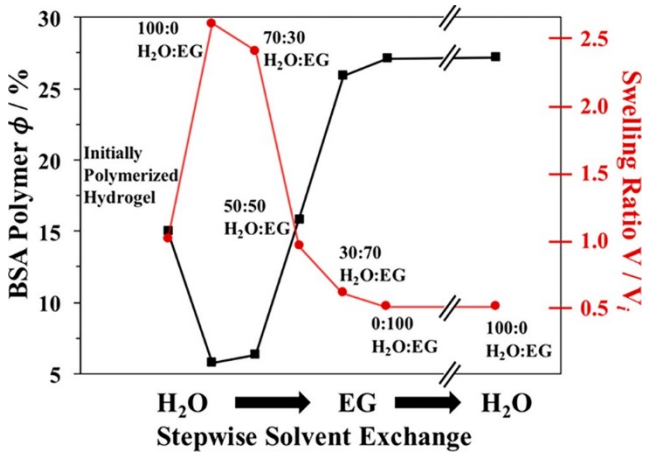

Figure 5.4- Dependence of the BSA polymer volume fraction, ϕ (left axis, black squares), and the swelling ratio, V/V_i (right axis, red circles), as a function of mobile phase composition during the stepwise water to EG exchange. The breaks in the graph illustrate thestepwise solvent exchange from pure EG back to pure water.

dried BSA hydrogel samples also appear to have smaller pores compared to those of the frozen hydrated samples (Figure 5.2A−D).

5.3.2 **EG Solvent Exchange Causes Irreversible VPT**

The stepwise solvent exchange from water to EG transforms responsive BSA hydrogels into responsive BSA organogels that sense protein−ligand binding in the pure organic solvent environment.[39] This EG exchange causes a large VPT that decreases the organogel volume. This VPT is irreversible with respect to the mobile phase composition. Attempting to rehydrate the BSA organogel by reversing the stepwise solvent exchange back to water does not cause organogel swelling. The volume swelling ratios, V/V0 (red circles), and the resulting BSA polymer volume fractions, φ (black squares), are shown in Figure 4, beginning with the initial BSA hydrogel directly after glutaraldehyde polymerization (φ = 15 vol %), and for each subsequent solvent exchange step in the hydrogel to organogel transformation.

The BSA hydrogel initially swells when incubated in water after polymerization until the system comes to equilibrium:$\Pi = \frac{\partial \Delta G\text{total}}{\delta V} = 0$. BSA hydrogel swelling in nanopure water decreases the BSA polymer volume fraction from φ = 15 vol % to φ = 6 vol % BSA.

The hydrogel then shrinks as the concentration of EG in the mobile phase increases. The final organogel volume equilibrated in pure EG is roughly half that of the initially fabricated hydrogel. This produces an organogel where the BSA polymer volume fraction is φ = 27 vol %.

Rehydrating the organogel by exchanging the EG mobile phase back to water does not cause organogel swelling. The BSA organogel does not reswell after incubating in water for over 7 days, nor does it swell when the solution is mildly heated to 45 °C. This temperature is below the 57 °C temperature that induces BSA conformational changes.67 Above 57 °C, swelling may result from protein unfolding. The BSA polymer volume fraction of these water incubated BSA organogels is equal to that of the BSA organogel in EG, φ= 27 vol % BSA.

Flory polymer solution theory is often used to describe the VPT phenomenon,[23] which describes the VPT in terms of osmotic pressures in the system that drive the volume change. These osmotic pressures derive from Gibbs free energy changes in the polymer−mobile phase system. The change in the total Gibbs free energy, ΔGtotal, has contributions from free energy of mixing changes, ΔGmix, elastic free energy changes, ΔGel, and ionic free energy changes, ΔGion.[21,68] Changes in the mobile phase composition often induce ΔGmix. Typically, ΔGel and ΔGion are expected to be small for a simple solvent exchange.

The VPT that results in a dramatic decrease in volume suggests that phase separation of the BSA polymer and mobile phase occurs during the water to EG exchange. The irreversibility very generally indicates that there is a hysteresis in the total Gibbs free energy between the BSA

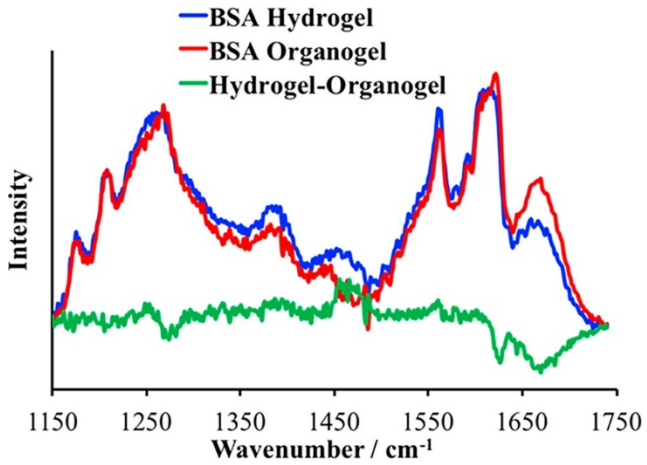

Figure 5.5- UVRR spectra of BSA hydrogel (blue), BSA organogel (red), and BSA hydrogel−organogel difference spectrum (green). The broad AmIII[3] band at ~1240−1270 cm^{-1} results from the distribution of peptide backbone Ψ angles used to calculate the protein secondary structure. Spectral differences at ~1460 cm^{-1} result from the subtraction of an intense EG Raman peak in the BSA organogel.

hydrogel and water incubated BSA organogel. The mechanisms of this phase separation and the origin of this irreversible VPT are discussed below.

5.3.3 **BSA Hydrogel, Organogel, and Water Incubated Organogel Secondary Structures**

The secondary structures of BSA hydrogels, organogels, and water incubated organogels were investigated using UV Resonance Raman (UVRR) spectroscopy. UVRR spectroscopy is a powerful tool for investigating the hydrogen bonding,[69,70] solvation environ- ment,[71,72] and secondary structure[47,73,74] in proteins.[75,76]

UVRR measurements were performed with an excitation wavelength of ~204 nm that is in resonance with the secondary amide $\pi \rightarrow \pi^*$ transitions of the polypeptide backbone.[76] This enhances the Raman scattering of vibrations that couple to the backbone amide electronic transitions.[76]

The UVRR enhanced amide III3 band frequency is highly sensitive to the Ramachandran Ψ torsion angles of the peptide backbone, enabling quantitative analysis of the protein secondary structure.[47,74] The AmIII3 band, found in the ∼1200−1300 cm^{-1} spectral region, consists primarily of C−N stretching and NH bending of the peptide bond.[76] The frequency of the AmIII3s band sinusoidally depends on the Ramachandran Ψ torsion angle of the peptide bond.[47,74] Mikhonin et al. developed equations to calculate the Ramachandran Ψ angles from the measured AmIII3s frequencies.[47]

The distribution of secondary structure populations in proteins gives rise to a particular set of Ψ angles. The secondary structure distribution inhomogeneously broadens the AmIII3 band. The secondary structures in our BSA proteins are determined from the broadened AmIII3 Raman bands. The AmIII3 band shape is fitted to a series of Lorentzians whose sum fits the AmIII3 Raman band shapes. Each Lorentzian band correlates to a particular Ψ angle frequency. The details of the calculated distribution of protein secondary structures in the BSA hydrogels, organogels, and water incubated organogels are provided in Appendix B.

We reproduced UVRR measurements of the BSA hydrogel and BSA monomers in aqueous solution. The reproduced UVRR spectra, shown in Figure B.2, agree with previous measurements.[3] The AmIII3 band shapes of the polymerized BSA hydrogel and BSA monomer are essentially identical, indicating that the protein secondary structure is not perturbed by the glutaraldehyde interprotein cross-linking that forms the BSA polymer network.

In both the BSA monomer and the BSA hydrogel, the fit of the AmIII3 band shape produces a dominant Lorentzian band at ∼1263 cm^{-1}; this AmIII s frequency correlates to a Ψ angle of ∼−47°.[47,74] This Ψ angle derives from an α-helical secondary structure. The area under the Lorentzian band at 1263 cm^{-1} accounts for ∼65% of the total $AmIII_3$ bandintensity, indicating

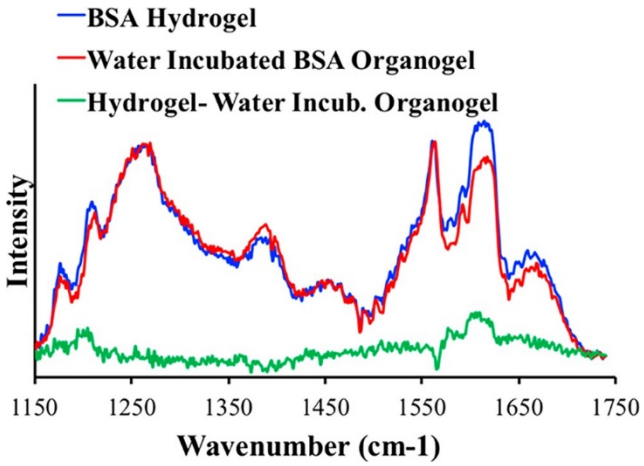

Figure 5.6- UVRR spectra of (blue) BSA hydrogel, (red) BSA organogel incubated in water, and (green) BSA hydrogel−water organogel incubated in water difference spectrum.

that BSA is predominantly α-helical. Other investigations on native BSA monomers also found the BSA secondary structure to be ~67% α-helical.[77,78]

The BSA organogel $AmIII_3$ band is shifted to a higher frequency from that of the BSA hydrogel (Figure 5.5). The negative peak in the hydrogel−organogel difference spectrumat ~1265 cm^{-1} (green spectrum in Figure 5.5) highlights the differences in the two $AmIII_3$ bands. This indicates that the α- helix type $AmIII_3$ band has an increased intensity in the organogel compared to the hydrogel. The BSA proteins in theorganogel show a ~4% increase in α-helical secondary structures compared to that of the BSA hydrogels.

This result is consistent with previously reported data for immobilized albumins in the presence of EG.[79,80] For example, Wasacz et al. used IR/ATR spectroscopy to investigate the structure of human serum albumin (HSA) that was adsorbed onto a substrate in water, EG, and methanol.[79] They observedan increased intensity of the α-helix $AmIII_3$ band when HSA was exposed to EG. Organic mobile phases generally decrease the solvent's ability to compete for hydrogen bonds compared to water. As a result, the proteins form more intrapeptide hydrogen bonding which increases the propensity for α-helix and β-sheet secondary structure formation.

The UVRR spectra of water incubated BSA organogels reveal that the ~4% increase in the BSA organogel α-helical conformations is reversible when EG is exchanged back to water. The AmIII3 band for the water incubated organogel is essentially identical to that of the BSA hydrogel (Figure 5.6), indicating that the BSA hydrogel and water incubated organogel have similar secondary structures.

The EG appears to be completely washed out of the organogel during the EG to water exchange. The intense EG Raman peak at ~1460 cm^{-1} in the UVRR BSA organogel spectrum does not appear in the water incubated BSA organogel spectrum.

We also examined the frequency of the AmI band of the BSA hydrogel, BSA organogel, and rehydrated BSA organogel. The AmI band in the ~1650−1700 cm^{-1} spectral region consists predominantly of the C=O stretching motion of the peptide backbone.[76] The BSA hydrogel, BSA organogel, and water incubated BSA organogel all have AmI bands at about 1665 cm^{-1}. The constant AmI band frequency in the BSA hydrogel and organogel spectra indicates that the hydrogen bonding and dielectric environments of the protein backbone amides are similar for the polymerized BSA proteins in the water and EG mobile phases.[69,70,75] This is unexpected since the dielectric constant of EG is significantly lower than that of water. This frequency would shift if the lower dielectric EG mobile phase caused disruptions to the H-bonding environment of the peptide backbone. AmI band frequency shifts in FT-IR spectrahave been observed for HSA when bound water layers are stripped from the protein surface by the addition of EG.[80]

5.3.4 **Water Content in BSA Organogels**

NIR absorption spectroscopy was used to measure the water content in our BSA organogels to elucidate the microenvironment around the proteins of the organogel. Water strongly absorbs

between 1900 and 1950 nm, whereas the EG has minimal absorption at these wavelengths.[81] The Supporting Information includes the 1400−2000 nm NIR absorbance of BSA organogels, the absorbance of EG−water mixtures, and the dependence of the 1915 nm absorbance as a function of water concentration.

Details on the calculations of the water molar absorptivity at 1915 nm, the water concentration in bulk EG, and the calculation of the water concentration in our BSA organogels are also included in the Supporting Information.

The BSA organogels are in equilibrium with an EG mobile phase that contains ~0.08 M water. The 1400−2000 nm NIR absorbance spectra of the BSA organogel films are shown in Figure S5 in the Supporting Information. The strong absorption around 1900 nm stems from water that is partitioned into the organogel films. From these absorbance measurements, we calculate that the maximum BSA organogel water concentration is 8.0 ± 0.2 M.

To account for the small EG absorbance contributions to the total organogel absorbance, the absorbance of a 420 and 820 μm thick pure EG film was subtracted from the total BSA organogel absorbance. This subtraction overestimates the EG absorption since the EG content in the organogel is less than that of a pure EG film. The minimum BSA organogel water concentration is calculated using this EG subtracted absorbance. Our BSA organogels contain at least 6.5 ± 0.2 M water. We assume that the increased water content in the BSA organogels relative to the bulk EG mobile phase stems from solvation shell waters that are bound to the polymerized BSA proteins.

These BSA organogel water concentrations correspond to 1182−1475 water molecules per BSA protein. Small-angle neutron scattering experiments and theoretical calculations of a single water layer based on the BSA surface area have shown that the first solvation shell of BSA contains

~1070 water molecules.[63,82] Terahertz spectroscopy studies of albumin proteins in aqueous solutions found that the bound solvation shell waters, which have slower water relaxation times relative to bulk water, can extend ~0.85 nm63 to ~1.5 nm62 from the protein surface. Shiraga et al. estimated that the ~0.85 nm solvation shell contains ~3400 waters per BSA (3−4 hydration layers).[63]

The polymerized BSA proteins in pure EG retain more than one hydration layer. The 1182−1475 waters per BSA calculated in our BSA organogels correspond to 1.1−1.4 solvation

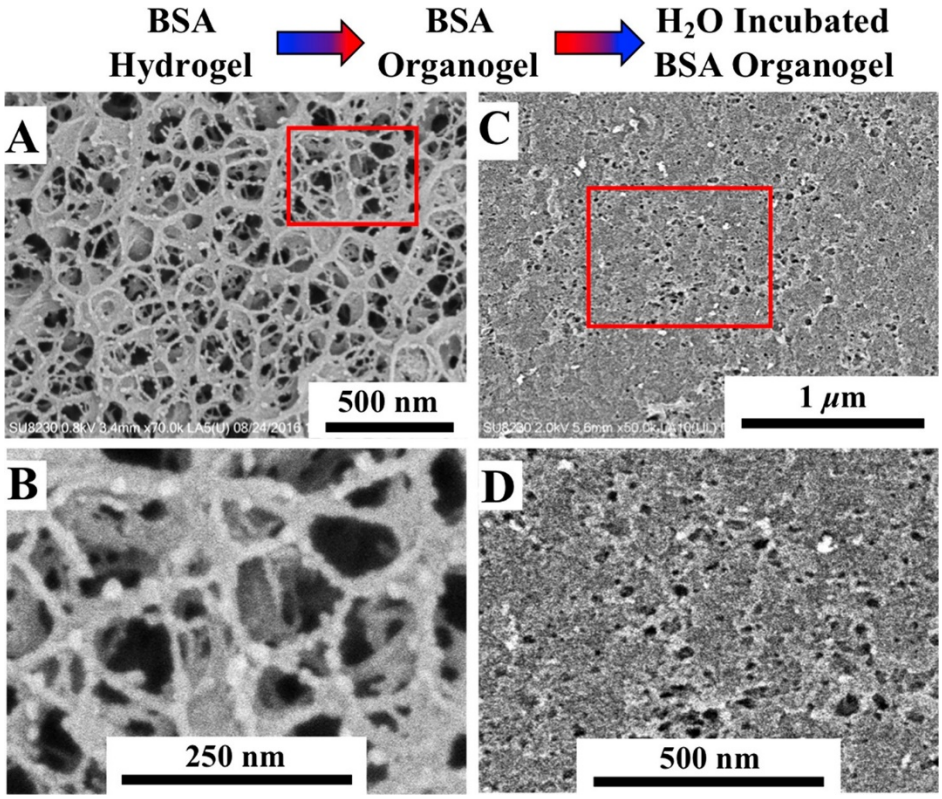

Figure 5.7- Cryo-SEM images comparing the morphology of BSA hydrogels (A, B) to that of the water incubated BSA organogels (C, D) after 40 min of sublimation and the application of a 2.5 nm Pt sputter coat. (A) BSA hydrogel; 70K magnification. (B) Enlarged area of BSA hydrogel, indicated by the red box in Figure 5.7A. (C) Water incubated BSA organogel; 50K magnification. (D) Enlarged area of water incubated BSA organogel, indicated by the red box in Figure 5.7C.

shells. The retained BSA solvation shell waters most likely account for the constant UVRR AmI frequency measured in the BSA hydrogels and organogels.

This protein hydration layer is important for protein folding and the dynamics necessary for protein ligand binding and catalysis.83−86 For example, it has been experimentally observed that there is a critical hydration level required for enzymatic activity (∼a single monolayer of water).[63,83,86] Our pure protein organogel sensors and catalysts[39] retain much of their native protein activity in EG, at least in part, due to the retained hydration layers. A discussion on the retained protein hydration shell of BSA organogels is provided in Appendix B.

5.3.5 **Water Incubated BSA Organogel Morphology**

Only the water incubated BSA organogels could be investigated using Cryo-SEM. The BSA organogels could not be imaged because the EG mobile phase could not be sublimed from the BSA polymer structure. We hypothesize that the BSA organogel and water incubated BSA organogel morphologies are roughly similar. The irreversibility of the VPT indicates that the largest polymer morphology changes occur during the water to EG exchange. We believe that additional significant morphology changes during the solvent exchange back to water are unlikely.

The mobile phase exchange induces significant irreversible changes in the morphology of the BSA polymer network. As a result, there is an obvious difference between the BSA protein polymer network structure observed in Cryo-SEM images of the water incubated BSA organogel (Figure 5.7C,D) compared to that of the BSA hydrogel (Figure 5.7A,B). The water to EG exchange changes the BSA polymer morphology from an interconnected network of thin BSA polymer strands to a dense amorphous BSA polymer phase in the water incubated BSA organogel. This is

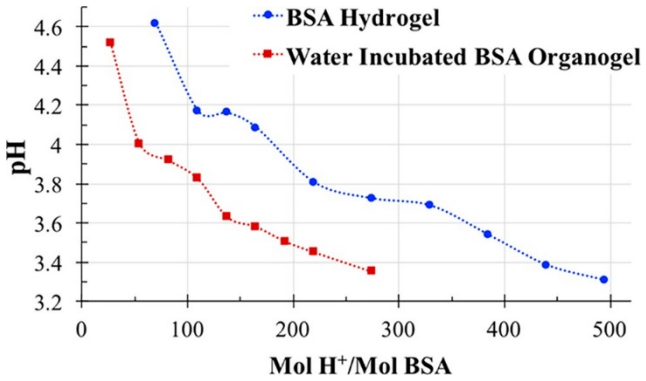

Figure 5.8- Titration curve of the BSA hydrogel before the water to EGexchange (blue), and the water incubated BSA organogel after the water to EG exchange and EG to water exchange (red). The titrationis normalized to the number of moles of H^+ added to solution per mole of BSA in the sample.

accompanied by a decrease in the polymer pore diameters compared to that of the BSA hydrogel. The water incubated BSA organogel pore diameters range from ~5 to ~30 nm.

We could not resolve the individual BSA polymer strands in the dense amorphous BSA polymer phase. Thus, thetopological properties of the organogel network, such as the number of interprotein cross-linked BSA in the protein polymer chains between polymer cross-links, cannot be estimated in the water incubated organogels, as we did forthe BSA hydrogels. Thus, changes in the BSA polymer cross- link density cannot be determined from these Cryo-SEM images.

From titration studies, we found that these morphology changes are accompanied by a decrease in the BSA polymer surface area that is accessible to the mobile phase. The changein the mobile phase exposed BSA polymer surface area was examined by titrating the pH sensitive amino acid carboxyl groups in the BSA hydrogels and in the water incubatedorganogels.

BSA contains 39 aspartic acid residues (pK_a 3.71) and 59 glutamic acid residues (pK_a 4.15).[61] The H^+ concentrationrequired to titrate aqueous solutions containing BSA hydrogelsor water incubated organogels from pH 6 to pH ~ 3.35 is directly proportional to the number of BSA carboxyl groups protonated. Only mobile phase accessible carboxyl groups onthe BSA polymer

surface are titratable. Carboxyl groups buried by the BSA polymer morphology change are not titrated because mobile phase diffusion to the buried polymer surface area is significantly slowed.

As shown in Figure 5.8, the water incubated BSA organogel titration curve is shifted to lower acid concentrations relative to that of the BSA hydrogel. The titration curves of the hydrogels and water incubated organogels can be directly compared because the titration is normalized to the number of moles of H+ added per mole of BSA in the hydrogel or water incubated organogel.

The water incubated BSA organogels require ~2-fold less acid to protonate all titratable aspartic and glutamic acid residues compared to that of the BSA hydrogels. These titration results directly demonstrate that the VPT phase separation irreversibly changes the BSA polymer surface area exposed to the mobile phase. The VPT renders about half the polymer surface area inaccessible to the mobile phase.

It should also be noted that formation of amino acid side chain interactions may also occur during the phase separation and could contribute to the decrease in titratable carboxyl groups. Interactions between carboxylates and other amino acids may decrease the effective pKa of those carboxylates. For example, salt bridges could form between the carboxylates and positively charged amino acids to stabilize the charged species.

5.3.6 **Mechanism of Irreversible VPT Caused by EG Exchange**

From these results, we are able to make certain conclusions on the mechanisms that actuate the VPT during the water to EG exchange. The large VPT that decreases the BSA organogel volume as a result of the EG exchange suggests that phase separation of the BSA polymer from the EG mobile phase occurs which induces a collapse of the polymer network. This BSA polymer phase separation is primarily driven by free energy of mixing changes, ΔG_{mix}. The UVRR

experiments clearly demonstrate that the BSA secondary structure does not significantly change between the hydrogel and organogel. During fabrication of the BSA hydrogel, the proteins are immobilized by the glutaraldehyde cross-linking.[43] Protein immobilization stabilizes the native protein conformation, which inhibits protein denaturation by the introduced organic solvent mobile

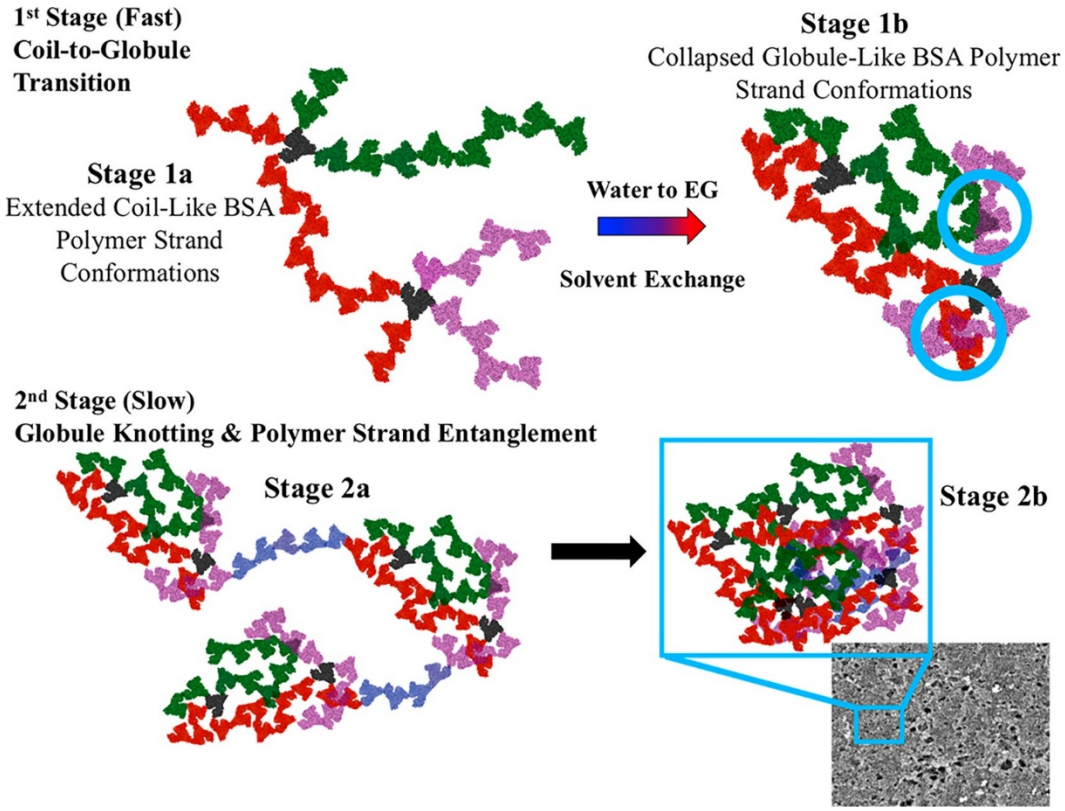

Figure 5.9- Illustration of the proposed kinetic two-stage phase separation of the BSA polymer that occurs during the water to EG exchange. The first stage (1a−1b) involves a fast coil-to-globule transition of the BSA polymer strands. This coil-to-globule transition decreases the distance between BSA polymer strands. Polymerized BSA on different protein polymer strands can form interprotein interactions where the BSA polymer strands are in close proximity, highlighted by the blue circles in stage 1b. These additional interprotein polymer strand interactions formed during phase separation increase the polymer cross-link density through physical polymer cross-linking, thus, preventing organogel reswelling. The second slower stage (2a−2b) of the phase separation involves knotting of the localized globules in the network and entanglement of the BSA polymer strands. This second stage further increases the BSA polymer density, resulting in the very dense BSA polymer phase observed in the water incubated organogel Cryo-SEM.

phase.[36] It is important to eliminate the possibility of protein structural changes because protein conformational changes could contribute to the VPT phenomenon,[25] particularly if the induced conformational change exposes amino acid side chains buried in the native protein core.

The BSA polymer VPT that occurs during the EG exchange is not caused by protein conformational changes but rather is induced by an unfavorable change in ΔGmix, between the protein polymer and mobile phase as the concentration of EG increases. The hydrogel/organogel ΔGmix is primarily determined by the Flory−Huggins polymer−solvent interaction parameter, χ.[23,65] Polymers in a good solvent are highly swollen and have small χ values because polymer−solvent interactions are favorable. In contrast, polymers in a poor solvent have larger χ values, and contain little solvent because polymer−polymer interactions are more favorable than polymer−mobile phase interactions.[87] Flory theory predicts that when $\chi \geq 0.5$, phase separation of the polymer from the mobile phase will occur due to enthalpic and/or entropic penalties resulting from the poor solvent interacting with the polymer chains.[23,87] It is extremely difficult to parse out which entropic or enthalpic contribution dominates this phase separation process because the hydrogel and subsequent organogel have a highly complex system of interactions between the protein polymer and mobile phase. The proteins have polypeptide chains made up of a specific sequence of 20 possible amino acid (AA) residues that vary in their hydrophobic properties, charge state, and hydrogen bonding strength. This specific sequence of AA directs protein folding, leading to a protein conformation that exposes certain AA to the mobile phase and buries others in the core of the protein. Each AA in the protein will have different enthalpic and entropic contributions to the protein−mobile phase interactions depending on its chemical structure and depending on the neighboring amino acids.

The large swelling ratio of the BSA hydrogel in water indicates $\chi_{BSA-water} \ll 0.5$. The continuous decrease in BSA hydrogel volume that occurs upon EG exchange indicates that χ increases with increasing EG concentrations. When χ exceeds the critical value of 0.5, phase separation occurs. However, we cannot determine the EG concentration that initiates the phase separation from these existing data. A more careful investigation of the BSA hydrogel VPT generated with smaller incremental increases in the EG concentration is necessary. The critical EG concentration that induces phase separation could be determined through titration of the BSA polymer carboxyl groups after equilibration in each EG/water solution. A large decrease in the solvent accessible polymer surface area would elucidate the EG concentration at which phase separation occurs.

This mobile phase exchange induced phase separation causes a collapse of the water swollen 3D protein polymer network. During phase separation, the polymer attempts to minimize its free energy, thus initiating conformational changes in the polymer strands that minimize its surface area in contact with the mobile phase.[88]

Polymer phase separation in a poor solvent is thought to occur as a (at least) two-stage process: a fast polymer strand collapse that induces a coil-to-globule-like transition in the polymer strands, followed by a slower stage that involves knotting of those globules and entanglement of the polymer strands.[89–91] We postulate that the BSA hydrogel to organogel transformation via the exchange from water to EG generates a similar kinetic two-stage phase separation, resulting in the dense amorphous BSA polymer phase observed in the water incubated organogel Cryo-SEM images, as illustrated in Figure 5.9.

The first stage of the phase separation involves a coil-to-globule transition of the BSA polymer strands (Figure 5.9, stage 1a−1b). The thin BSA polymer strands in the water swollen

hydrogel have an extended coil-like conformation. These extended polymer strand conformations collapse into a globule-like conformation to minimize the polymer surface area in contact with the EG mobile phase. As depicted in Figure 5.9, stage 2a, this fast coil-to-globule transition creates localized high polymer density globules throughout the cross-linked network connected by stretched bridging BSA polymer strands.[90]

The coil-to-globule transition is followed by globule knotting, where these localized globules coalesce into a very high density BSA polymer phase.[89] Entanglement of the polymer strands within the dense BSA polymer phase also occurs in this second stage and increases over time.[92] This kinetic two-stage phase separation that occurs during the BSA hydrogel to organogel transformation results in the amorphous dense BSA polymer phase observed in the water incubated BSA organogel Cryo-SEM images (Figure 5.9, stage 2b).

The phase separation mechanisms of thermoresponsive polymers have extensively been studied, for linear poly(N-isopropylacrylamide),[87,93] polystyrene,[94] and poly(methyl methacrylate)[91] polymer chains in solution. The phase separation of cross-linked poly(N-isopropylacrylamide) hydro-gel networks has also been investigate in polymer micro-particles.[49] The rate of both stages of the phase separation is significantly slowed in a cross-linked polymer network due to the topological constraints compared to the linear polymer chains in solution.

The VPT induced by phase separation in synthetic organic polymers is typically reversible. Entanglement of the polymer strands slows globule swelling in a good solvent.[92] Hysteresis in the globule-to-coil transition of poly(N-isopropylacrylamide) polymers has been observed, where melting of the globule is slowed by physical entanglements formed in the globule state.[95]

In contrast, our BSA polymer system exhibits a completely irreversible VPT. Negligible polymer swelling was observed upon the exchange back to water for several weeks. We

hypothesize that this irreversible VPT phenomenon of the pure protein polymer is caused by the formation of additional physical or chemical cross-links in the phase separated BSA polymer. The initial coil-to-globule transition and subsequent globule knotting decrease the distances between BSA polymer strands in the network. This allows formation of interprotein interactions between BSA proteins on different polymer strands that can act as polymer cross-links, indicated by the blue circles in Figure 5.9, stage 1b.

Additional interprotein strand interactions may include the formation of salt bridges or hydrogen bonds between AA sidechains that act as physical polymer cross-links. Electrostatic and H-bonding interactions between AA side chains[100] are likely to form during the water to EG exchange because EG is less polar than water and is consequently a weaker H-bond acceptor/donor. Thus, the competitiveness of the solvent to H-bond with the AA side chains decreases when water is exchanged for EG such that the AA−AA interactions are enthalpically more favorable than AA−EG interactions. Chemical polymer cross-links could also form if dangling glutaraldehyde groups are present. Polymer strand entanglement could also create physical polymer cross-links in the BSA polymer network.

Thus, the elastic free energy of the BSA polymer network increases during the BSA hydrogel to organogel transition. The elastic free energy is an entropically derived restoring force that resists polymer strand conformational changes which are intrinsic to hydro-/organogel swelling or shrinking. Therefore, incubating the BSA organogel in water does not result in swelling due to a significant increase in the cross-link density of the BSA polymer network.

Finally, it must be noted that attempting to fabricate the BSA organogels using a single step solvent exchange where the BSA hydrogels are directly incubated in pure EG creates a material that is in a kinetically trapped state far from the thermodynamic equilibrium. The stepwise

solvent exchange to EG allows the BSA polymer network to homogeneously shrink with increasing EG concentration prior to the phase separation event, that we believe occurs at higher EG concentrations. This creates a material much closer to the thermodynamic equilibrium state.

An interfacial skin layer can form in hydrogels when exposed to drastic changes in solvent quality that cause a phase separation induced VPT.[96] Skin layer formation has been utilized for drug release applications, where the drug is not released from the hydrogel material until the VPT of the skin layer is reversed.[97] However, formation of a skin layer in our photonic crystal organogel sensing materials may confound the sensor response. The BSA organogels fabricated using the stepwise solvent exchange swell in response to BSA−ligand binding.[39] In contrast, the single step solvent exchanged BSA organogels shrink in response to the ligand binding (unpublished data). The magnitude of these volume changes varies in the kinetically trapped BSA organogels depending on the time the BSA hydrogel was equilibrated in pure EG prior to ligand addition. This results in an unreliable sensor response for the single step solvent exchanged BSA organogels.

5.4 Conclusions

Using UVRR and IR spectroscopy, Cryo-SEM, and physical measurements of the gel volume and concentration of titratable amino acids, we characterized changes to the BSA secondary structure and BSA polymer morphology that accompanies the stepwise solvent exchange to EG. The mobile phase exchange from water to EG transforms responsive BSA hydrogels into responsive BSA organogels. We determined the following:

(1) The BSA hydrogel is an interconnected network of thin BSA polymer strands with diameters roughly that of a single BSA protein. BSA hydrogel pores have diameters ranging

from 50 to 200 nm. The molecular weight between polymer cross-links was approximated from the polymer strand lengths, which equal ~5−30 BSA or ~3×10^5 − 2×10^6 g/mol.

(2) The solvent exchange from the water mobile phase of the hydrogel to the EG mobile phase of the organogel causes a VPT that increases the BSA polymer volume fraction from $\phi_{hydrogel}$ = 6% to $\phi_{organogel}$ = 27%. The VPT is irreversible; $\phi_{water\text{-}incubated\text{-}organogel}$ = 27% after exchanging the EG mobile phase back to water.

(3) There is a ~4% increase in the population of α-helix secondary structure in the BSA organogel compared to that of the BSA hydrogel and native BSA monomers. These secondary structure changes are reversible; the UVRR $AmIII_3$ bands of water incubated BSA organogels are identical to those of the BSA hydrogels.

(4) The water incubated organogel UVRR spectrum does not contain contributions from EG, indicating that the EG mobile phase is qualitatively removed during exchange back to water.

(5) The NIR absorbance of water in the BSA organogels demonstrate that there is a higher water content in the BSA organogels compared to the bulk EG mobile phase. There are roughly 1200−1500 water molecules per BSA protein in the organogel, meaning 1.1−1.4 hydrations layers remain bound to the proteins.

(6) Irreversible BSA polymer morphology changes occur during EG exchange. The water incubated BSA organogel morphology drastically differs from that of the BSA hydrogel. The water incubated organogel morphology is a dense amorphous polymer phase with significantly smaller pore diameters (5−30 nm) compared to the BSA hydrogel pore diameters (50− 200 nm).

(7) The hydrogel to organogel morphology change results in a decrease in the solvent exposed

surface area. There are approximately 50% fewer titratable amino acid carboxyl groups in the BSA organogel than in the BSA hydrogel.

We determined that a phase separation of the BSA polymer and mobile phase causes the VPT that accompanies the hydrogel to organogel transformation. This phase separation is driven by free energy of mixing changes where the Flory−Huggins interaction parameter increases with increasing EG concentrations. This phase separation proceeds in two stages, a fast coil-to-globule transition followed by globule knotting and BSA polymer strand entanglement, that results in a dense amorphous BSA polymer morphology. Additional interprotein strand interactions that are formed in the phase separated BSA polymer state are the most likely source of the irreversible VPT phenomenon. Physical or chemical polymer cross-links increase the polymer cross-link density. Thus, the elastic free energy increases, resisting BSA polymer swelling when the mobile phase is exchanged back to water.

The irreversible VPT phenomena of our BSA polymer is advantageous for our photonic crystal sensing motif where BSA organogels sense BSA−ligand binding through an organogel swelling response. EG is a hydroscopic organic solvent and absorbs water vapor proportional to the relative humidity of the air. Water absorption by EG in the BSA organogel does not impact the sensor response because the addition of water will not reswell the organogel. This is in contrast to our previously fabricated evaporation resistant sensing materials that contain an ionic liquid mobile phase[16] which undergo a VPT in response to humidity changes.

5.4.1 **Funding**

This work was funded by the Defense Threat Reduction Agency under grant HDTRA1-15-1-0038.

5.4.2 **Notes**

The authors declare no competing financial interest.

5.5 Acknowledgements

Cryo-SEM imaging was performed at the College of Science and Engineering Characterization Facility at the University of Minnesota. We appreciate the assistance of Chris Fretham and Hanseung Lee. Their expertise in Cryo-SEM imaging was critical in obtaining high resolution images of the protein polymer morphology.

5.6 References

(1) Elliott, J. E.; Macdonald, M.; Nie, J.; Bowman, C. N. Structure and Swelling of Poly (Acrylic Acid) Hydrogels: Effect of pH, Ionic Strength, and Dilution on the Crosslinked Polymer Structure. *Polymer* 2004, *45*, 1503−1510.

(2) Lee, Y.-J.; Pruzinsky, S. A.; Braun, P. V. Glucose-Sensitive Inverse Opal Hydrogels: Analysis of Optical Diffraction Response. *Langmuir* 2004, *20*, 3096−3106.

(3) Cai, Z.; Zhang, J.-T.; Xue, F.; Hong, Z.; Punihaole, D.; Asher, S. A. 2D Photonic Crystal Protein Hydrogel Coulometer for Sensing Serum Albumin Ligand Binding. *Anal. Chem.* 2014, *86*, 4840−4847.

(4) Cai, Z.; Smith, N. L.; Zhang, J.-T.; Asher, S. A. Two-Dimensional Photonic Crystal Chemical

and Biomolecular Sensors. *Anal. Chem.* 2015, *87*, 5013−5025.

(5) Cai, Z.; Kwak, D. H.; Punihaole, D.; Hong, Z.; Velankar, S. S.; Liu, X.; Asher, S. A. A Photonic Crystal Protein Hydrogel Sensor for Candida albicans. *Angew. Chem., Int. Ed.* 2015, *54*, 13036−13040.

(6) Lu, H. D.; Wheeldon, I. R.; Banta, S. Catalytic Biomaterials: Engineering Organophosphate Hydrolase to Form Self-Assembling Enzymatic Hydrogels. *Protein Eng., Des. Sel.* 2010, *23*, 559−566.

(7) Kim, Y. H.; Campbell, E.; Yu, J.; Minteer, S. D.; Banta, S. Complete Oxidation of Methanol in Biobattery Devices Using a Hydrogel Created from Three Modified Dehydrogenases. *Angew. Chem., Int. Ed.* 2013, *52*, 1437−1440.

(8) Hoffman, A. S. Hydrogels for Biomedical Applications. *Adv. Drug Delivery Rev.* 2012, *64*, 18−23.

(9) Baler, K.; Michael, R.; Szleifer, I.; Ameer, G. A. Albumin Hydrogels Formed by Electrostatically Triggered Self-Assembly and Their Drug Delivery Capability. *Biomacromolecules* 2014, *15*, 3625−3633.

(10) Leach, J. B.; Schmidt, C. E. Characterization of Protein Release from Photocrosslinkable Hyaluronic Acid-Polyethylene Glycol Hydrogel Tissue Engineering Scaffolds. *Biomaterials* 2005, *26*, 125− 135.

(11) Kamoun, E. A.; Kenawy, E.-R. S.; Chen, X. A Review on Polymeric Hydrogel Membranes for Wound Dressing Applications: PVA-Based Hydrogel Dressings. *J. Adv. Res.* 2017, *8*, 217−233.

(12) Idris, A.; Man, Z.; Maulud, A.; Khan, M. Effects of Phase Separation Behavior on Morphology and Performance of Polycar- bonate Membranes. *Membranes* 2017, *7*, 21−39.

(13) Gerlach, G., Arndt, K.-F., Eds. *Hydrogel Sensors and Actuators: Engineering and Technology*; Springer Series on Chemical Sensors and Biosensors Vol. 6; Springer-Verlag Berlin Heidelberg: Dresden, 2010.

(14) Asher, S. A.; Holtz, J.; Liu, L.; Wu, Z. Self-Assembly Motif for Creating Submicron Periodic Materials. Polymerized Crystalline Colloidal Arrays. *J. Am. Chem. Soc.* 1994, *116*, 4997−4998.

(15) Zhang, J.-T.; Wang, L.; Luo, J.; Tikhonov, A.; Kornienko, N.; Asher, S. A. 2-D Array Photonic Crystal Sensing Motif. *J. Am. Chem. Soc.* 2011, *133*, 9152−9155.

(16) Smith, N. L.; Hong, Z.; Asher, S. A. Responsive Ionic Liquid-Polymer 2D Photonic Crystal Gas Sensors. *Analyst (Cambridge, U. K.)* 2014, *139*, 6379−6386.

(17) Walker, J.; Kimble, K.; Asher, S. Photonic Crystal Sensor for Organophosphate Nerve Agents Utilizing the Organophosphorus Hydrolase Enzyme. *Anal. Bioanal. Chem.* 2007, *389*, 2115−2124.

(18) Walker, J. P.; Asher, S. A. Acetylcholinesterase-Based Organophosphate Nerve Agent Sensing Photonic Crystal. *Anal. Chem.* 2005, *77*, 1596−1600.

(19) Kamenjicki, M.; Lednev, I. K.; Asher, S. A. Photoresponsive Azobenzene Photonic Crystals. *J. Phys. Chem. B* 2004, *108*, 12637−12639.

(20) Sharma, A. C.; Jana, T.; Kesavamoorthy, R.; Shi, L.; Virji, M. A.; Finegold, D. N.; Asher, S. A. A General Photonic Crystal Sensing Motif: Creatinine in Bodily Fluids. *J. Am. Chem. Soc.* 2004, *126*, 2971−2977.

(21) Goponenko, A. V.; Asher, S. A. Modeling of Stimulated Hydrogel Volume Changes in Photonic Crystal Pb2+ Sensing Materials. *J. Am. Chem. Soc.* 2005, *127*, 10753−10759.

(22) Wu, C.; Zhou, S. Volume Phase Transition of Swollen Gels: Discontinuous or Continuous?

Macromolecules 1997, *30*, 574−576.

(23) Flory, P. J. *Principles of Polymer Chemistry*; Cornell University Press: Ithaca, NY, 1953.

(24) Hirotsu, S.; Hirokawa, Y.; Tanaka, T. Volume-Phase Transitions of Ionized N-Isopropylacrylamide Gels. *J. Chem. Phys.* 1987, *87*, 1392−1395.

(25) Cai, Z.; Luck, L. A.; Punihaole, D.; Madura, J. D.; Asher, S. A. Photonic Crystal Protein Hydrogel Sensor Materials Enabled by Conformationally Induced Volume Phase Transition. *Chem. Sci.* 2016, *7*, 4557−4562.

(26) Gao, X.; Lyu, S.; Li, H. Decorating a Blank Slate Protein Hydrogel: A General and Robust Approach for Functionalizing Protein Hydrogels. *Biomacromolecules* 2017, *18*, 3726−3732.

(27) Xu, X.; Xu, Z.; Yang, X.; He, Y.; Lin, R. Construction and Characterization of a Pure Protein Hydrogel for Drug Delivery Application. *Int. J. Biol. Macromol.* 2017, *95*, 294−298.

(28) Heck, T.; Faccio, G.; Richter, M.; Thöny-Meyer, L. Enzyme-Catalyzed Protein Crosslinking. *Appl. Microbiol. Biotechnol.* 2013, *97*, 461−475.

(29) de Vries, A.; Hendriks, J.; van der Linden, E.; Scholten, E. Protein Oleogels from Protein Hydrogels via a Stepwise Solvent Exchange Route. *Langmuir* 2015, *31*, 13850−13859.

(30) Scholten, E. Protein Oleogels: Network Formation of Proteins in Hydrophobic Conditions. In *Edible Oleogels*, 2nd ed.; Marangoni, A. G., Garti, N., Eds.; AOCS Press, 2018; Chapter 12, pp 285−305.

(31) Fjerbaek, L.; Christensen, K. V.; Norddahl, B. A Review of the Current State of Biodiesel Production using Enzymatic Trans- esterification. *Biotechnol. Bioeng.* 2009, *102*, 1298−1315.

(32) Carrea, G.; Riva, S. Properties and Synthetic Applications of Enzymes in Organic Solvents. *Angew. Chem., Int. Ed.* 2000, *39*, 2226−2254.

(33) Jacquet, P.; Daude, D.; Bzdrenga, J.; Masson, P.; Elias, M.; Chabriere, E. Current and

Emerging Strategies for Organophosphate Decontamination: Special Focus on Hyperstable Enzymes. *Environ. Sci. Pollut. Res.* 2016, *23*, 8200−8218.

(34) Yang, F.; Wild, J. R.; Russell, A. J. Nonaqueous Biocatalytic Degradation of a Nerve Gas Mimic. *Biotechnol. Prog.* 1995, *11*, 471− 474.

(35) Mattos, C.; Ringe, D. Proteins in Organic Solvents. *Curr. Opin. Struct. Biol.* 2001, *11*, 761−764.

(36) Stepankova, V.; Bidmanova, S.; Koudelakova, T.; Prokop, Z.; Chaloupkova, R.; Damborsky, J. Strategies for Stabilization of Enzymes in Organic Solvents. *ACS Catal.* 2013, *3*, 2823−2836.

(37) Iyer, P. V.; Ananthanarayan, L. Enzyme Stability and Stabilization Aqueous and Non-Aqueous Environment. *Process Biochem. (Oxford, U. K.)* 2008, *43*, 1019−1032.

(38) Zdarta, J.; Meyer, A.; Jesionowski, T.; Pinelo, M. A General Overview of Support Materials for Enzyme Immobilization: Characteristics, Properties, Practical Utility. *Catalysts* 2018, *8*, 92−119.

(39) Smith, N. L.; Coukouma, A. E.; Wilson, D. C.; Ho, B.; Gray, V.P.; Asher, S. A. Stimuli Responsive Pure Protein Organogel Sensors and Biocatalytic Materials. *ACS Appl. Mater. Interfaces* 2019, in press; DOI: 10.1021/acsami.9b18191.

(40) Cui, J. D.; Jia, S. R. Optimization Protocols and Improved Strategies of Cross-linked Enzyme Aggregates Technology: Current Development and Future Challenges. *Crit. Rev. Biotechnol.* 2015, *35*, 15−28.

(41) Lopez-Gallego, F.; Betancor, L.; Mateo, C.; Hidalgo, A.; Alonso-Morales, N.; Dellamora-Ortiz, G.; Guisan, J. M.; Fernandez- Lafuente, R. Enzyme Stabilization by Glutaraldehyde Crosslinking of Adsorbed Proteins on Aminated Supports. *J. Biotechnol.* 2005, *119*, 70−75.

(42) Kartal, F.; Janssen, M. H. A.; Hollmann, F.; Sheldon, R. A.; Kılınc, A. Improved Esterification Activity of Candida Rugosa Lipase in Organic Solvent by Immobilization as Cross-linked Enzyme Aggregates (CLEAs). *J. Mol. Catal. B: Enzym.* 2011, *71*, 85−89.

(43) Sheldon, R. A.; Schoevaart, R.; Van Langen, L. M. Cross-linked Enzyme Aggregates (CLEAs): A Novel and Versatile Method for Enzyme Immobilization (a review). *Biocatal. Biotransform.* 2005, *23*, 141−147.

(44) Homaei, A. A.; Sariri, R.; Vianello, F.; Stevanato, R. Enzyme Immobilization: An Update. *J. Chem. Biol.* 2013, *6*, 185−205.

(45) Curry, S.; Brick, P.; Franks, N. P. Fatty Acid Binding to Human Serum Albumin: New Insights from Crystallographic Studies. *Biochim. Biophys. Acta, Mol. Cell Biol. Lipids* 1999, *1441*, 131−140.

(46) Evoli, S.; Mobley, D. L.; Guzzi, R.; Rizzuti, B. Multiple Binding Modes of Ibuprofen in Human Serum Albumin Identified by Absolute Binding Free Energy Calculations. *Phys. Chem. Chem. Phys.* 2016, *18*, 32358−32368.

(47) Mikhonin, A. V.; Bykov, S. V.; Myshakina, N. S.; Asher, S. A. Peptide Secondary Structure Folding Reaction Coordinate: Correla- tion between UV Raman Amide III Frequency, Ψ Ramachandran Angle, and Hydrogen Bonding. *J. Phys. Chem. B* 2006, *110*, 1928− 1943.

(48) Wu, T.-Y.; Zrimsek, A. B.; Bykov, S. V.; Jakubek, R. S.; Asher, S. A. Hydrophobic Collapse Initiates the Poly(N-isopropylacrylamide) Volume Phase Transition Reaction Coordinate. *J. Phys. Chem. B* 2018, *122*, 3008−3014.

(49) Wu, C. A Comparison Between the ′Coil-to-Globule' Transition of Linear Chains and the 'Volume Phase Transition' of Spherical Microgels. *Polymer* 1998, *39*, 4609−4619.

(50) Erickson, H. P. Size and Shape of Protein Molecules at the Nanometer Level Determined

by Sedimentation, Gel Filtration, and Electron Microscopy. *Biol. Proced. Online* 2009, *11*, 32−51.

(51) Bykov, S.; Lednev, I.; Ianoul, A.; Mikhonin, A.; Munro, C.; Asher, S. A. Steady-State and Transient Ultraviolet Resonance Raman Spectrometer for the 193−270 nm Spectral Region. *Appl. Spectrosc.* 2005, *59*, 1541−1552.

(52) Heuser, J. E. The Origins and Evolution of Freeze-Etch Electron Microscopy. *Microscopy* 2011, *60*, S3−S29.

(53) Schneider, C. A.; Rasband, W. S.; Eliceiri, K. W. NIH Image to ImageJ: 25 years of Image Analysis. *Nat. Methods* 2012, *9*, 671.

(54) Migneault, I.; Dartiguenave, C.; Bertrand, M. J.; Waldron, K. C. Glutaraldehyde: Behavior in Aqueous Solution, Reaction with Proteins, and Application to Enzyme Crosslinking. *BioTechniques* 2004, *37*, 790−802.

(55) Huang, B. X.; Kim, H.-Y.; Dass, C. Probing Three-Dimensional Structure of Bovine Serum Albumin by Chemical Cross-linking and Mass Spectrometry. *J. Am. Soc. Mass Spectrom.* 2004, *15* (8), 1237−1247.

(56) Apkarian, R. P.; Wright, E. R.; Seredyuk, V. A.; Eustis, S.; Lyon, L. A.; Conticello, V. P.; Menger, F. M. In-Lens Cryo-High Resolution Scanning Electron Microscopy: Methodologies for Molecular Imaging of Self-Assembled Organic Hydrogels. *Microsc. Microanal.* 2003, *9*, 286−295.

(57) Wright, E. R.; Conticello, V. P.; Apkarian, R. P. Morphological Characterization of Elastin-Mimetic Block Copolymers Utilizing Cryo- and Cryoetch-HRSEM. *Microsc. Microanal.* 2003, *9*, 171−182.

(58) Vezie, D. L.; Thomas, E. L.; Adams, W. W. Low-Voltage, High-Resolution Scanning Electron Microscopy: A New Characterization Technique for Polymer Morphology. *Polymer*

1995, *36*, 1761−1779.

(59) Guo, Q. *Polymer Morphology: Principles, Characterization, and Processing*; John Wiley & Sons, Incorporated: New York, 2016.

(60) Lou, X.; Munro, S.; Wang, S. Drug Release Characteristics of Phase Separation pHEMA Sponge Materials. *Biomaterials* 2004, *25*,5071−5080.

(61) Majorek, K. A.; Porebski, P. J.; Dayal, A.; Zimmerman, M. D.; Jablonska, K.; Stewart, A. J.; Chruszcz, M.; Minor, W. Structural and Immunologic Characterization of Bovine, Horse, and Rabbit Serum Albumins. *Mol. Immunol.* 2012, *52*, 174−182.

(62) Bye, J. W.; Meliga, S.; Ferachou, D.; Cinque, G.; Zeitler, J. A.; Falconer, R. J. Analysis of the Hydration Water around Bovine Serum Albumin Using Terahertz Coherent Synchrotron Radiation. *J. Phys. Chem. A* 2014, *118*, 83−88.

(63) Shiraga, K.; Ogawa, Y.; Kondo, N. Hydrogen Bond Network of Water around Protein Investigated with Terahertz and Infrared Spectroscopy. *Biophys. J.* 2016, *111*, 2629−2641.

(64) Gu, Y.; Zhao, J.; Johnson, J. A. A (Macro)Molecular-Level Understanding of Polymer Network Topology. *Trends Chem.* 2019, *1*, 318−334.

(65) White, E. M.; Yatvin, J.; Grubbs, J. B., III; Bilbrey, J. A.; Locklin, J. Advances in Smart Materials: Stimuli-Responsive Hydrogel ThinFilms. *J. Polym. Sci., Part B: Polym. Phys.* 2013, *51*, 1084−1099.

(66) Marmorat, C.; Arinstein, A.; Koifman, N.; Talmon, Y.; Zussman, E.; Rafailovich, M. Cryo-Imaging of Hydrogels Super-molecular Structure. *Sci. Rep.* 2016, *6*, 25495.

(67) Murayama, K.; Tomida, M. Heat-Induced Secondary Structureand Conformation Change of Bovine Serum Albumin Investigated by Fourier Transform Infrared Spectroscopy. *Biochemistry* 2004, *43*, 11526−11532.

(68) Tanaka, T.; Fillmore, D.; Sun, S.-T.; Nishio, I.; Swislow, G.; Shah, A. Phase Transitions in Ionic Gels. *Phys. Rev. Lett.* 1980, *45*,1636−1639.

(69) Punihaole, D.; Jakubek, R. S.; Workman, R. J.; Asher, S. A. Interaction Enthalpy of Side Chain and Backbone Amides in Polyglutamine Solution Monomers and Fibrils. *J. Phys. Chem. Lett.* 2018, *9*, 1944−1950.

(70) Wang, Y.; Purrello, R.; Georgiou, S.; Spiro, T. G. UVRR Spectroscopy of the Peptide Bond. 2. Carbonyl H-Bond Effects on the Ground- and Excited-State Structures of N-Methylacetamide. *J. Am. Chem. Soc.* 1991, *113*, 6368−6377.

(71) Jakubek, R. S.; White, S. E.; Asher, S. A. UV Resonance Raman Structural Characterization of an (In)soluble Polyglutamine Peptide. *J. Phys. Chem. B* 2019, *123*, 1749−1763.

(72) Punihaole, D.; Jakubek, R. S.; Dahlburg, E. M.; Hong, Z.; Myshakina, N. S.; Geib, S.; Asher, S. A. UV Resonance Raman Investigation of the Aqueous Solvation Dependence of Primary Amide Vibrations. *J. Phys. Chem. B* 2015, *119*, 3931−3939.

(73) Jakubek, R. S.; Workman, R. J.; White, S. E.; Asher, S. A. Polyglutamine Solution-State Structural Propensity Is Repeat Length Dependent. *J. Phys. Chem. B* 2019, *123*, 4193−4203.

(74) Asher, S. A.; Ianoul, A.; Mix, G.; Boyden, M. N.; Karnoup, A.; Diem, M.; Schweitzer-Stenner, R. Dihedral ψ Angle Dependence of the Amide III Vibration: A Uniquely Sensitive UV Resonance Raman Secondary Structural Probe. *J. Am. Chem. Soc.* 2001, *123*, 11775− 11781.

(75) Jakubek, R. S.; Handen, J.; White, S. E.; Asher, S. A.; Lednev, I. K. Ultraviolet Resonance Raman Spectroscopic Markers for Protein Structure and Dynamics. *TrAC, Trends Anal. Chem.* 2018, *103*, 223− 229.

(76) Oladepo, S. A.; Xiong, K.; Hong, Z.; Asher, S. A.; Handen, J.; Lednev, I. K. UV Resonance Raman Investigations of Peptide and Protein Structure and Dynamics. *Chem. Rev.* 2012, *112*,

2604−2628.

(77) Takeda, K.; Shigeta, M.; Aoki, K. Secondary Structures of Bovine Serum Albumin in Anionic and Cationic Surfactant Solutions. *J. Colloid Interface Sci.* 1987, *117*, 120−126.

(78) Moriyama, Y.; Watanabe, E.; Kobayashi, K.; Harano, H.; Inui, E.; Takeda, K. Secondary Structural Change of Bovine Serum Albumin in Thermal Denaturation up to 130 °C and Protective Effectof Sodium Dodecyl Sulfate on the Change. *J. Phys. Chem. B* 2008, *112*, 16585−16589.

(79) Wasacz, F. M.; Olinger, J. M.; Jakobsen, R. J. Fourier Transform Infrared Studies of Proteins using Nonaqueous Solvents. Effects of Methanol and Ethylene Glycol on Albumin and Immunoglobulin G.*Biochemistry* 1987, *26*, 1464−1470.

(80) Jakobsen, R. J.; Wasacz, F. M.; Brasch, J. W.; Smith, K. B. The Relationship of Bound Water to the IR Amide I Bandwidth ofAlbumin. *Biopolymers* 1986, *25*, 639−654.

(81) GuidedWave, An Introduction to Online NIR Water Measurements in Liquid Samples. AZO Mater. [Online], Jan. 25, 2019. https://www.azom.com/article.aspx?ArticleID=17511 (accessed May 27, 2019).

(82) Rejou-Michel, A.; Henry, F.; Villardi, M. d.; Delmotte, M. Protein and Ion Hydration Variation in Fixed Aqueous Solutions: Measurement by Dielectric Decrement. *Phys. Med. Biol.* 1985, *30*, 831−837.

(83) Rupley, J. A.; Careri, G. Protein Hydration and Function. In *Advances in Protein Chemistry*; An*f*insen, C. B., Richards, F. M., Edsall, J. T., Eisenberg, D. S., Eds.; Academic Press, 1991; Vol. *41*, pp 37− 172.

(84) Schmitke, J. L.; Wescott, C. R.; Klibanov, A. M. The Mechanistic Dissection of the Plunge in Enzymatic Activity upon Transition from Water to Anhydrous Solvents. *J. Am. Chem. Soc.* 1996, *118*, 3360−3365.

(85) Laage, D.; Elsaesser, T.; Hynes, J. T. Water Dynamics in the Hydration Shells of Biomolecules. *Chem. Rev.* 2017, *117*, 10694− 10725.

(86) Brovchenko, I.; Oleinikova, A. Which Properties of a SpanningNetwork of Hydration Water Enable Biological Functions? *Chem- PhysChem* 2008, *9*, 2695−2702.

(87) Wang, R.; Wang, Z.-G. Theory of Polymer Chains in Poor Solvent: Single-Chain Structure, Solution Thermodynamics, and Θ Point. *Macromolecules* 2014, *47*, 4094−4102.

(88) Raos, G.; Allegra, G. Chain Collapse and Phase Separation in Poor-Solvent Polymer Solutions: A Unified Molecular Description. *J. Chem. Phys.* 1996, *104*, 1626−1645.

(89) Grosberg, A. Y.; Kuznetsov, D. V. Single-Chain Collapse or Precipitation? Kinetic Diagram of the States of a Polymer Solution. *Macromolecules* 1993, *26*, 4249−4251.

(90) Halperin, A.; Goldbart, P. M. Early Stages of Homopolymer Collapse. *Phys. Rev. E: Stat. Phys., Plasmas, Fluids, Relat. Interdiscip. Top.* 2000, *61*, 565−573.

(91) Maki, Y. Chain Collapse and Aggregation in Dilute Solutions of Poly(Methyl-Methacrylate) Below the Theta Temperature. *Polym. J. (Tokyo, Jpn.)* 2014, *46*, 641.

(92) Lee, N.-K.; Abrams, C. F.; Johner, A.; Obukhov, S. Arrested Swelling of Highly Entangled Polymer Globules. *Phys. Rev. Lett.* 2003, *90*, 225504.

(93) Wang, X.; Qiu, X.; Wu, C. Comparison of the Coil-to-Globule and the Globule-to-Coil Transitions of a Single Poly(N-isopropyla- crylamide) Homopolymer Chain in Water. *Macromolecules* 1998, *31*, 2972−2976.

(94) Chu, B.; Ying, Q.; Grosberg, A. Y. Two-Stage Kinetics of Single-Chain Collapse. Polystyrene in Cyclohexane. *Macromolecules* 1995, *28*, 180−189.

(95) Wu, C.; Wang, X. Globule-to-Coil Transition of a SingleHomopolymer Chain in Solution. *Phys. Rev. Lett.* 1998, *80*, 4092−4094.

(96) Matsuo, E. S.; Tanaka, T. Patterns in Shrinking Gels. *Nature* 1992, *358*, 482−485.

(97) Yoshida, R.; Sakai, K.; Okano, T.; Sakurai, Y. Surface-Modulated Skin Layers of Thermal Responsive Hydrogels as On-Off Switches: II. Drug Permeation. *J. Biomater. Sci., Polym. Ed.* 1992, *3*, 243−252.

(98) Xing, R.; Yuan, C.; Li, S.; Song, J.; Li, J.; Yan, X. Charge-Induced Secondary Structure Transformation of Amyloid-Derived Dipeptide Assemblies from β-Sheet to α-Helix. *Angew. Chem., Int. Ed.* 2018, *57*, 1537−1542.

(99) Yuan, T.; Xu, Y.; Fei, J.; Xue, H.; Li, X.; Wang, C.; Fytas, G.; Li, J. The Ultrafast Assembly of a Dipeptide Supramolecular Organogel and its Phase Transition from Gel to Crystal. *Angew. Chem., Int. Ed.* 2019, *58*, 11072−11077.

(100) Yuan, C.; Ji, W.; Xing, R.; Li, J.; Gazit, E.; Yan, X. Hierarchically oriented organization in supramolecular peptide crystals. *Nat. Rev. Chem.* 2019, *3*, 567−588.

6.0 Summary of Important Findings and Future Directions

This thesis demonstrates advances in the fabrication and utilization of 2D photonic crystal hydrogel sensors. This thesis also presents the development of air-stable protein organogels.

Chapter 1 introduces 2D photonic crystal hydrogel sensors. Chapter 1 also explains the research program's motivation.

Chapter 2 demonstrates the use of a removable polyvinyl alcohol interpenetrating network to support fragile hydrogels. The interpenetrating network supports fragile pH-responsive hydrogels made with low cross-linker concentration. Low cross-linker hydrogels have larger dynamic ranges and lower limits of detection.

Chapter 3 demonstrates an alternative method to decrease the effective crosslinking density, macroporous hydrogels. Macroporous hydrogels have micron-sized voids formed during fabrication by vortexing. Macroporous hydrogels demonstrate an increase in volume response compared to non-macroporous hydrogels.

Chapter 4 explores the effects of salts upon the self-assembly of 2D Photonic Crystals. We elucidate the relationship between the thickness of the debye ring measured and the ordering of the 2D Photonic Crystal.

Chapter 5 examines the structure of protein hydrogels and the mechanism of hydrogel to organogel transition. Protein hydrogels are composed of individual proteins attached like beads on a string in a giant web. The structure of a protein organogel is different from a hydrogel. A protein hydrogel undergoes an irreversible phase separation during the hydrogel to organogel transition. Protein organogels have a dense solid-looking polymer structure. The web structure of the hydrogel is not visible.

6.1 Future Directions

There are several future directions for this research. We can investigate whether or not the mechanism of the protein hydrogel to organogel fabrication works with synthetic polymers. We can also investigate new proteins for use in 2D Photonic crystal hydrogels and organogel such as antibodies. For example, anti-HSA antibodies tightly bind human serum albumin, a charged molecule. HSA binding will increase in the hydrogel charge and cause hydrogel volume swelling due to the HSA charge group's immobilization and the consequent immobilization of their counter-ion charges.

Appendix A Chapter 4 Supporting Information

Appendix A.1 Representative SEM Images of 2DPC for 409, 570, and 915 nm Particles for All Salt

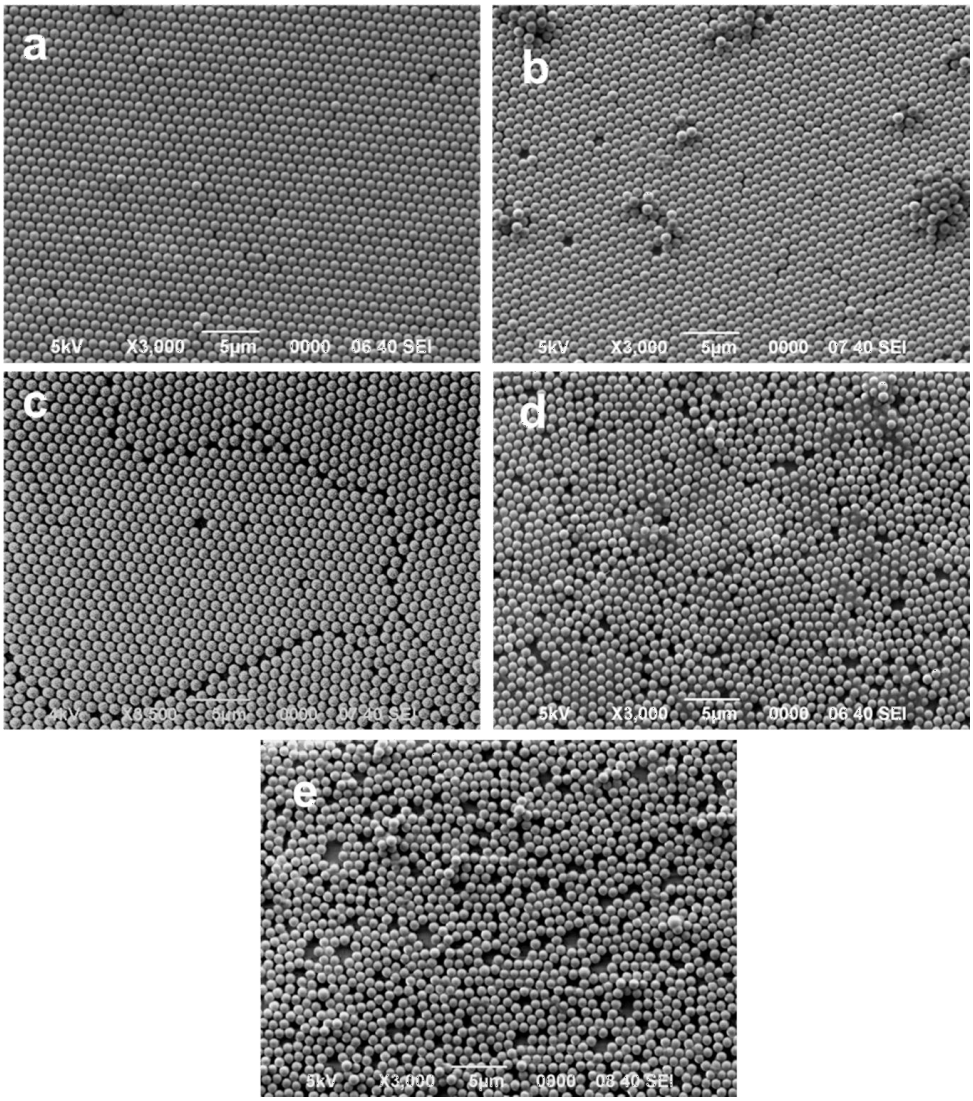

Appendix Figure A.1- 570 nm Diameter 2DPC SEM micrographs of 2DPC fabricated by self-assembly of 915 nm diameter charged polystyreneparticles at the air-water interface of electrolyte solutions containing NaCl. A. Pure Water B. 0.001 M NaCl C.

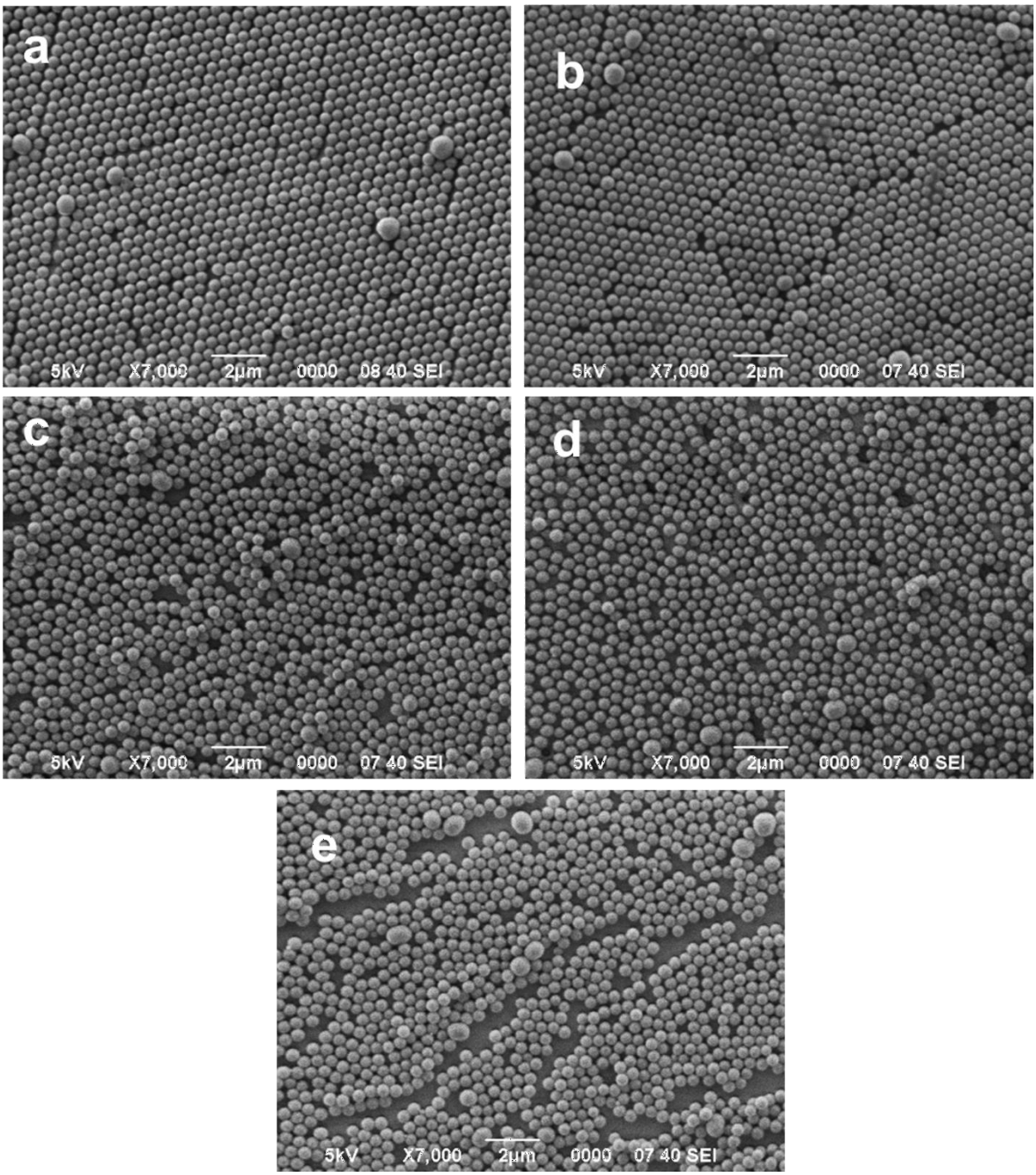

Appendix Figure A.2- SEM micrographs of 2DPC fabricated by self-assembly of 570 nm diameter charged polystyrene particles at the air-water interface of electrolyte solutions containing NaCl. A. Pure Water B. 0.001 M NaCl C. 0.01 M NaCl D. 0.1 M NaCl E. 1 M NaCl

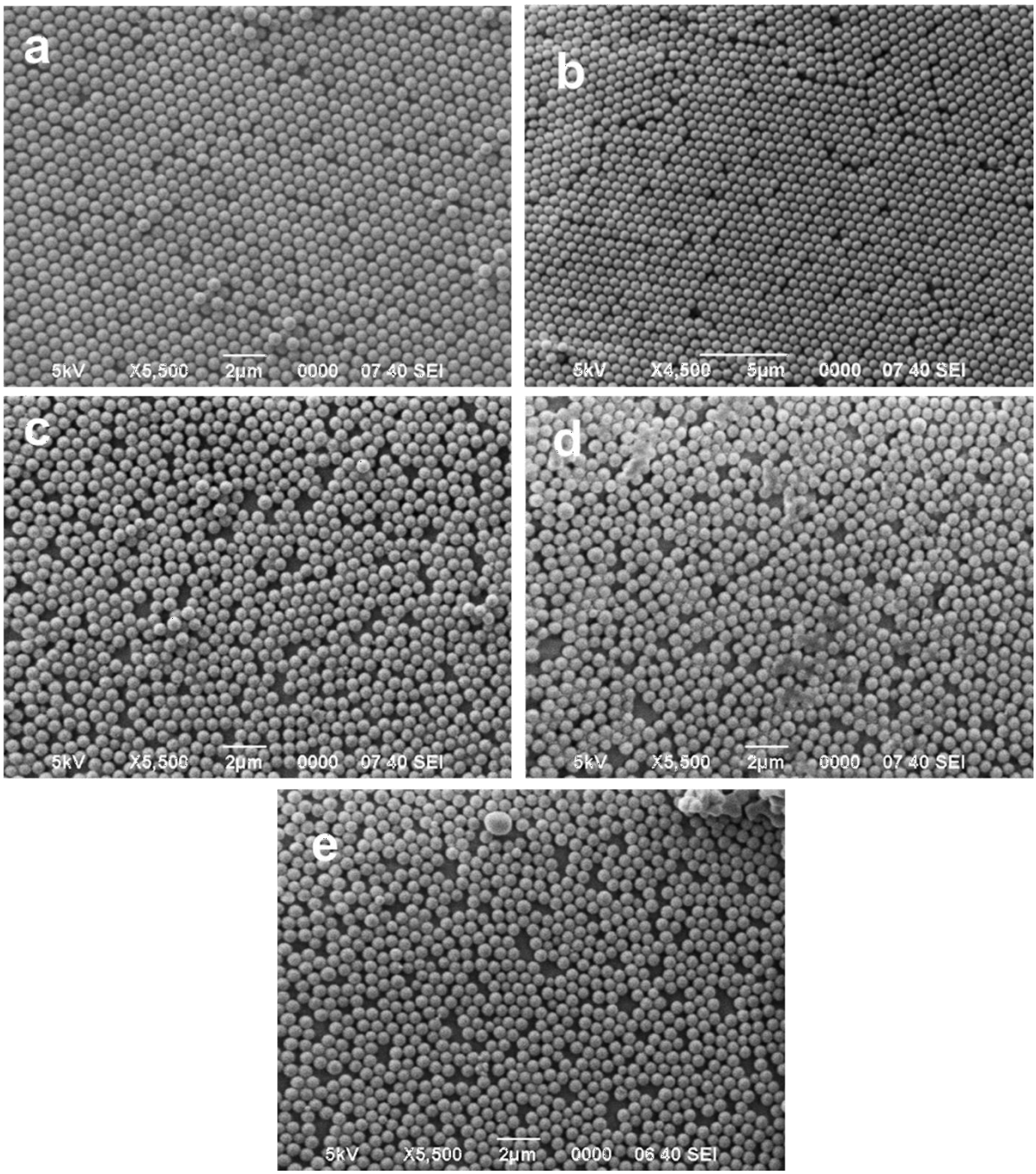

Appendix Figure A.3- SEM micrographs of 2DPC fabricated by self-assembly of 409 nm diameter charged polystyreneparticles at the air-water interface of electrolyte solutions containing NaCl. A. Pure Water B. 0.001 M NaCl C. 0.01 M NaCl D. 0.1 M NaCl E. 1 M NaCl

Appendix A.2 Array Ordering Analysis

First, each image was transformed into a black and white binary image using the GNU Image Manipulation Program (GIMP) using a difference between Gaussians edge-detection filter. The particles in each image were then found using the circle Hough transform algorithm included in the MATLAB scripting package (MathWorks). The centers of the detected particles were passed into a function to calculate the pair correlation function (Equation A.1). The program counts the number of particles, dn, in the areaof the shell, da having an inner diameter, r, and outer diameter, r + dr.

Equation A.1

$$g(r) = \frac{1}{< p >} \frac{dn(r, r + dr)}{da(r, r + dr)}$$

This was done for increasing shell radii, r = 0 to 14, increasing by, dr = $0.016R_0$, where R_o is the particle radius[1]. A plot of g(r) with respect to the normalized distance $R/2R_o$ from 15 SEM images was produced for each particle size and salt concentration. The function utilized is appended as arrayOrdering.m and automated with the appended 2DOrderingProc.m

The g(r) plots were further analyzed utilizing a discrete Fast Fourier Transform (FFT). The FFTs of theaverage g(r) spectra were taken using the FFTW library included in the MATLAB software. The Full Width Half Maximum (FWHM) bandwidth of the first peak of the FFT of g(r)-1 can be used to quantify 2DPC ordering[1-3]. The width of the first peak is directly related to the decay in g(r). As the 2DPC long range order decreases, the width the first FFT peak increases. The dimensionless ordering parameter (κ/κ_o) is the ratio of the FWHM of the FFT peak for a fabricated

2DPC, κ and the FWHM of the FFT peak for a perfect array[1]. κ was averaged over all 15 data sets for each salt concentration and particle sizewith the appended KAve.m

A Gaussian baseline was observed in the FFTs of 2DPCs of poor ordering. A Gaussian peak in the g(r) spectrum appears as a Gaussian peak in the FFT of g(r)-1[4]. The baseline was nearly eliminated by removing the first Gaussian peak in the g(r) spectrum. Removal of the first Gaussian peak in g(r) does not affect the rate of decay in g(r) peaks, the source of the line width, therefore the FFT bandwidth is noteffected.[4]

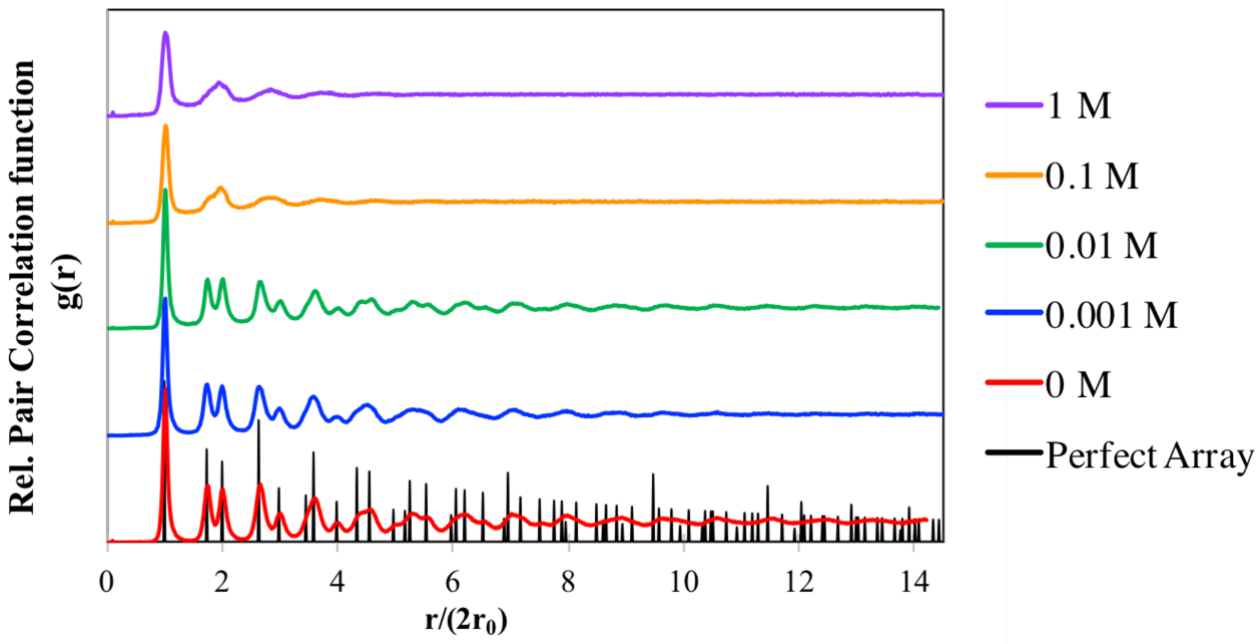

Appendix Figure A.4- 2D Pair Correlation function for a perfect close-packed 2D array of circles with 409 nm diameters and 2DPC of 409 nm particles fabricated on pure water and on 0.001, 0.01, 0.1, and 1M NaCl solutions

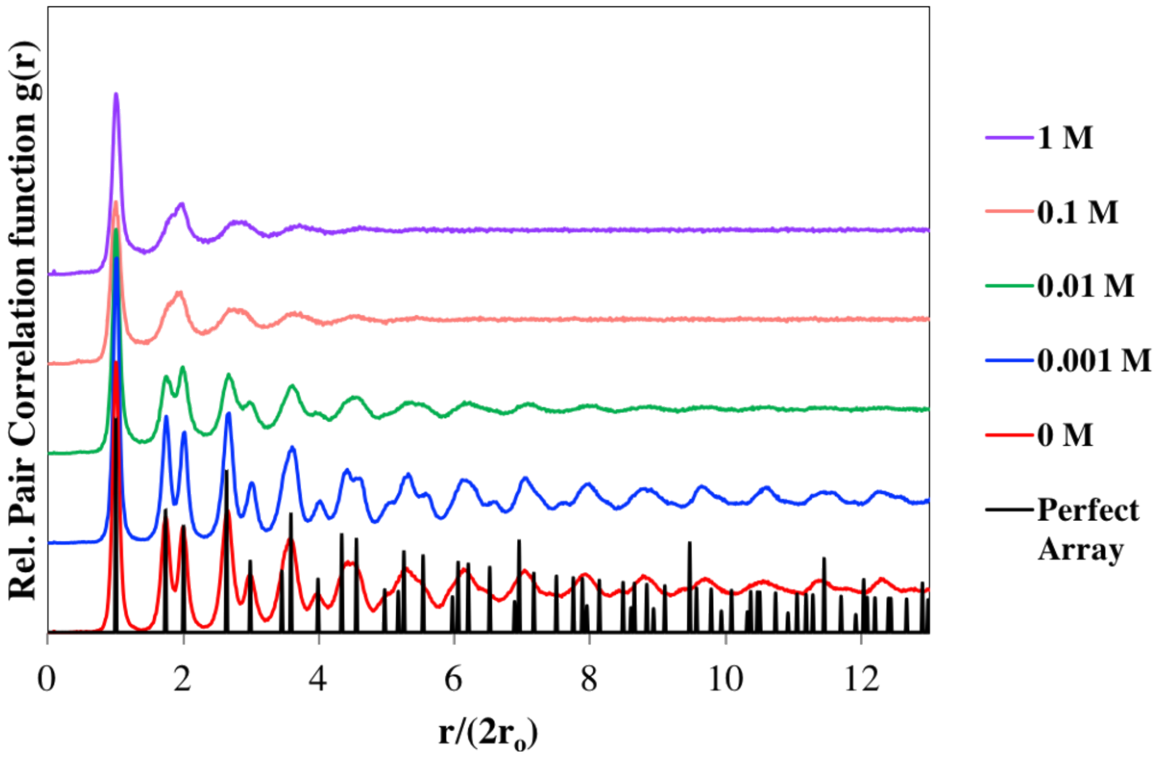

Appendix Figure A.5- 2D Pair Correlation function for a perfect close-packed 2D array of circles with 570 nm diameters and 2DPC of 570 nm particles fabricated on pure water and on 0.001, 0.01, 0.1, and 1M NaCl solutions

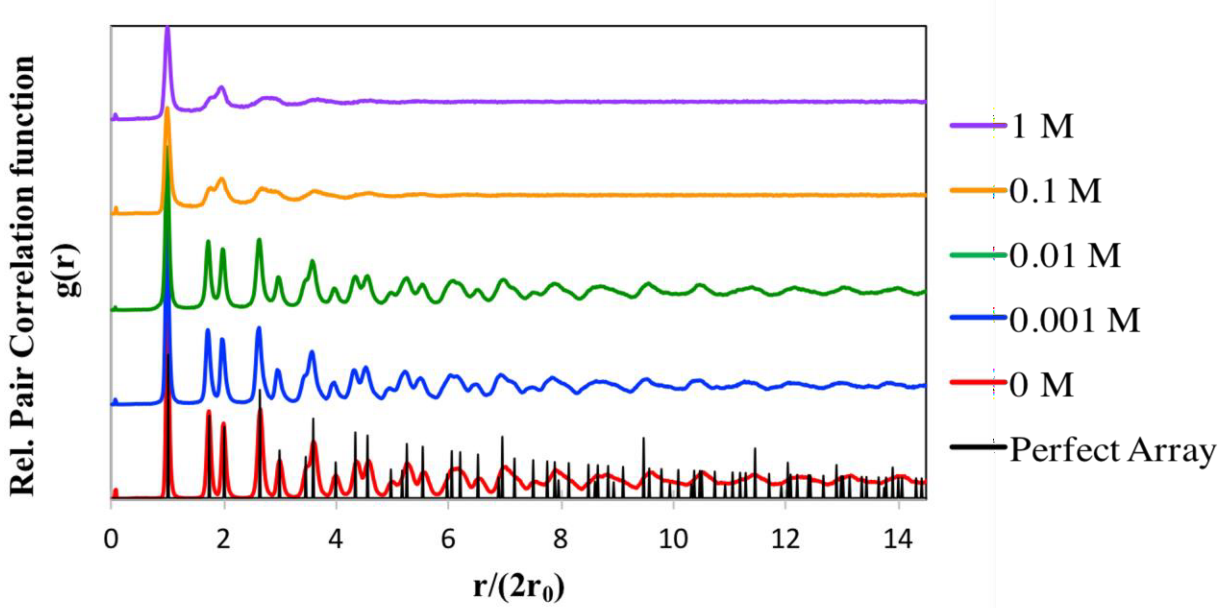

Appendix Figure A.6- 2D Pair Correlation function for a perfect close-packed 2D array of circles with 915 nm diameters and 2DPC of 915 nm particles fabricated on pure water and on 0.001, 0.01, 0.1, and 1M NaCl solutions

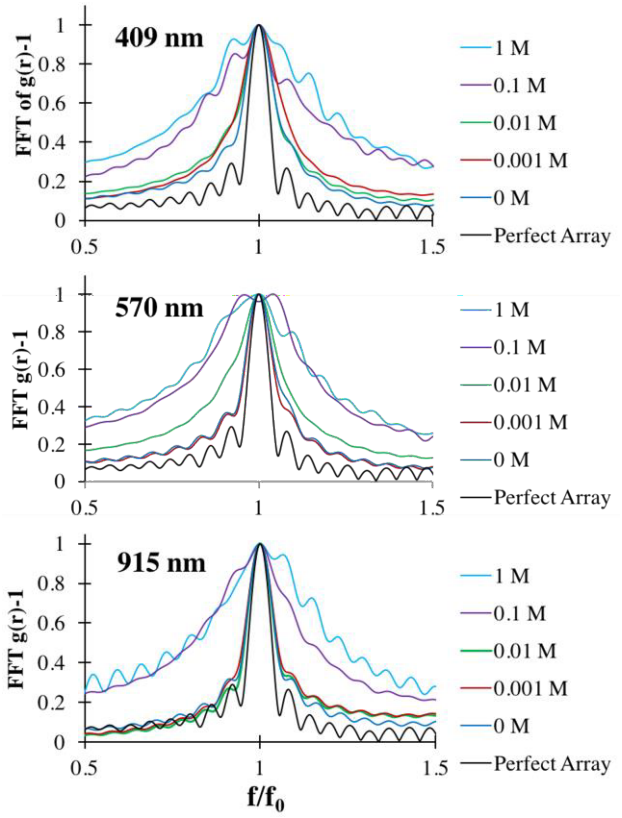

Appendix Figure A.7- The first peak of the FFT of g(r)-1 plotsfor 2DPC arrays of 413nm (top), 570nm (middle), and 915nm (bottom).

Appendix A.3 References

(1) Zhang, J.-T.; Wang, L.; Lamont, D. N.; Velankar, S. S.; Asher, S. A., Fabrication of Large-AreaTwo-Dimensional Colloidal Crystals. *Angew. Chem. Int. Ed.* **2012,** *51* (25), 6117-6120.

(2) Bohn, J. J.; Ben-Moshe, M.; Tikhonov, A.; Qu, D.; Lamont, D. N.; Asher, S. A., Charge stabilizedcrystalline colloidal arrays as templates for fabrication of non-close-packed inverted photonic crystals. *J. Colloid Interface Sci.* **2010,** *344* (2), 298-307.

(3) Rengarajan, R.; Mittleman, D.; Rich, C.; Colvin, V., Effect of disorder on the optical properties ofcolloidal crystals. *Physical Review E* **2005,** *71* (1), 016615.

(4) Bracewell, R. N., *The Fourier transform and its applications*. McGraw Hill: Boston, 2000; Vol. 3rd.

Appendix B Chapter 5 Supporting Information

Appendix B.1 Sample Holder for Cryo-SEM Frozen Hydrated Samples

Appendix Figure B.1- Cryo-SEM sample holder. The sample cavity on the right contains one of the Ted Pella brass planchets that is used to freeze and fracture the hydrogel or organogel samples. The sample cavity on the left is empty.

Appendix B.2 UVRR Spectra of BSA Hydrogels and BSA Protein Monomers in Aqueous Solutions

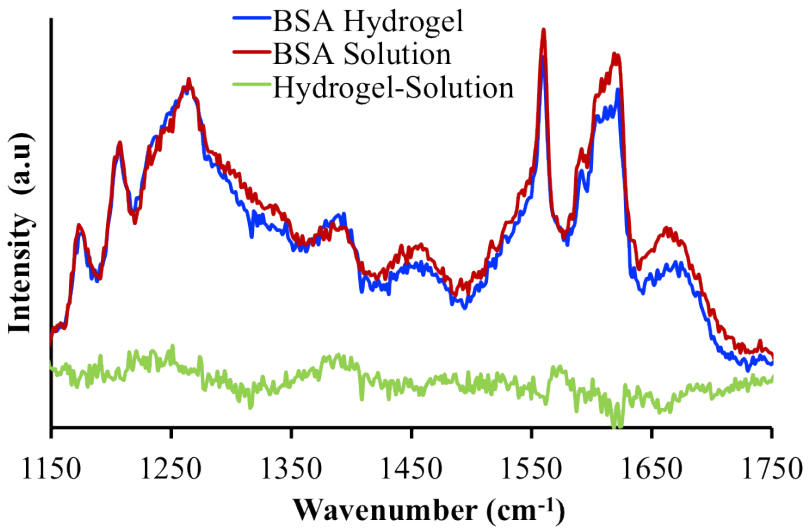

Appendix Figure B.2- UVRR measurements and protein secondary structure determination fitting the BSA UVRR spectra

Appendix B.3 UVRR Measurements and Protein Secondary Structure Determination

Appendix B.3.1 Fitting the BSA UVRR Spectra

We used Grams software (version 8.0, Thermo Fisher Scientific, Inc. Waltham, Mass., USA) to model our UVRR spectra as a sum of Gaussian and Lorentzian bands:

Equation B.1

$$f(x) = \sum_i (1 - M)\left(He^{-\left(\frac{x-x_0}{w}\right)^2(4\ln(2))}\right) + (M)\left(\frac{H}{4\left(\frac{x-x_0}{w}\right)^2+1}\right)$$

where H is the peak height, X_0 is the peak frequency, w is the full width at half height, M=1 if the band is Lorentzian, and M=0 if the band is Gaussian for the i^{th} UVRR band. The $AmIII_3^S$ fitted bands were modeled as Gaussian bands because they are inhomogenously broadened due to the peptide Ψ angle distribution.[1]

Appendix B.3.2 Ψ Ramachandran Angle Calculation

Details describing the methodologies for calculating Ψ angles are reported by Mikhonin et al.[1-2] We use the following equation to calculate the Ψ angle for the α-helix $AmIII_3^S$ bands:

Equation B.2

$$v_i = 1244\ cm^{-1} - 54\ cm^{-1} \sin(\Psi + 26)$$

where υ_i is the $AmIII_3^S$ frequency and Ψ is the backbone Ramachandran Ψ angle. As discussed by Mikhonin et al.,[1] this equation is used to calculate the Ψ angles for the peptide backbones involved in backbone-backbone hydrogen bonding.[1]

Appendix B.3.3 Estimation of the Change in BSA Organogel α-Helix Populations

To estimate the change in protein secondary structure in the BSA organogel, we divided thetotal intensity of the $AmIII_3$ bands in BSA by the intensity of the hydrogel-organogel difference spectrum. We find that the intensity of the hydrogel-organogel difference spectrum is ~4% that of the total intensity of the $AmIII_3$ band. Therefore, we estimate that the organogel contains ~4% moreα-helical peptide bonds compared to that of the hydrogel.

Appendix B.4 NIR Absorption of Ethylene Glycol-Water Solutions and BSA Organogels

Small volumes of water were added to 1.6 mL aliquots of EG. The EG aliquots were directly taken from the final EG solution in which the organogels were equilibrated. During the solvent exchange, the organogels were placed on a shaker to mix the solutions. The exchange to pure EG took place over 2 days, in which ~250 mL of pure EG was replaced 3 times daily to remove bulk water in the samples.

The 1400-2000 nm NIR absorption spectra of ethylene glycol (EG) solutions containing 0, 5, 10, 15, 20, and 25 μL water are shown in Figure B.3a. EG-water solutions were measured in a 5 mm path length quartz cuvette. Water has strong absorption peaks at ~1400 and ~1900 nm that are used to monitor the samples water content.[3,4-5] These absorption bands derive from the first overtone of the OH-stretching band (~1400 nm) and the combination of the OH-stretching band andthe O-H bending band (~1900 nm).[6]

We utilize the ~1900 nm peak to monitor the water content in the mobile phase because EG has stronger absorption around 1400 nm due to its O-H stretching mode. EG has minimal absorption at ~1900 nm.[7] Pure EG in a 5 mm pathlength cuvette shows an absorbance of 0.7 at 1915nm.[7] We measured an absorbance of 0.74 at 1915 nm for the EG extracted from the bottle containing the organogels, corresponding to 0.08 M water in the bulk EG.

The difference spectrum of the EG/water solutions with the pure EG spectrum subtracted is shown in Figure SI 3b. The increasing absorbance from the increasing water concentration at ~1400and ~1900 nm is clearly evident. The 1915 nm absorbance of the EG/water solutions from this difference spectrum (Figure B.4) was used to calculate the molar absorptivity, ε, of water using theBeer-Lambert equation. The 1915 nm molar absorptivity coefficient of water was calculated to be ε=0.95 M^{-1} cm^{-1}.

The 1400 – 2000 nm NIR absorbance of our BSA organogels is shown in Figure SI 5. The organogel films are 420 µm thick such that the double film layer is 840 µm thick. The 1915 nm absorbance of these organogels are 0.32 for the single film layer and 0.63 for two film layers. Theseabsorbance values yield organogel water concentrations of 8.1 M for a single organogel film and 7.9M for two organogel films (average 8.0 ± 0.2 M water).

To account for the small EG absorbance at 1915 nm in the organogel, we subtracted the absorbance of a pure EG film having a thickness of either 420 µm or 840 µm. A pure EG film of

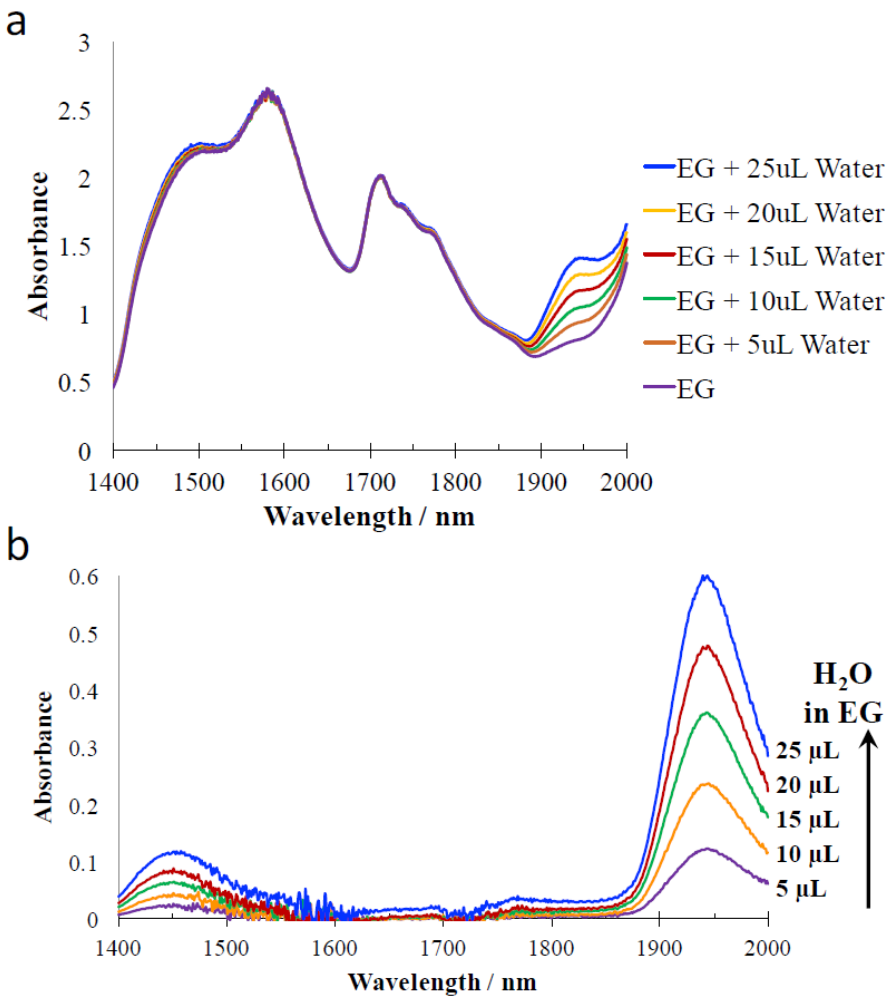

Appendix Figure B.3- NIR absorbance of EG and its water solutions in a 5 mm path length quartz cuvette between 1400 nm to 2000 nm. (a) Spectra of pure EG with 0, 5, 10, 15, 20, and 25 µL water added (b) Difference Spectra of (EG/water solution) - EG spectra.

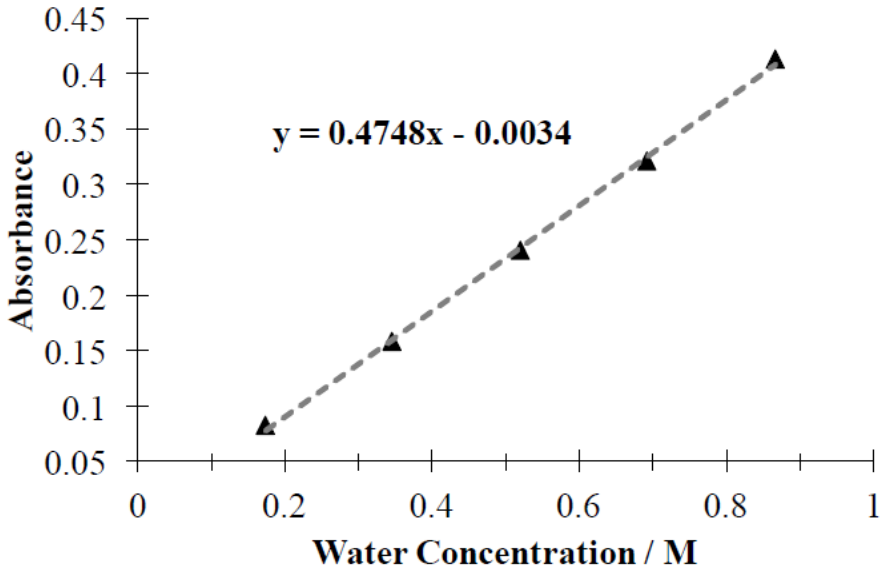

Appendix Figure B.4- (EG+water)-EG difference spectra absorbance at 1915 nm as a function of water concentration. The slope of the best fit line is 0.47 A.U. M^{-1}.

420 µm thickness has a theoretical absorbance of 0.065 and an 840 µm thick EG film has an absorbance of 0.13. The 1915 nm absorbance of the organogel films decrease to 0.26 (420 µm) and 0.50 (840 µm) when the pure EG film absorbance is subtracted, Figure B.5. The water concentration calculated from the EG subtracted organogel absorbance is now 6.5 M for a single organogel film and 6.3 M for two organogel films (average 6.4 ± 0.2 M water). This subtraction overestimates the absorbancefrom EG in the BSA organogels because the organogels contain less EG than a pure EG film. Thus,the water concentration calculated from the subtracted organogel absorbance underestimates the water content.

Based on these measurements, we calculate the number of water molecules per BSA proteinin a 1 mL BSA organogel sample. The organogel has a BSA polymer volume fraction of $\phi = 0.27$.The organogel protein concentration is 360 mg/mL BSA (BSA MW: 66430 g/mol). Thus, a 1 mL sample of the BSA organogel contains 3.3 x 10^{18} molecules of BSA. A 1 mL BSA organogel sample that contains 6.5 – 8 M water has 3.9 x 10^{21} to 4.8 x 10^{21} molecules of water.

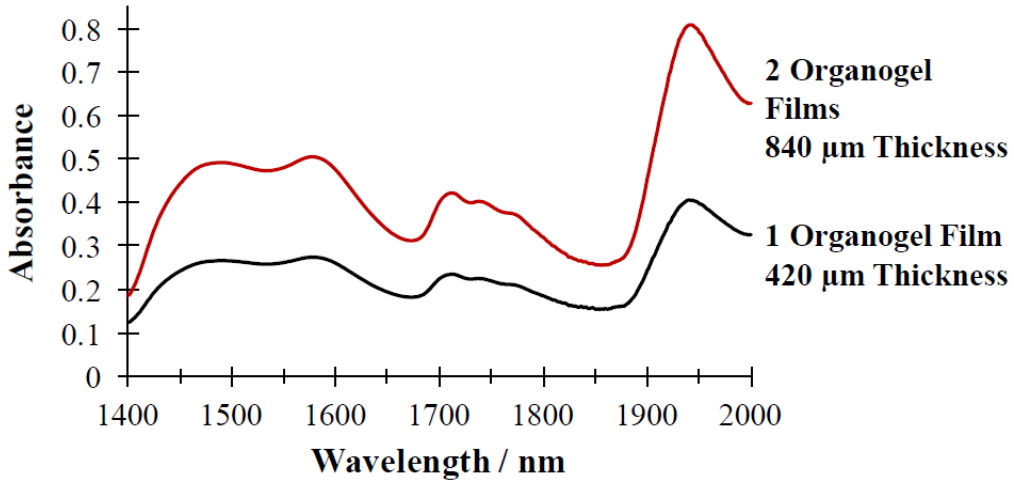

Appendix Figure B.5- The 1400-2000 nm NIR absorbance of a single and double layer BSA organogel film.

Therefore, the ratio of water molecules per BSA protein in the organogel is calculated to be 1182-1477 water molecules per BSA protein.

Appendix B.4.1 Hydrophilic BSA Polymers Retain Much of Their Hydration Shell Waters in EG

Polar solvents, such as EG, more effectively strip water from a protein surface compared tonon-polar solvents due to more favorable solvation enthalpies between the water and polar organicsolvent.[8-11] Hydrated proteins exposed to non-polar organic solvents often retain more of their hydration layers than hydrated proteins exposed to polar organic solvents.[9,11] However, while thesehydrophilic polar organic solvents can strip away water molecules that are loosely bound to the protein surface, the polar organic solvents have little effect on the tightly bound water molecules around ionic and polar amino acid residues on the protein surface.[9-11]

The protein hydration shell around the crosslinked BSA proteins in the pure EG organogel ismostly retained, at least in part due to the very hydrophilic nature of BSA. Gekko et al[12] experimentally demonstrated that BSA is preferentially hydrated in solutions containing 60% EG

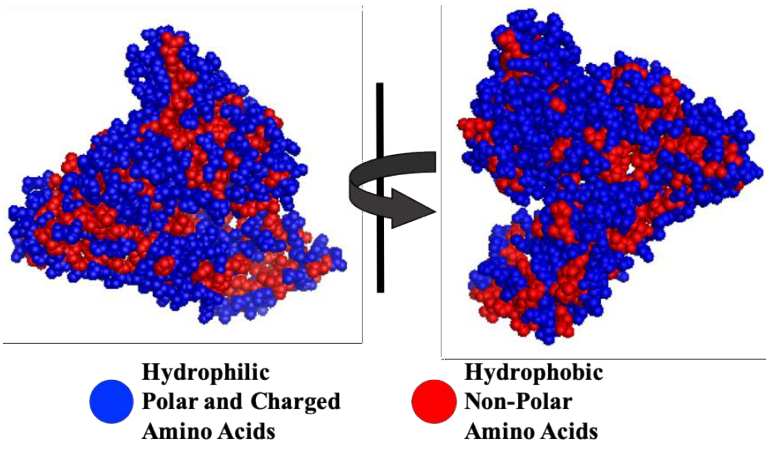

Appendix Figure B.6- BSA protein structure from X-ray crystallography (PDB: 3V03)[13]. Hydrophilic amino acid residues are colored blue (Lys, Arg, Asp, Glu, His, Ser, Thr, Asn, Gln, Cys); hydrophobic amino acid residues are colored red (Gly, Ala, Leu, Ile, Met, Val, Phe, Tyr, Trp, Pro).

in water. As shown in Figure SI 6, the BSA surface exposed to solvent is predominately hydrophilic. The hydrophilic charged and polar amino acids are shown in blue in Figure SI 6, and the non-polar hydrophobic amino acids are shown in red. The hydration shell waters that are tightly bound to the large surface area of hydrophilic domains in BSA likely remain intact when the aqueous mobilephase is exchange to pure EG.

Additionally, protein hydration shells have been protected by modifying the proteins or the protein microenvironment to enhance protein activity in organic solvents. For example, attaching highly hydrophilic groups to proteins is an effective method to protect the protein hydration shell and increase enzyme activity.[14] These hydrophilic groups tightly bind numerous waters to form a protective hydrating shell around the protein, thus decreasing the ability of the organic solvent to strip waters from the protein surface. Improved protein hydration has also been demonstrated for proteins immobilized on hydrophilic materials[15] and for proteins encapsulated in hydrophilic polymer networks.[16]

Appendix B.5 References

(1) Mikhonin, A. V.; Bykov, S. V.; Myshakina, N. S.; Asher, S. A., Peptide Secondary Structure Folding Reaction Coordinate: Correlation between UV Raman Amide III Frequency, Ψ Ramachandran Angle, and Hydrogen Bonding. *J. Phys. Chem. B* **2006,** *110*, 1928-1943.

(2) Asher, S. A.; Mikhonin, A. V.; Bykov, S., UV Raman Demonstrates that α-Helical Polyalanine Peptides Melt to Polyproline II Conformations. *J. Am. Chem. Soc.* **2004,** *126*, 8433-8440.

(3) Büning-Pfaue, H., Analysis of Water in Food by Near Infrared Spectroscopy. *Food Chem.* **2003,** *82*, 107-115.

(4) Tran, C. D.; De Paoli Lacerda, S. H.; Oliveira, D., Absorption of Water by Room-Temperature Ionic Liquids: Effect of Anions on Concentration and State of Water. *Appl. Spectrosc.* **2003,** *57*, 152-157.

(5) Smith, N. L.; Hong, Z.; Asher, S. A., Responsive Ionic Lquid-Polymer 2D Photonic Crystal GasSensors. *Analyst* **2014,** *139*, 6379-6386.

(6) Luck, W. A. P.; Schiöberg, D., Spectroscopic Investigations of the Structure of Liquid Water and Aqueous Solutions. *Adv. Mol. Relax. Interact. Proces.* **1979,** *14*, 277-296.

(7) GuidedWave, An Introduction to Online NIR Water Measurements in Liquid Samples. *AZO Mater. [Online]*, Jan. 25, 2019, https://www.azom.com/article.aspx?ArticleID=17511 (accessed May, 27, 2019).

(8) Sirotkin, V. A.; Sukhov, A. V.; Dudkina, E. V., Heat Effects of Dehydration of Human Serum Albumin in Hydrophilic Organic Solvents. *Eng. Life Sci.* **2009,** *9*, 74-81.

(9) Yang, L.; Dordick, J. S.; Garde, S., Hydration of Enzyme in Nonaqueous Media is Consistent with Solvent Dependence of its Activity. *Biophys. J.* **2004,** *87*, 812-821.

(10) Halling, P. J., High-Affinity Binding of Water by Proteins is Similar in Air and in Organic

Solvents. *Biochim. Biophys. Acta, Protein Struct. Mol. Enzymol.* **1990,** *1040*, 225-228.

(11) Micaêlo, N. M.; Soares, C. M., Modeling Hydration Mechanisms of Enzymes in Nonpolar andPolar Organic Solvents. *FEBS J.* **2007,** *274*, 2424-2436.

(12) Gekko, K.; Morikawa, T., Preferential Hydration of Bovine Serum Albumin in Polyhydric Alcohol-Water Mixtures. *J. Biochem.* **1981,** *90*, 39-50.

(13) Majorek, K. A.; Porebski, P. J.; Dayal, A.; Zimmerman, M. D.; Jablonska, K.; Stewart, A. J.; Chruszcz, M.; Minor, W., Structural and Immunologic Characterization of Bovine, Horse, and Rabbit Serum Albumins. *Mol. Immunol.* **2012,** *52*, 174-182.

(14) Khmelnitsky, Y. L.; Belova, A. B.; Levashov, A. V.; Mozhaev, V. V., Relationship Between Surface Hydrophilicity of a Protein and its Stability Against Denaturation by Organic Solvents. *FEBS Lett.* **1991,** *284*, 267-269.

(15) Stepankova, V.; Bidmanova, S.; Koudelakova, T.; Prokop, Z.; Chaloupkova, R.; Damborsky, J.,Strategies for Stabilization of Enzymes in Organic Solvents. *ACS Catal.* **2013,** *3*, 2823-2836.

Zhang, P.; Sun, F.; Tsao, C.; Liu, S.; Jain, P.; Sinclair, A.; Hung, H.-C.; Bai, T.; Wu, K.; Jiang, S., Zwitterionic Gel Encapsulation Promotes Protein Stability, Enhances Pharmacokinetics, and Reduces Immunogenicity. *Proc. Natl. Acad. Sci. U.S.A.* 2015, *112*, 12046-12051